Electron/photon Identification and Standard Model Higgs Process Studies at the High Level Trigger for the ATLAS experiment

Inauguraldissertation

der Philosophisch-naturwissenschaftlichen Fakultät

der Universität Bern

vorgelegt von

Valeria Perez Reale

von Spanien

Leiter der Arbeit: Prof. Dr. K. Pretzl

Laboratorium für Hochenergiephysik

Electron/photon Identification and Standard Model Higgs Process Studies at the High Level Trigger for the ATLAS experiment

Inauguraldissertation

der Philosophisch-naturwissenschaftlichen Fakultät
der Universität Bern

vorgelegt von

Valeria Perez Reale

von Spanien

Leiter der Arbeit: Prof. Dr. K. Pretzl

Laboratorium für Hochenergiephysik

Von der Philosophisch-naturwissenschaftlichen Fakultät angenommen.

Bern, den 2. Februar 2006   Der Dekan

Prof. Dr. P. Messerli

Abstract

The ATLAS experiment, one of the four detectors at the Large Hadron Collider currently under construction at CERN with start–up date in 2007, will search for Standard Model Higgs Bosons and for new physics beyond the Standard Model up to the TeV scale. The LHC will collide proton beams at a center–of–mass energy of 14 TeV with an interaction rate of 10^9 Hz. The ATLAS online selection will face the challenge of efficiently selecting interesting candidate events whilst rejecting the enormous number of minimum bias and QCD–jet background events reducing the bunch crossing rate of 40 MHz to around 200 Hz for permanent storage. The ATLAS trigger is performed in a three level selection: Level1, Level2 and the Event Filter; the last two are viewed as the High Level Trigger. In this thesis the High Level Trigger strategy and physics performance for the electron and photon selection and the potential to trigger on a Standard Model Higgs with electron and photon decays in the low mass region $m_H < 2m_Z$ has been evaluated. In addition, to validate the electron trigger selection the electron/pion separation capability with the High Level Trigger has been studied with real data from the ATLAS Combined Test Beam 2004.

Contents

Chapter 1

Introduction

The Standard Model is a very succesful theory that describes at a level of high accuracy the interactions of elementary particles which have been so far covered by several experiments. Nevertheless, it is not considered the ultimate theory for the description of particle physics, mainly since neither the fundamental parameters, masses and couplings, nor the symmetry pattern can be derived and the gravitational interaction is not coherently incorporated in the theory. Furthermore, the Higgs mechanism for generating the masses of the fundamental particles which is a cornerstone of the model, still lacks experimental verification up to now, in particular the Higgs boson which should arise if this mechanism is right, has not yet been discovered.

The Large Hadron Collider, which is currently being constructed at CERN, will disclose a new energy range to experimental particle physics and will allow the search for several proposed extensions to the Standard Model. The LHC will collide protons at a center of mass energy of 14 TeV with a bunch crossing rate of 40 MHz. The ATLAS detector, one of the multipurpose experiments at the LHC, will face the challenge of efficiently selecting interesting physics events, whilst rejecting an enormous number of QCD background events. Very complex trigger and data aquisitions systems are being designed in order to reduce online the initial event rate of 10^9 minimum bias events produced each second to an event rate of ~ 200 Hz going to mass storage.

A key element of the ATLAS trigger and data aquisition system is the High Level Trigger (HLT) which is responsible for the online event selection and filtering involving a rate reduction of a factor of several hundred, and for the classification of all accepted events for further offline physics analysis. This task will be performed in two stages: at the first stage (Level2) the event selection will be performed in an average latency of 10 ms and at the second stage (Event Filter) in an average latency time of 1 s. Therefore, the physics and event selection architecture development and performance studies are crucial for the data taking of the ATLAS experiment.

This thesis presents a study of the electron/photon selection and Standard Model Higgs Process selection in the ATLAS High Level Trigger. In Chapter 2 the physics motivation for the construction of the LHC are given. Chapter 3 describes the LHC challenging environment and the ATLAS detector as well as the physics signatures and potential of the ATLAS experiment to discover Standard Model Higgs Processes. Chapter 4 contains a

brief overview of the trigger and data aquisition system with emphasis on the HLT selection stages (Level2 and Event Filter) and their common selection software. In Chapter 5 the physics strategy for the online selection of events in ATLAS is presented for both LHC luminosity scenarios. The electron/photon Level1 and HLT algorithm selection is described in Chapter 6. Chapter 7 presents a study of the inclusive electron/photon selection and the rejection capability against QCD–jets at the different trigger selection steps (Level1– Level2–Event Filter) at different luminosities. The physics performance in terms of trigger efficiency and rates is evaluated on MonteCarlo simulated data and the system performance is studied for the different HLT electron/photon selection algorithms. In Chapter 8 the potential to trigger on the following SM Higgs decay channels with lepton and photons in the final state: $H \rightarrow \gamma\gamma$, $H \rightarrow ZZ^* \rightarrow 4l$, and $H \rightarrow WW^* \rightarrow l\nu l\nu$ decay via VBF have been studied for the low mass region, $m_H < 2m_Z$. Chapter 9 contains a study of the electron/pion separation performed with real data obtained in the 2004 ATLAS Combined Test Beam. Trigger electron efficiencies and pion fake rates have been studied for different particle energies using the Level2 electron trigger.

Chapter 2

The Standard Model and Beyond

The Standard Model (SM) is a consistent, finite and, within the limitations of our present technical ability, a computable theory of fundamental microscopic interactions that successfully explains most of the known phenomena in elementary particle physics. The SM describes strong, electromagnetic and weak interactions [1]. This chapter breifly describes the main components of the model with emphasis on the Higgs boson production mechanism. In addition, some alternative new physics models beyond the Standard Model are also discussed.

2.1 The Standard Model

The laws of Nature are summarized in the Standard Model of particle physics [2, 3, 4, 5]. The basic *constituents of matter* are fundamental spin $\frac{1}{2}$ fermions: six leptons and six quarks [6, 7] which are realized in three families of identical structure. For each of the various fundamental constituents, its symbol and the ratio of its electric charge Q to the elementary charge e of the electron are given in Table 2.1. In the SM the matter fields, all of spin $\frac{1}{2}$, are the quarks, the constituents of protons, neutrons and all hadrons, endowed with both color and electro-weak charges, and the leptons (the electron e^-, the muon μ^-, the tau τ^- plus the three associated neutrinos ν_e, ν_μ and ν_τ) with no color but with electro-weak charges. At present there is no explanation for this triple repetition of fermion families. The entire ensemble of these constituents has been identified experimentally. The least known properties of these constituents are the profile of the top quark, the mixing among the lepton states and the quark states, and in particular, the structure of the neutrino sector.

Four different *forces* act between the leptons and quarks: electromagnetic, weak, strong, and gravitational. The electromagnetic and weak forces are unified in the Standard Model. The fields associated with these forces, as well as the fields associated with the strong force, are spin-1 fields, describing the photon γ, the electroweak gauge bosons $W^\pm$ and $Z^\pm$, and the gluons g. There are three strong charges, called 'color' charges and three electro-weak charges (which in particular include the electric charge). The force carriers, of spin 1, are the photon γ, the weak interaction gauge bosons W^+, W^- and Z^0 and the eight gluons g that mediate the strong interactions. The photon and the gluons have zero masses as a consequence of the exact conservation of the corresponding symmetry

Table 2.1: The fundamental fermions.

Particle	Flavour	$Q/|e|$
leptons	e μ τ	-1
	ν_e ν_μ ν_τ	0
quarks	u c t	$+\frac{2}{3}$
	d s b	$-\frac{2}{3}$

generators, the electric charge and the eight color charges. The weak bosons $W^\pm$ and Z_0 have large masses ($m_W \sim 80.4$ GeV, $m_Z \sim 91.2$ GeV) signalling that the corresponding symmetries are spontenously broken. The interactions of the force fields with the fermionic constituents of matter as well as their self–interactions are described by Abelian and non–Abelian $SU(3) \times SU(2) \times U(1)$ gauge theories [8, 9]. The experimental exploration of these fundamental gauge symmetries is far advanced in the sector of lepton/quark–gauge boson interactions, yet much less is known so far from experiment about the self–interactions of the force fields. The gravitational interaction is mediated by a tensor field, with a character quite different from spin-1 gauge fields. The gravity sector is attached *ad hoc* to the other sectors of the Standard Model, not properly formulated yet as a quantum phenomenon.

The third component of the Standard Model is the *Higgs mechanism* [10, 11, 12]. In this sector of the theory, scalar fields interact with each other in such a way that the ground state acquires a non–zero field strength, breaking the electroweak symmetries spontaneously. The Higgs mechanism predicts the presence in the physical spectrum of one spin 0 particle, the Higgs boson, not yet experimentally observed. A tremendous experimental effort is underway or planned to reveal the Higgs sector as the last crucial missing link in the SM verification. The Higgs Production mechanism will be described in the next section.

All experimental observations are compatible with the Standard Model at a level of very high accuracy. Not all building blocks of the model, however, have been experimentally established so far. In particular, the Higgs mechanism for generating the masses of the fundamental particles [10, 11, 12] which is a cornerstone of the system, still lacks experimental verification up to now, even though indirect indications support this mechanism quite strongly. Even if all the elements of the Standard Model will be established experimentally in the near future, the model cannot be considered the ultima ratio of matter and forces. Neither the fundamental parameters, masses and couplings, nor the symmetry pattern can be derived; these elements are merely built into the model by hand. Moreover, gravity with a structure quite different from the electroweak and strong forces, is not coherently incorporated in the theory.

Despite this criticism, the Standard Model provides a valid framework for the description of Nature, probed from microscopic scales of order 10^{-16} cm up to cosmological distances of order 10^{28} cm. The model therefore ranks among the greatest achievements of mankind in understanding Nature.

2.1.1 Higgs Production Mechanism

As described in the previous section, the SM is a gauge theory based on a $SU(3) \times SU(2)_L \times U(1)$ symmety. The $SU(2)_L \times U(1)$ symmetry is however spontaneously broken to $U(1)_{em}$ since three massive ($Z^0, W^\pm$) and one massless (γ) gauge bosons are observed: the symmetry, in fact, forbids masses for all particles that have been so far observed (quarks, leptons and gauge bosons). The way the symmetry breaks down is presently experimentally untested.

This problem has been solved by means of the Higgs mechanism [10, 11, 12] in which masses are introduced into gauge theories in a consistent way. The solution of the problem is achieved at the expense of a new fundamental degree of freedom, the Higgs field, which is a scalar $SU(2)$ complex doublet Φ with a potential:

$$V(\Phi) = m^2|\Phi|^2 + \lambda|\Phi|^4 \qquad \text{where} \qquad m^2 < 0 \qquad (2.1)$$

which has a minimum for $|\Phi|^2 = -m^2/(2\lambda) \equiv v^2/2$. The negative condition on the m^2 will impose a positive value of *lambda* due to the vacumm stability criterium. The value of $v \simeq 246$ GeV is fixed by the measurement of the β decay rate. Exploiting the gauge symmetry a particular minimum vacumm state can be selected in order to keep only one degree of freedom of the Higgs boson field. The symmetry can be broken by developing the theory around the selected minimum: this leads to a massive Higgs boson with a mass $m_H^2 = 2\lambda v^2$ while the other three degrees of freedom of the Higgs boson field allow a mass for the gauge bosons. The masses for quarks and leptons arise from the Yukawa couplings between fermions and the Higgs field.

In technical language, the Higgs mechanism leads to a renormalizable gauge field theory including non–zero gauge–boson and fermion masses [13, 14]. After fixing a small number of basic parameters which must be determined experimentally, the theory is under strict theoretical control, in principle to any required accuracy.

The Higgs boson has not been discovered yet and its mass is not theoretically predicted. In the last years extensive studies have been performed on both the experimental and theoretical side in order to derive a set of constrains on the SM Higgs boson mass. The search strategies for the SM Higgs Boson at the Large Hadron Collider (LHC) experiment are described in Chapter 3.4.

A lower bound on the SM Higgs boson mass comes from experimental activities. The LEPII[1] [15] experiments set a 95% confidence level lower bound at 114.4 GeV. Moreover, a global fit to precision SM observables presents a ψ^2 minimum for $m_H = 98$ GeV with $m_H < 212$ GeV at 95% confidence level reffig:LEP2.

From the theoretical point of view the Higgs boson mass is a free parameter of the SM and therefore no prediction can be directly performed. Moreover, it is commonly assumed that the minimal Standard Model is merely a low–energy effective theory of some more fundamental theory which explains the origin of electroweak symmetry breaking: there must therefore exist some energy scale Λ at which the SM breaks down. That is, the Standard model is no longer adequate for describing the theory above Λ and degrees of

---

[1]The Large Electron Positron collider that was running at Cern at a CM energy of 200 GeV for its second running period
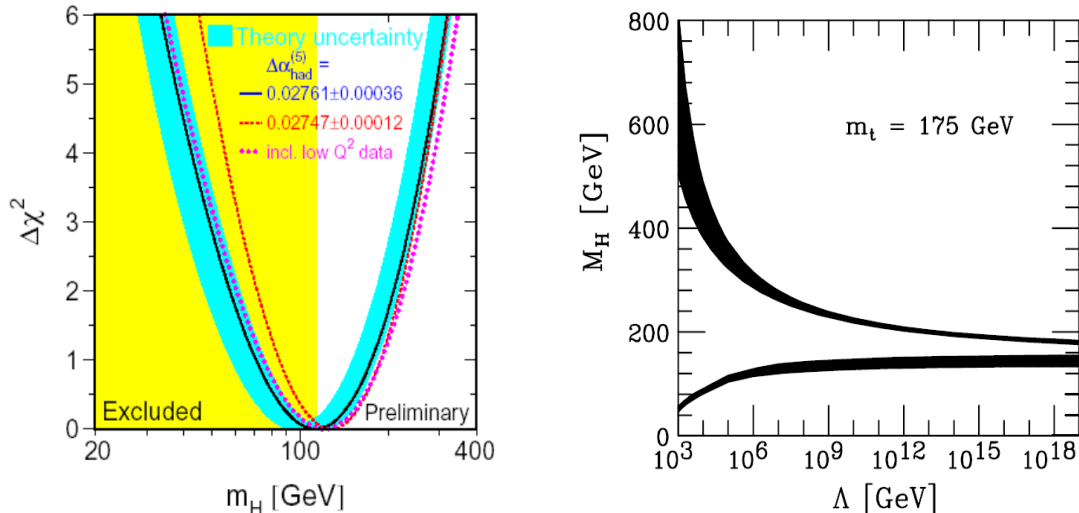
Figure 2.1: Fit of the Standard Model Higgs boson mass from electroweak precision data (left plot). Bounds on the mass of the Higgs boson in the Standard Model: *Lambda* denotes the energy scale at which the Higgs–boson system of the Standard Model would become strongly interacting (upper bound); the lower bound follows from the requirement of vacuum stability (right plot).

freedom related to new physics become relevant. Although the value of Λ is presently unknown, for a given value of Λ one can compute the minimum and the maximum allowed Higgs mass based on three main theoretical arguments: the vacumm stability, the unitary and the triviality of the theory. Lower and upper limits on the Higgs boson mass as a function of the scale Λ are shown in Figure 2.1 where the allowed region is delimited by two curves. As can be noticed, the $130 \text{ GeV} \leq m_H \leq 180 \text{ GeV}$ mass range would be consistent with the hypothesis $\Lambda = M_{pl}$: this would mean that the SM could be in principle valid up to the Planck scale. On the contrary, a Higgs boson mass outside this region would imply a SM breakdown at a certain scale $\Lambda < M_{pl}$ and evidences for new physics should be found nearby.

2.2   Beyond the Standard Model

There are both conceptual problems and phenomenological indications for physics beyond the SM. On the conceptual side the most obvious problems are that quantum gravity is not included in the SM and the related hierarchy problem. Among the main phenomenological hints for new physics there is coupling unification, dark matter, neutrino masses, baryogenesis and the cosmological vacuum energy [16].

Altough the Higgs mass range $130 \text{ GeV} \leq m_H \leq 180 \text{ GeV}$ seems to allow the Standard Model to survive up to the Planck scale this hypothesis is considered to be unlikely: this conclusion is based on the *naturalness* argument. In an effective field theory the masses

are calculable in terms of parameters of a more fundamental renormalizable theory that describes physics at the energy scale Λ: in the SM the Higgs boson mass is quadratically sensitive to the scale Λ. At one loop:

$$m_H^2 = (m_H^2)_0 + cg^2\Lambda^2 \qquad (2.2)$$

where $(m_H^2)_0$ is a parameter of the more fundamental theory and c is a constant O(1). Therefore, assuming an upper limit on the Higgs mass of 1 TeV one can obtain a 'natural' value for $\Lambda \simeq m_H/g \sim$O(1 TeV). If Λ is significantly larger than 1 TeV (*hierarchy problem*) only an 'unnatural' cancellation (*fine tuning*) between the two terms in eq. 2.2 could explain a Higgs mass at the order of the electroweak symmetry breaking [17, 18].

Another reason why the Standard Model is generally believed to be just an effective low energy theory is the fact that the force of gravity, which is important for very high energies (10^{16} GeV) is not included in the SM.

The impressive success of the SM [16] sets strong limits on models for new physics: in general, models that preserve the SM structure and introduce soft improvements are clearly prefered. SUSY models are the most developed and widely accepted: the supersymmetric extension of the SM is a well defined and computable model which also preserves all virtues of the SM. *Supersymmetry* is a beautiful theory that postulates a symmetry connecting fermions and bosons. If the symmetry exists at high energies, then additional fermionic loops would cancel the quadratic divergences of bosons solving the hierarchy problem. In addition, supersymmetric theories require two Higgs doublets.

The fact that no supersymmetric particles have yet been observed means that supersymmetry is not an unbroken symmetry in Nature. In the minimal supersymmetric extension to the Standard Model (MSSM) there are no assumptions made to the SUSY–breaking mechanism. Instead, all possible SUSY-breaking terms are considered, which gives rise to more than 100 new, fundamental parameters. Models exist in which the the low–energy parameters are determined from only a few parameters, which live at a much higher scale, by assuming a specific SUSY-breaking mechanism. These models include minimal-Supergravity (mSUGRA), minimal Gauge Mediated SUSY Breaking (mGMSB) and minimal Anomaly Mediated SUSY Breaking (mAMSB) [19].

Another recent model for new physics implies the existence of *large compactified extra dimensions*. In this model the hierarchy problem is solved by bringing the gravity scale from M_{pl} to $\sim$O(1 TeV): the idea from string theories is that the SM fields are confined to a four–dimensional brane immersed in a d–dimensional bulk. Gravity feels the whole geometry and appears to be weak in the brain because a lot of lines of force escape in extra dimensions [20].

No signal of new physics has been found yet experimentally. However, to make a light Higgs natural in presence of quantum fluctuations new physics should not be so far. This is encouraging for the LHC that should experimentally clarify the problem of the electroweak symmetry breaking sector and probably (hopefully) find new physics signatures at the TeV scale.

Chapter 3

The LHC and the ATLAS Detector

In this chapter the motivations and the main features of the Large Hadron Collider (LHC) as well as some details of the ATLAS experiment will be introduced. In the first section the relevant accelerator parameters and the physics programme allowed by the machine potential will be reviewed and an overview of the main aspects of the experimental working conditions at the LHC will be described. In the second section, the ATLAS detector and subdetector structures will be described, with emphasis on the requirements imposed by the physics program, the machine features and the technology constrains. The last section addresses the physics signatures, the search strategies and the overall sensitivity for the discovery potential of SM Higgs boson processes in ATLAS.

3.1 The Large Hadron Collider

3.1.1 Machine parameters and Physics Program

The Large Hadron Collider [21] (LHC) at CERN is a proton–proton and heavy–ion collider with a centre–of–mass energy of 14 TeV when operating in the pp mode. The accelerator is presently under construction and is currently being installed in the LEP tunnel. A layout of the LHC injection and acceleration scheme is shown in Figure 3.1: protons will be produced in the 50 MeV proton linear accelerator, which will then be injected into the 1.4 GeV Proton Synchrotron Booster. The Proton Synchrotron (PS) itself will accelerate the protons to 25 GeV and will deliver a beam of 135 bunches, containing ~ 1011 protons, spaced at 25 ns. The Super Proton Synchrotron (SPS) will accelerate the protons to 450 GeV, ready to be injected into the LHC.

The first pp collisions at the LHC are expected to be observed in 2007. The circumference of the LEP tunnel is $\sim$ 27 Km and the magnetic field needed to keep the beam circulating in the machine is provided by 1232 superconducting dipoles providing a 8.4 Tesla magnetic field. Bunches of protons separated by 25 ns and with a RMS lenght of 75 mm intersect at four points where experiments are placed, see Figure 3.1: ATLAS and CMS are general purpose experiments designed for searches of new physics and precision measurements. LHCb is a B physics and CP violation dedicated detector while ALICE is a heavy ion experiment which will study the behaviour of nuclear matter at very high
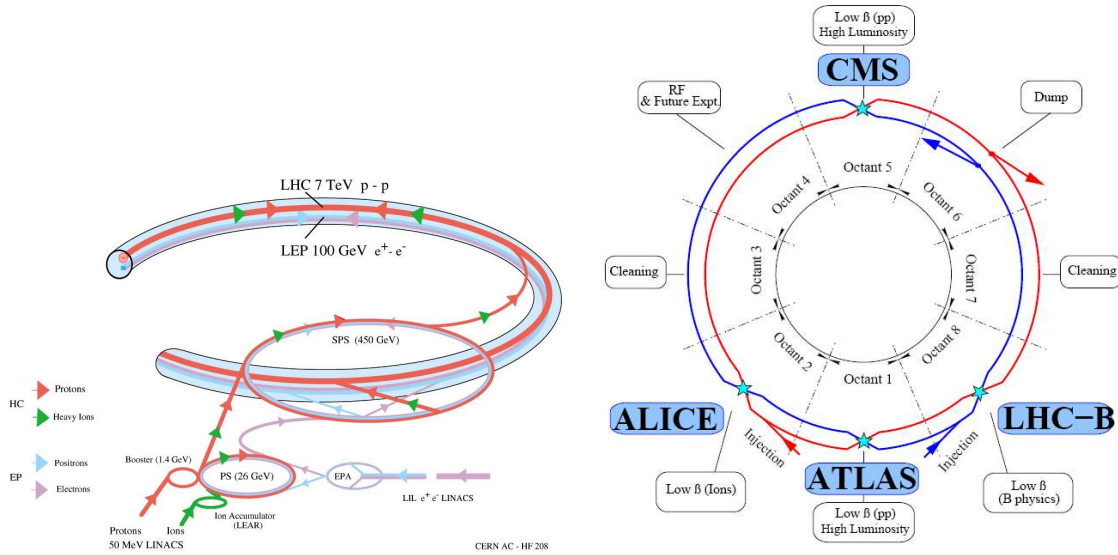
Figure 3.1: The LHC machine and its injection scheme (left). Layout of the LHC ring with the four interaction points (right).

energies and densities.

Two phases are forseen for the LHC operation: in the first few years of operation (low luminosity phase) the nominal luminosity is expected to be $2 \times 10^{33} \mathrm{cm}^{-2} \mathrm{s}^{-1}$ and then should reach $1 \times 10^{34} \mathrm{cm}^{-2} \mathrm{s}^{-1}$ (high luminosity phase). At low luminosity approximately 10 fb^{-1} of data per calendar year will be provided while in one year of operation at high luminosity will deliver 100 fb^{-1} of integrated luminosity. The machine will also be able to accelerate heavy ions allowing for example Pb–Pb collisions at 1150 TeV in the center–of–mass and luminosity up to $1 \times 10^{27} \mathrm{cm}^{-2} \mathrm{s}^{-1}$.

The LHC machine will allow a broad and ambitious physics program. The main topics are briefly summarized in the following list:

1. Search for a Standard Model Higgs boson over the full allowed mass range from the experimental limit set by LEP and Tevatron up to the theoretical upper bound of 1 TeV. If such a particle will be found, the LHC should be able to measure its mass and couplings with high precision.

2. Search for Supersymmetry and other physics beyond the Standard Model, such as leptoquarks or additional leptons, quarks and gauge bosons, up to masses of ~ 5 TeV.

3. Precise measurements of the W mass, of WWγ and WWZ Triple Gauge Couplings, and of the mass, the couplings and the decay properties of the top quark. Several QCD measurements will also be performed, such as the running of the strong coupling constant α_s over an unprecedented range of Q^2.

4. Detailed studies of the physics of B–mesons and of CP–violation in the B-hadron system. These measurements will be performed also (and with better sensitivity for some aspects) by the dedicated LHCb experiment [22].

5. Study of the phase transition from hadronic matter to a plasma of deconfined quarks and gluons. It is believed that the inverse transition (plasma→hadronic matter) happened in the universe 10μ s after the Big Bang. These studies will be performed by the dedicated ALICE experiment [23].

3.1.2 Experimental Environment

The LHC experiments will cope with complex working conditions due to high centre–of–mass energy and luminosity; the review presented in the following sections will be focused on pp collisions. The total cross section for inelastic, non–diffractive pp interactions at the LHC is expected to be around 80 mb at $\sqrt{14}$ TeV. At high luminosity the expected event rate is $\simeq 10^9$ ev/s. The physics events can be classified as follow:

1. *soft collisions*: they are due to long–distance collisions between the two incoming protons. The final state particles from soft collisions have large longitudinal momentum and a small transverse momentum with $< p_T > \simeq$ MeV. These events are also called <u>minimum bias events</u> and represent by far the majority of the pp collision.

2. *hard collisions*: they are due to short range interactions in which head–on collisions take place between two partons of the incoming protons. In these interactions the momentum transfer can be large, allowing the production of final states with high–p_T particles an the creation of massive new particles. At the LHC the high–p_T events are dominated by QCD jet production from quarks and gluons fragmentation in the final state which has a large cross section. Rare events with new particle production have a cross section which is usually some orders of magnitude smaller than the jet production and therefore hadronic final states can not be used to detect rare events such as SM Higgs boson decay, In these conditions, only decays into leptons and photons can be used even if their branching ratio is much smaller than decays into quarks.

At the LHC a bunch of $\sim 10^{11}$ protons will collide at each interaction point every 25 ns and therefore 25 soft collisions occurr in average at each bunch crossing giving rise to a total numer of 1000 charged particles in the region of $|\eta| < 2.5$. When an interesting high–p_T event takes place it is overlapped with $< 25 >$ soft interactions which constitute the <u>pile–up</u>. The detector parameters have been carefully tuned in order to reduce the impact of the pile–up on the physics searches.

3.2 The ATLAS Detector

The ATLAS[1] detector is currently under construction with many of its parts (calorimeter and magnet system) already in the cavern and starting the cosmic run commissioning phase (tile calorimeter). The overall ATLAS detector layout, shown in Figure 3.2, is incredibly complex and described in detail in the Technical Proposal [24] and Technical

---

[1]ATLAS is an acronym standing for A Toroidal LHC ApparatuS.
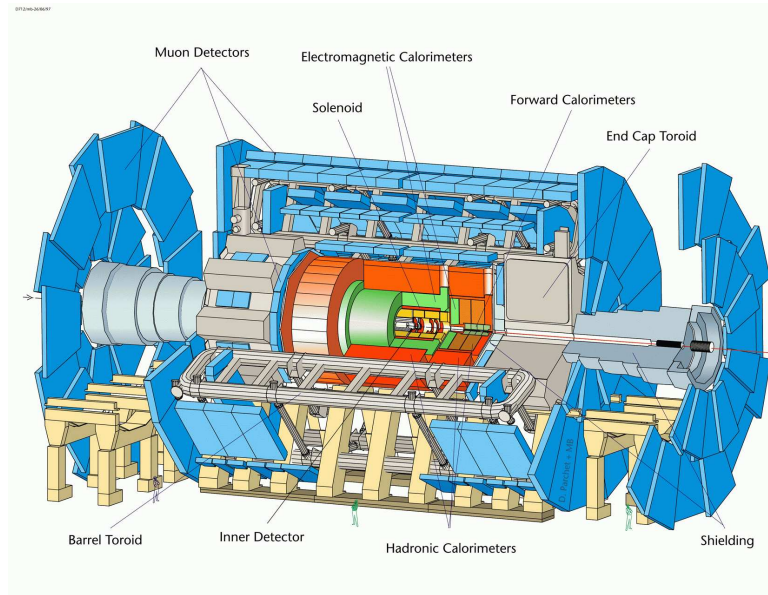
Figure 3.2: The ATLAS Detector.

Design Reports [25]. For completness, in this chapter a brief description of the detector components is given.

The basic design criteria of the detector include the following:

- Very good electromagnetic calorimetry for electron and photon identification and measurements, complemented by full–coverage hadronic calorimetry for accurate jet and missing transverse energy (E_T^{miss}) measurements;

- High–precision muon momentum measurements, with the capability to guarantee accurate measurements at the highest luminosity using the external muon spectrometer alone;

- Efficient tracking at high luminosity for high–p_T lepton–momentum measurements, electron and photon identification, τ–lepton and heavy–flavour identification, and full event reconstruction capability at lower luminosity;

- Large acceptance in pseudorapidity[2] (η) with almost full azimuthal angle (ϕ)[3] coverage everywhere. The azimuthal angle is measured around the beam axis, whereas pseudorapidity relates to the polar angle (θ) where θ is the angle from the z direction.

- Triggering and measurements of particles at low-p_T thresholds, providing high efficiencies for most physics processes of interest at LHC.

---

[2]The pseudorapiduty is defined as $\eta = -ln tan(\theta/2)$

[3]The azimuthal angle ϕ is measured around the beam axis and the polar angle θ from the beam axis (z direction)

The ATLAS detector is contained within a cylinder of about 44 m length and 22 m in diameter. The overall weight of the detector is $\sim$ 7000 Tons. Like most of the collider detectors, the ATLAS detector presents an onion–like structure. It can be split into three major sub–systems starting from the interaction point: the inner detector, the calorimeters and the muon spectrometer. The trigger and data acquisition system can be considered as a fourth component of the detector and it will be described in Chapter 4.

3.2.1 The Calorimeter

A calorimeter is almost always divided into an electromagnetic and a hadronic calorimeter. This distinction is possible because of the different interaction behaviour between the calorimeter and electron/photons on one side and hadrons on the other side. An extense overview of Calorimeters in particle physics is given in [26].

The ATLAS calorimeter, shown in Figure 3.3, consists of an electromagnetic (EM) calorimeter covering the pseudorapidity region $|\eta| < 3.2$, a hadronic barrel calorimeter covering $|\eta| < 1.7$, hadronic end–cap calorimeters covering $1.5 < |\eta| < 3.2$, and forward calorimeters covering $3.1 < |\eta| < 4.9$.

Identification of electrons and photons are the most important issues for the calorimeters. The rate of QCD–jets is high and to be able to get a clean sample of electrons with transverse momentum above 20 GeV a rejection of QCD–jets at the level of 10^6 is required. Such a rejection can be achieved with a calorimeter of the granularity in both the EM and hadronic part to identify isolated energy depositions from electrons/photons and to veto on hadronic energy behind the cluster in the EM calorimeter.

The design of the EM calorimeter is driven by requirements for energy and spatial resolution for Higgs processes involving decays to electrons and photons, $H \rightarrow ZZ^* \rightarrow 4e$ and $H \rightarrow \gamma\gamma$. The latter decay of a SM Higgs has a large background and a mass resolution of 1% is required [27]. This requires that the constant term of the energy resolution remains less than 1% and that the sampling term is kept at the level of $0.1/\sqrt[2]{E(GeV)}$. The dynamic range for the calorimeter ranges in transverse energy from around 1 GeV for electrons from B–meson decays to a few TeV for the decay of a heavy vector boson.

The reconstruction of jets is important for studies of quark compositeness. This sets stringent limits on the linearity of the hadronic calorimeter response at high energies. Also for the reconstruction of W bosons in hadronic decays the jet energy resolution is important. The discovery of a high mass Higgs decaying into a high p_T $W \rightarrow jetjet$ requires jet–jet mass reconstruction and forward jet tagging.

A measurement of missing transverse energy is a way to measure particles escaping the detector without interactions. This can either be neutrinos or stable supersymetric particles. For example, MSSM decays of $H^0 \rightarrow \tau\tau$ require good p_T^{miss} resolution and E_T^{miss} reconstruction. To identify missing transverse energy the calorimeter needs to have a good hermicity which means that the rapidity coverage has to reach $|\eta| = 5$ and any cracks in the detector for cables and cooling has to be avoided. Also the hadronic calorimeter needs to be thick enough to contain the energy of hadrons. Finally, bfor a good energy containment and resolution 11 absorption lenght of material in front of the muon system have been chosen.
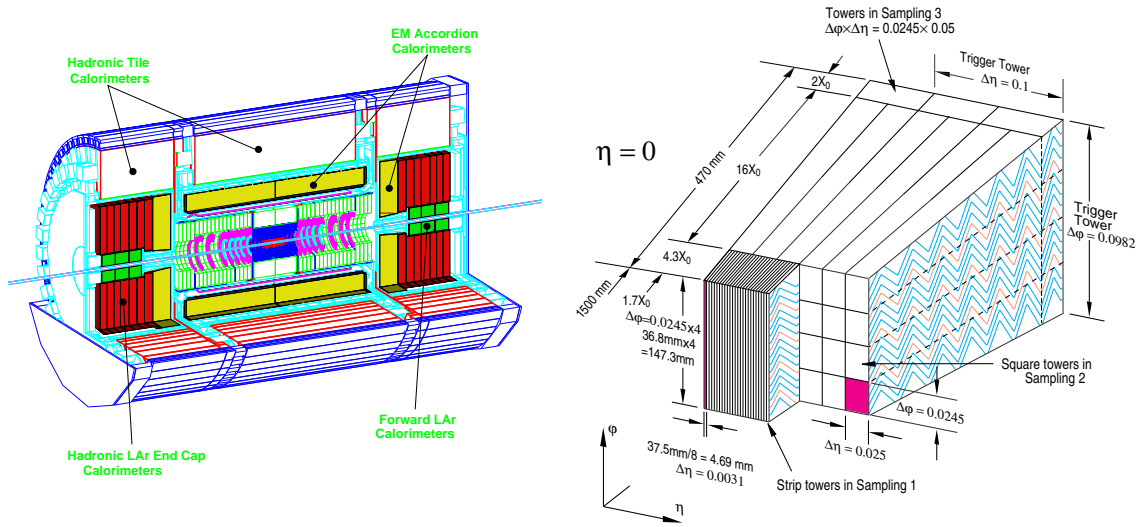
Figure 3.3: Three–dimensional cutaway view of the ATLAS calorimeter (left). The structure of the barrel accordion calorimeter, the presampler is infront of the accordion (right).

The Liquid Argon Calorimeter

The EM calorimeter is a lead liquid argon (LAr) sampling calorimeter. Layers of lead/stainless steel absorber plates and LAr are interspaced. The lead gives the shower development with its short radiation length and the secondary electrons create ionization in the narrow gaps of liquid argon. An inductive signal from the ionisation electrons drifting in the electric field across the gap–gap is registered by cooper electrodes.

To achieve a low capitance of the detecting elements and thereby a fast signal and to provide a complete ϕ symmetry, the lead plates have an accordion shape geometry as shown in Figure 3.3. In the region devoted to precision physics ($|\eta| < 2.5$) the EM calorimeter is segmented into four samplings:

- *Presampler*: A single thin layer of argon but no lead absorber in front. The purpose is to correct for the energy loss in the solenoid and cryostat wall.

- *1st Sampling*: The first sampling has a depth of $4.3X_0$. The readout is as seen in Figure 3.3 in thin η strips which provides an excellent resolution in the η coordinate for γ/π^0 separation. The ϕ coordinate is not suited for this since converted photons will open up in the magnetic field and produce clusters with widths similar to π^0 clusters.

- *2nd Sampling*: The majority of the energy is deposited in the $16X_0$ of the second sampling. Clusters with energy below 50 GeV are fully contained. For the position measurement of the cluster the two coordinates are equally important resulting in square cells of size $\Delta\eta \times \Delta\phi = 0.0245 \times 0.0245$

- *3rd Sampling*: Only the highest energy electrons will reach this deep in the detector. The clusters are at this point wide and the cell size can be doubled in the η direction without loss of resolution.

For the region of $|\eta| > 2.5$, i.e. for the end–cap inner wheel, the calorimeter is segmented in two longitudinal sections and has a coarser later granularity than for the rest of the acceptance which is sufficient to satisfy the requirements (reconstruction of jets and measurement of E_T^{miss}). In the end–cap there is less material in front of the calorimeter therefore the presampler can be avoided. The end–cap EM calorimeters start at $|\eta| = 1.5$ and continue down to $|\eta| = 3.2$ but with an increased cell size above $|\eta| = 2.5$. There is a crack with bad energy resolution where the end–cap and barrel calorimeters meet.

In the forward region the hadronic calorimeter is also of liquid argon technology to withstand the high radiation levels. The design is simpler than the EM calorimeter and has parallel copper plates as absorbers placed perpendicular to the beam.

The very forward hadronic calorimeter with a coverage down to $|\eta| = 4.9$ is made of copper/tungsten. The choice of these material is necessary to limit the width and depth of the showers from high energy jets close to the beam pipe, and to keep the background level low in the surrounding calorimeters from particles spraying out from the forward region.

The Tile Calorimeter

The tile calorimeter of ATLAS is a hadron calorimeter using iron as the absorber and scintillating tiles as the active material. The calorimeter is in the central rapidity region reaching out to $|\eta| = 1.7$ where the liquid argon calorimeter takes over. The resolution of the hadronic calorimeter is $0.5/(E)^{1/2} + 3\%$ for $|\eta| < 3$ and $1/(E)^{1/2} + 10\%$ for $3 < |\eta| < 5$.

The scintillator tiles are placed such that the shower passes through them from the side to improve the e/h[4] ratio. The light created in the scintillators is read out with wavelenght shifting fibres to photomultipliers placed on the outside of the calorimeter. The fibres absorb the blue light from the scintillators and reemit it at longer wavelenghts where it reaches the photomultipliers through total reflection inside the fibers.

To improve the hermicity of the hadronic calorimeter two plug in each side are inserted in the region where the cables and cooling from the EM calorimeter and the Inner Detector pass through. The crack scintillator, a pure scintillator with no steel absorber, is one of them. It plays an important role for the EM calorimeter as well since it is placed just in the difficult transition region between the barrel and end–cap EM calorimeter.

3.2.2 The Inner Detector

The Inner Detector (ID) is the innermost part of ATLAS. With a combination of high–precision, high–granularity layers in the inner part and straw tubes in the outer part, it can reconstruct the track of charged particles in a solenoidal magnetic field of 2 T with a coverage that extends up to $\eta = 2.5$.

The main requirements for the Inner Detector are:

---

[4]The ratio between the response of the calorimeter for the purely hadronic and the purely electromagnetic part of the shower is called e/h
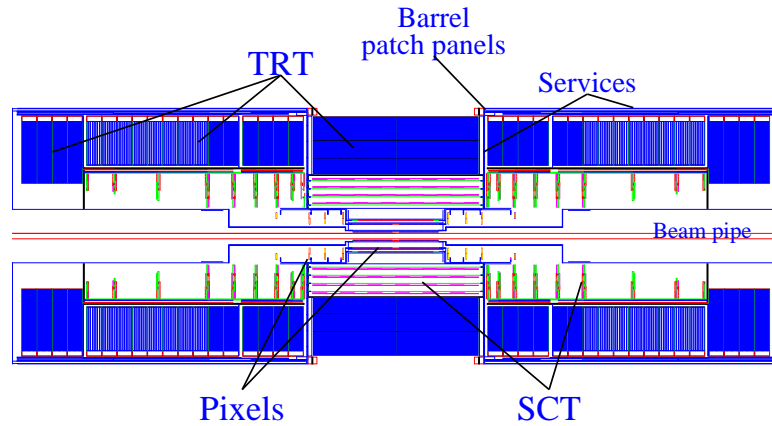
Figure 3.4: A side view of the Inner Detector layout.

- Tracking efficiency of $> 95\%$ over the full coverage for isolated tracks with $p_T > 5$ GeV, with fake–track rates less than 1% of signal rates.

- Identification of individual particles in dense jets where the calorimeter cannot resolve the individual particles.

- Momentum measurement in a large momentum range. Below $p_T = 0.5$ GeV the particles loop in the magnetic field and reconstruction is not possible. This lower limit affects the reconstruction of converted photons and J/Ψ decays.

- Distinguish between electrons and photons which create similar cluster in the EM calorimeter.

- Charge identification of particles with large transverse momentum for the identification of a possible Z' decay.

- Decay length reconstruction used for CP–violation studies in the B–system and for a B_s^0 mixing measurement.

- Tagging of jets originating from high energy b–quarks. The tagging is done by secondary vertex identification and through the identification of leptons from semileptonic B–meson decays.

- Momentum measurement of low energy muons which have large multiplicity scattering in the hadronic calorimeter.

- Electron/jet separation in addition to the separation already provided by the calorimeter.

- Identification of the primary vertex in the presence of many vertices from overlying minimum bias events.

The momentum and vertex resolution requirements from physics call for high–precision measurements to be made with fine–granularity detectors. Semiconductor tracking detectors, using silicon microstrip (SCT) and pixel technologies are used. The highest granularity is achieved around the vertex region using semi–conductor pixel detectors. The total number of precision layers must be limited because of the material they indtroduce, and because of their high cost. Photon conversions, bremsstrahlung from electrons and nuclear interactions with pions all cause a degraded calorimeter performance. Typically, three pixel layers and eight strip layers are crossed by each track. A large number of tracking points (typically 36 per track) is provided by the straw tube tracker (TRT) in the outer part, which provides continuous track–following with much less material per point and a lower cost. The combination of the two techniques gives very robust pattern recognition and high precision in both η and ϕ coordinates.

In the barrel part of the Inner Detector where $|\eta| \geq 1$ all of the detecting elements are ordered in cylindrical structures while the two end–caps have the detecting elements placed in wheels. This assures that the particles pass all detecting elements with large incident angles.

The Silicon Detectors

Two technologies are used for the ATLAS semiconductor tracker (SCT): pixel detectors placed closest to the beam pipe and silicon strip detectors placed further away.

The SCT system is designed to provide eight precision measurements per track in the intermidiate radial range, contributing to the measurement of momentum, impact parameter and vertex position, as well as providing good pattern recognition by the use of high granularity.

The silicon strip detectors have a n type bulk with a single sided readout of $n+$ strips. This choice is believed to be the most radiation resistent. In each of the layers of the detector two single sided detectors are placed back to back. In one layer the strips are parallel to the beam pipe thus measuring the ϕ coordinate directly. The strips on the back side reconstruct the z(r) coordinate in the barrel (end–cap). Each strip in the detecting element will have a length of 12 cm and a width of 80 μm.

The pixel detector system is designed to provide a very high–granularity, and high–precision set of measurements as close to the interaction point as possible. The system provides three precision measurements over the full acceptance, and mostly determines the impact parameter resolution. The system contains 140 million square detecting elements, each 50 μm in the Rϕ direction and 300 μm in z, thus giving a 2–dimensional coordinate with just one layer. The best resolution is in the ϕ direction. The pixel device is placed in the layers closest to the primary vertex because of the high spatial resolution.

The most important requirements for the pixel detectors is the determination of secondary vertexes for the identification of B–meson decays, for b–tagging in top physics. It is important for pattern recognition since it has very low occupancy in spite of the close placement to the primavery vertex. To fulfill this requirement the first pixel layer is placed as close as possible to the beam pipe.

The Transition Radiation Tracker

The transition radiation tracker (TRT) is based on the use of straw detectors, which can operate at the very high rates expected at the LHC by virtue of their small diameter and the isolation of wires within individual gas volumes.

Electron identification capability is added by employing xenon gas to detect transition–radiation photons created in a radiator between the straws. This technique is intinsically radiation hard, and allows a large number of measurements, typically 36, to be made on every track at a modest cost. However, the detector must cope with a high occupancy and high counting rates at the LHC design luminosity. The large number of hits on the tracks is powerful in the pattern recognition state where tracks are to be found in the detector. The TRT provides additional discrimination between electrons and hadrons as described in Chapter 9.

In total there are around 370 000 straws with 4 mm diameter in the TRT, which are placed radially in the end–cap and along the beam axis in the barrel region; these orientations are chosen to maximise the number of straws passed in all directions pointing away from the interaction point. The straws are filled with a xenon gas mixture for the absorption of transition radiation which also enables a faster drift–time for electrons, providing higher spatial resoultion and reducing the influence from neighboring bunch crossings at the LHC. In the center of the straw is a 30 μm gold covered tungsten wire.

3.2.3 The Muon System

The muon system serves a double purpose as a trigger to select events with high energy muons and as a precision muon spectrometer. The general layout of the muon system is shown in Figure 3.5.

The muon system has to fullfil the following requirements:

- A good transverse momentum resolution in the low p_T region. The limit is defined by the ability to detect the $H \to ZZ^*$ decay in the muon channel with a high supression of the background. A resolution of around 1% is required.

- Sufficient resolution at high p_T for good charge identification for the identification of a $Z^{'} \to \mu\mu$ process.

- A rapidity coverage of $\eta < 3$ and an hermetic system to prevent particles to escape through holes.

- Measurement of spatial coordinates in two dimensions to provide good mass resolution.

- A low rate of both punch through hadrons and fake tracks.

Particles from the primary vertex traverse three sets of muon chambers. In the barrel part of the detector one set of chambers is placed inside the toroid and the momentum is measured from the sagitta of the tracks. In the end–caps, where the toroid cryostat prevents chambers from being placed inside the magnetic field, the muon momentum is measured from the difference in entry and exit angle of the magnet.
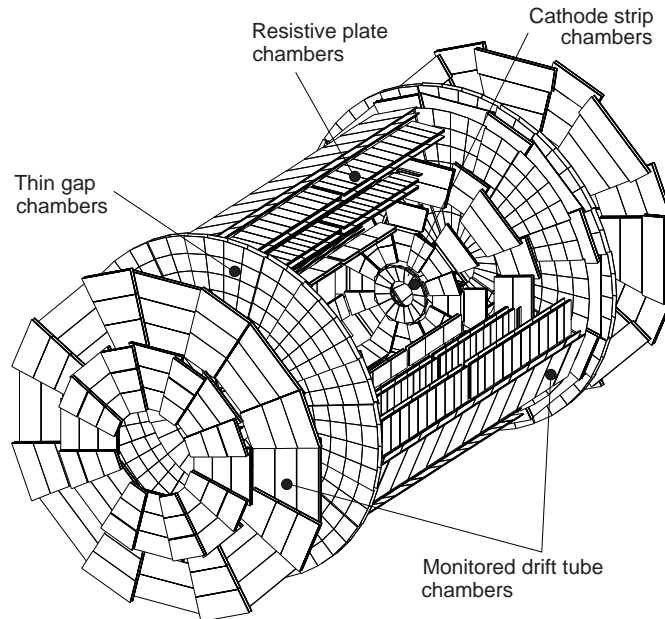
Figure 3.5: The ATLAS Muon Detector.

The Monitored Drift Tube (MDT) chambers are proportional chambers made out of aluminium tubes of 30 mm diameter and lengths varying from 70 cm to 630 cm. To measure the coordinate in the bending plane of the magnet the tubes are placed transverse to the beam axis. In order to reduce the level of fake tracks reconstructed from random associations of background hits each set of MDTs are required 2 superlayers each with 3 or 4 layers of tubes. Each MDT has a resolution of 80 μm which results in a momentum resolution $\Delta p_T/p_T < 10^{-4} \cdot p$ for tracks with $p_T > 300$ GeV.

Cathode Strip Chambers (CSC) with finer granularity compared to the MDT are used in the forward region, where the track density is higher, to find tracks. The CSCs are multiwire proportional chambers with a wire spacing of 2.5 mm.

The drift tubes have a large diameter which results in a maximum drift –time of 480 ns which is much longer than the 25 ns spacing between the bunch crossings. For this reason special layers of trigger chambers are needed for the trigger.

A Resistive Plate Chamber (RPC) has a gas–gap between two resistive bakelite plates with metal strips.

Only the trigger chambers are read out to the Level1 trigger. The lower spacial resolution of the trigger chambers provide a reduced but sufficient momentum resolution. The MDTs only give the η coordinate while the trigger chambers also provide the ϕ coordinate for the tracks.

3.2.4   The Magnet System

The ATLAS superconducting magnet system is an arragement of a central solenoid providing the Inner Detector with a magnetic field, surrounded by a system of three large air–core toroids generating the magnetic field for the muon spectrometer.

The solenoid magnet is placed inside the electromagnetic calorimeter. This is different from most other detector designs where the magnet is placed outside the EM calorimeter. A small magnetic field also reduces the tranverse spread of showers. The major problem is the increased amount of material in front of the calorimeter which causes many particles to start showering before they reach the active part of the calorimeter.

The solenoid is a superconducting magnet are indirectly cooled by helium at 4.5 K. To reduce the material, the magnet, does not have a separate cryostat with the liquid argon calorimeter thus saving two cryostat walls. The lenght is considerably shorter than the inner tracking system. This is a result of a compromise: a short coil reduces the material in front of the calorimeter and a long coil makes the magnetic field more uniform in the Inner Detector. The magnetic field along the z–direction is 2 T at the interaction point.

The toroid magnet is divided into one barrel part and two forward regions. Each of the three toroids consists of eight coils assembled radially and symmetrically around the beam axis. The toroid coils are of a flat racetrack type with two double–pancake windings made of 20.5 kA aluminium–stabilized NbTi superconductor and are in separate cryostats for the barrel. In the forward region the toroid field is also formed by eight superconducting coils but they are placed in a common cryostat.

WIth a toroid field, particles will across the complete pseudorapidity range, almost perpendicular to the field. This means that the field integral, which is the important factor for momentum resolution, can be kept high even in the forward region. The low number of coils to form the toroid field results in a field strength that varies strongly with the ϕ coordinate. The field in the barrel is 2 T and in the end–caps from 4 T.

3.3   SM Higgs boson Searches at the LHC

At the LHC the Standard Model Higgs boson is expected to be produced mainly through the processes shown in Figure 3.6: gluon–gluon fusion, vector boson fusion and WH, ZH and $t\bar{t}$H associated production. The cross–sections for the mentioned processes are reported in Figure 3.7 as a function of the Higgs mass. The gluon–gluon fusion through a top–quark loop is the dominant production process in the full expected Higgs mass range. Vector boson (VBF) WW and ZZ fusion becomes increasingly important with increasing Higgs boson masses, attaining a cross–section similar to that of gluon–gluon fusion for $m_H \sim 1$ TeV. The VBF production mode gives a very distictive signature that can be exploited to suppress the large background: the Higgs boson is accompained by two jets in the forward regions of the detector and in addition the central jet activity is suppressed. The associated Higgs production with a $t\bar{t}$ pair or a W/Z boson has a significantly smaller cross section, however some of the possible final states with a lepton coming from the decay of the accompanying particle can be relatively easy to extract from the background.

It should be noticed that the total production cross–section is larger than 100 fb even for Higgs masses lower than 1 TeV. Therefore more than $2 \cdot 10^3$ events are expected

to be produced in one year of running at low luminosity and more than 10^4 events in one year of running at high luminosity for $m_H \sim 1$ TeV.
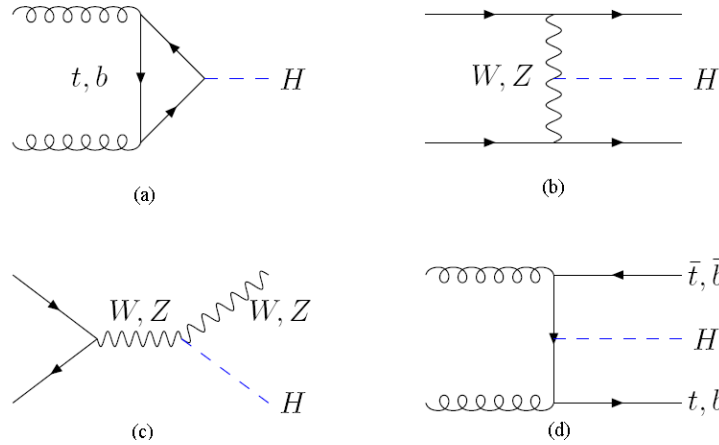
Figure 3.6: Main Feynman diagrams contributing to the production of the SM Higgs boson at the LHC: (a) gluon–gluon fusion (b) Vector Boson Fusion (VBF) in WW and ZZ fusion (c) asociated WH and WZ (d) associated $t\bar{t}$H.
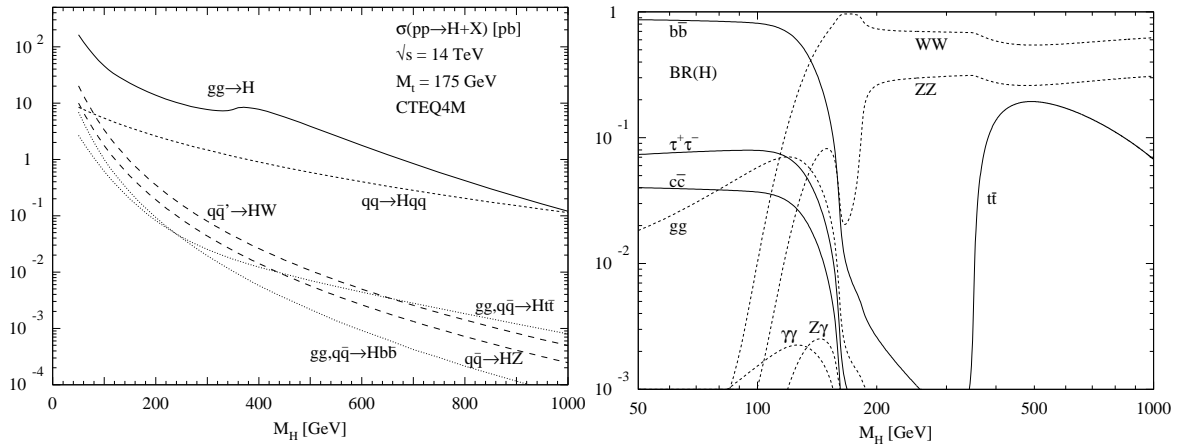
Figure 3.7: The cross section for $pp \rightarrow H + X$ as a function of the Standard Model Higgs boson mass at the LHC [28] (left). Branching ratios of the dominant decay modes of the standard model Higgs boson in the theoretically allowed mass range (right).

3.3.1   Search Strategy

At the LHC many possible decay channels could be used to look for a Standard Model Higgs boson depending on the Higgs boson mass, a complete picture is shown in Figure 3.7. The most promising channels which will be used at the LHC in the Higgs boson search can be classified in three main categories depending on the m_H:

1. *Low mass region decays* for $m_H < 130$ GeV

2. *Intermediate mass region decays* for 130 GeV$< m_H < m_Z$

3. *High mass region decays* for $m_H > m_Z$

In the following sections the main Higgs boson decay channels in the various mass range will be reviewed [29, 30, 31, 32].

Low mass region

In the low mass region two experimentally important decay modes have been studied [25]: $H \rightarrow b\bar{b}$ and $H \rightarrow \gamma\gamma$. The $H \rightarrow b\bar{b}$ decay has a branching ratio close to 100% since the Higgs boson couplings to fermions are proportional to the fermion masses and the b quarks are the most massive fermions kinematically accessible in this region. The $H \rightarrow b\bar{b}$ decays from inclusive production have a large cross section ($\simeq 20$ pb) but since the signal to background ratio is less than 10^{-5} it will be impossible to detect this process above the QCD background. Only $H \rightarrow b\bar{b}$ from associated production with $t\bar{t}$, and Z can be observed: the cross section is smaller ($\simeq 1$ pb) but final states with one lepton coming from the decay of the accompanying particle can be selected from the background.

The $H \rightarrow \gamma\gamma$ decay has a very small cross section ($\simeq 50$ fb) but the signal to background is of the order of 10^{-3}: for this reason this rare decay mode is expected to be one of the most promising in the low mass case and it is also considered one of the benchmark for the calorimeter detector performance.

A detailed study has been recently carried out on the $H \rightarrow \tau\tau$ decay with a Higgs boson coming from VBF [31]: in this study both double leptonic decay mode ($qqH \rightarrow qq\tau\tau \rightarrow qql^+\nu\nu l^-\nu\nu$) and lepton–hadron decay mode ($qqH \rightarrow qq\tau\tau \rightarrow qql^{\pm}\nu\nu$ had ν) have been considered. The results of the analysis demostrates that taking into account the contribution of this channel a 5σ signal significance can be achieved with only 10 fb^{-1} of integrated luminosity for $m_H \leq 120$ GeV (see next section).

Intermediate mass region

In the intermediate mass range (130 GeV$< m_H < m_Z$) the main discovery channels are expected to be [25]: $H \rightarrow ZZ^* \rightarrow 4l$ and $H \rightarrow WW^* \rightarrow l\nu l\nu$.

The Higgs $H \rightarrow ZZ^* \rightarrow 4l$ process gives rise to a very distinctive four lepton final state. In order to achieve a clear reconstruction of the mass peak, only electrons and muons are selected in the final state. The main irreducible background consists of $pp \rightarrow ZZ \rightarrow 4l$ continium. Potentially dangerous reducible background sources are due to the $t\bar{t} \rightarrow 4l + X$ and the $Zb\bar{b} \rightarrow 4l + X$ decays: in the first case two leptons come from the W produced in the $t \rightarrow Wb$ and two leptons from the semileptonic decay of the b quark; in the second case the two leptons come from the Z decay and two from the b quark decay. These reducible background sources can be reduced with a proper selection. For example, the request of a lepton pair with an invariant mass consistent with the Z mass is efficient against the $t\bar{t}$ background. The lepton isolation cut and the requirement that all leptons come from the interaction vertex are expected to be efficient for the selection of leptons coming from the semileptonic decay of the b quark.

The $H \to WW^* \to l\nu l\nu$ becomes a promising discovery channel for a Higgs mass around 170 GeV [33]. For such value of the Higgs boson mass, the signal significance of the $H \to ZZ^* \to 4l$ decay is reduced due to the fact that the WW decay mode opens up. Considering the WW channel, the presence of a Higgs boson can only be deduced from an excess of events in the transverse mass plot over the expected background (the knowledge of the total background yield is therefore crucial for this channel). There are many irreducible and reducible background contributions: a complete list of the main expected background sources together with the analysis details can be found in [25]. The associated production of a Higgs and a W boson with $H \to WW^* \to l\nu l\nu$ and $W \to l\nu$ has also been studied [34]: this channel provides a distinctive signature with three isolated leptons in the final state and low expected background [25].

Recently WW decays of a Higgs boson from a VBF production process has been studied in detail [31, 35]: both the di–lepton ($H \to WW^* \to l\nu l\nu$) and the $l\nu jj$ final states have been considered. The latter was already established in the past as a potential discovery channel for a heavy Higgs boson and has now been extended at the intermediate mass region. Exploiting the distinctive signature typical of the Higgs boson production via VBF with two jets at large η and low jet activity in the central region, a signal significance greater than 5 can be achieved for 140 GeV$< m_H < 190$ GeV even with an integrated luminosity of 10 fb^{-1}.

At the LHC the difficulty to extract the Higgs signal from the huge QCD background dictates the choice of channels with leptons and photons. For the low mass region, $m_H < 2m_Z$, the following Higgs decay channels include lepton and gammas in the final state: $H \to \gamma\gamma$, $H \to ZZ^* \to 4l$, and $H \to WW^* \to l\nu l\nu$ decay via VBF. The potential to trigger on these channels has been studied in Chapter 8.3.

High mass region

The case of a Higgs boson with a mass $2m_Z$ GeV$< m_H < 600$ GeV is the LHC best possible scenario: in this mass range the $H \to ZZ \to 4l$ channel gives rise to a gold plated four lepton final state. The background, which is dominated by the continuum production of Z boson pairs, is expected to be smaller than the signal. In this channel the Higgs boson would appear as a clear peak on the invariant mass of the four lepton on top of the background: in order to obtain a clean reconstruction of the Higgs mass peak only electrons and muons are required in the final state. A detailed review of this analysis can be found in [25]. A signal significance greater than 20 is expected to be achieved with this channel in the 200 GeV$\leq m_H \leq 500$ GeV mass range for an integrated luminosity of 30 fb^{-1}.

For Higgs bosons heavier than $500 - 600$ GeV the following two decays become increasingly important: $H \to ZZ \to ll\nu\nu$ and $H \to WW \to l\nu jj$. Both channels would be observable only through the requirement of two tag jets in the forward region ($2 < \eta < 5$) which selects the $qq \to qqH$ production process and strongly rejects the background from $t\bar{t}$ and W/Z+jet production. The studies described in [36, 37] demostrate that a SM Higgs boson would be observed in the $H \to ZZ \to ll\nu\nu$ and $H \to WW \to l\nu jj$ for a Higgs mass up to 1 TeV.

3.3.2 Discovery Potential in ATLAS

The overall sensitivity for the discovery of a Standard Model Higgs boson over the LHC accessible mass range is reported in Figure 3.8 for an integrated luminosity of 30 and 100 fb^{-1} respectively. A 5σ discovery can be achieved over the full mass range with 30 fb^{-1} of integrated luminosity: such luminosity can be accumulated in a few years of running in the low luminosity phase of the machine. The requirements on the detector performance in terms of energy, angular resolution, hermeticity, trigger and particle identification capibility will be crucial for the discovery of a Standard Model Higgs boson in the low and intermediate mass range. For $m_H > 2m_Z$ the main discovery channel is the four lepton channel and the background for this decay is expected to be small. Moreover, for a $m_H > 300$ GeV the Higgs width is expected to be larger than the detector resolution and the requirements on the detector performance are less demanding.
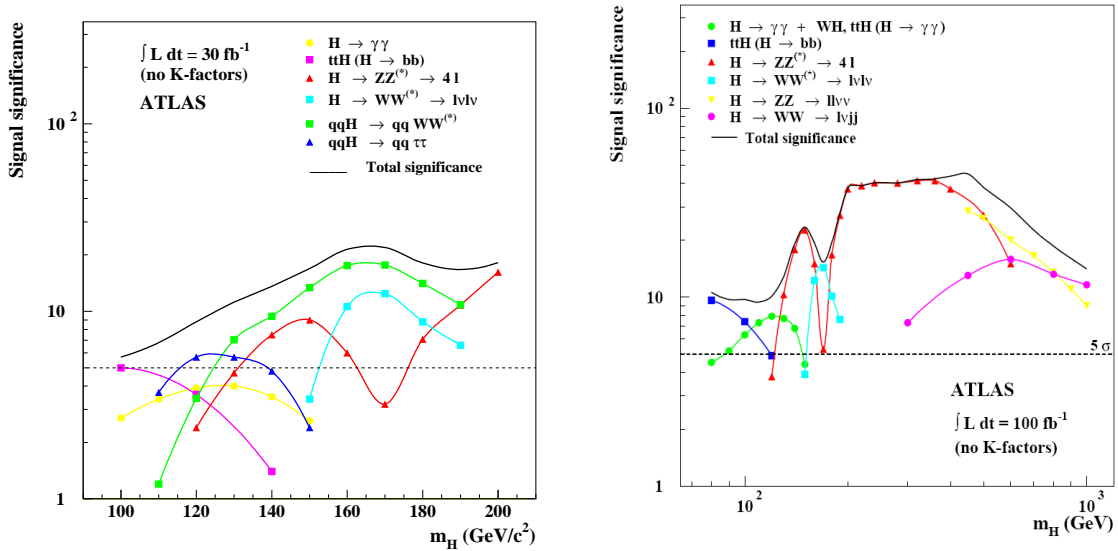
Figure 3.8: Expected signal significance for a Standard Model Higgs boson in ATLAS as a function of the Higgs mass for an integrated luminosity of 30 fb^{-1} (left) and 100 fb^{-1} (right plot). The most important discovery channels have been taken into account.

It should be noticed that no K–factors have been included in the evaluation of the signal significance because they were not fully available for both signal and background. Recent improvements in NLO computation for signals and backgrounds ([38, 39]) confirm that better significance can be achieved including next to leading order (NLO) corrections. It should be clear from Figure 3.8 that at the LHC over almost the full mass range more than one channel should be observed giving robustness to a discovery claim.

Chapter 4

The ATLAS Trigger System

In this chapter, a brief summary of the ATLAS three level Trigger system (Level1, Level2, and Event Filter) will be provided. The online triggering system will reduce the the bunch crossing rate of 40 MHz to approximately 200 Hz at mass storage. A description of the event data selection and classification starting from the Level1 trigger and passsing through the Level2 and Event Filter selections steps will be provided with emphasis on the common HLT event selection software.

4.1 General TDAQ Architecture

The Trigger system of ATLAS has been organized in three levels: level–1 (Level1), level–2 (Level2) and Event Filter (EF). A functional view of the DataAcquisition (DAQ) system with the expected rates is given in Figure 4.1. The online triggering system will reduce the the bunch crossing rate of 40 MHz to approximately 200 Hz at mass storage.

The Trigger/DAQ system has been subdivided into four main functional elements, namely: the Level1 trigger, The High–Level triggers (HLT), the Data Acquisition (DAQ) and the Detector Control System (DCS).

The *Level1* trigger is hardware based and reduces the event rate from the bunch crossing to 75 kHz.

The *High Level Trigger* system (composed of Level2 trigger and Event Filter) is responsible for the post–level1 event selection and filtering involving a rate reduction of a factor of several hundred, and for the classification of all accepted events. It will reduce the event rate which will be put to mass storage to about 200 Hz.

The *DAQ* is the system which deals with the movement of data from the RODs to mass storage and with the initialization, control and monitoring of the experiment data taking, and during testing and calibration runs. This system has been split into two systems: The Data Flow system and the Online System.

The Detector Control System (DCS) is responsible for the coherent and safe operation of the ATLAS detectors and associated systems. It interfaces with the ATLAS subdetectors, the LHC machine and the CERN infrastructure and provides supervision and monitoring of non–physics event data.

A detailed description of all the TDAQ systems can be found in [40], [41]. Here

the main components will be briefly described and emphasis will be put on the selection criteria at the different levels, which allow the ATLAS physics goals to be achieved.
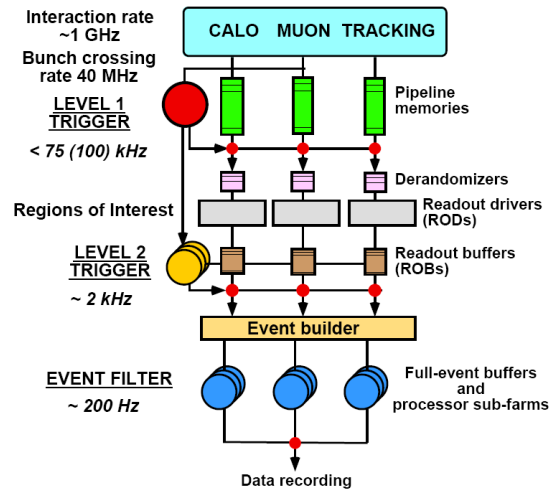
Figure 4.1: The ATLAS Trigger System.

4.2 The Level1 Trigger

The Level1 Trigger is implemented in custom hardware [41]. It reduces the event rate from the 40 MHz bunch–crossing rate to about 75 kHz (can be upgraded to 100 kHz). Since a decision cannot be reached in the 25 ns between two bunch crossings the detectors store the event data from all subdetectors (about 10^8 electronic channels) in pipelined buffers until the Level1 decision is made. The pipelines allow a fixed latency of up to 25 μs for a trigger decision, after which accepted events are forwarded to detector–specific Read Out Drivers (ROD). These drivers in turn send their data to detector independent Read Out Buffers (ROB) where the data are stored until a Level2 decision is reached. It is forseen that there will be a total of about 1700 ROBs.

The Level1 trigger only uses information from the calorimeters and muon detectors to reach its decision. Results from both the calorimeter and the muon triggers are combined in the Central Trigger Processor (CTP) which makes the final decision based on multiplicities of identified trigger objects for various p_T thresholds and information on global–energy variables (e.g. missing E_T). The decisions are forwarded via the Timing, Trigger and Control (TTC) system to the front–end electronics. For accepted events the Level1 trigger sends information to the Region Of Interest Builder (RoIB) which assembles a list of RoIs for the event, to be used by Level2. The information covers both RoIs that were used in making the LVL1 decision (*primary RoIs*) and, possibly, additional RoIs that were identified (*secondary RoIs*). The Level1 calorimeter trigger is described in section 5.1.1.

4.2.1 The Region of Interest Mechanism

An important piece of the startegy of the ATLAS trigger relies on the Region–of–Interest (RoI) mechanism for which the Level2 trigger makes use of the information provided by the Level1 trigger in localized region of the calorimeter and muon sub–detectors. This process is shown schematically in Figure 4.2.

The information contained in the RoI typically include the position (η and ϕ) and the p_T of the candidate objects as well as energy sums. Candidate objects selected by the Level1 can be high–p_T muons, electrons or photons, hadrons or taus, and jets. The energy sums include the missing–E_T vector and the scalar E_T value. For all selected Level1 events, the RoI information is sent to the Level2 using a dedicated data path. Making use of this RoI information, the Level2 algorithms only transfer the necessary ROBs in order to arrive quickly at a Level2 decision. It is important to note that all the data from all the sub–detectors with full granularity is available for the Level2 algorithms if necessary. However, typically only a small fraction of the detector, centred around the RoI information selected by the Level1, is needed by the Level2 algorithms. On average there are a few RoI per event (~ 1.4) and as a consequence to this mechanism only a few percent of the total event data is required at the Level2 stage. On the other hand, even though the bandwidth requirements on the Data Acquisition system is much reduced, it makes for a more complex system. The retrieval of data by the RoI mechanism necessary to perform the Level2 desicion will be discussed in section 3.3.1.
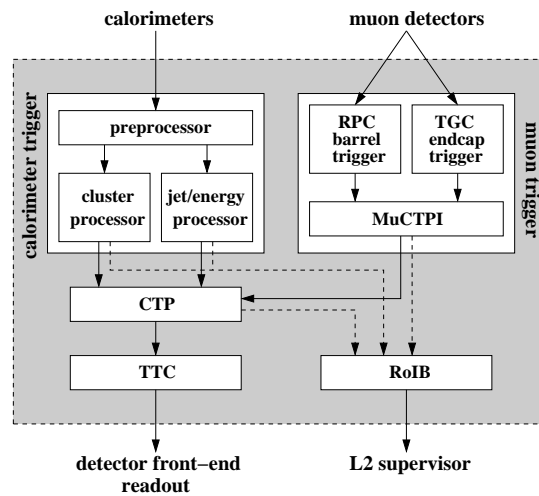

Figure 4.2: The Block Diagram of the Level1 Trigger.

4.3 The High Level Trigger

The High–Level Trigger (HLT) contains the second and third stages of the event selection. It comprises three main parts: The **Level2** system (Level2), the **Event Filter** (EF), and the **Event Selection Software** (ESS). The HLT system is implemented as a

Level2 processor farm and multiple EF subfarms after the event building stage. Level2 deals with a much higher event rate, but only a fraction of the full event data. The EF works on full events but at a much lower rate. Overall the network bandwidth needed is in the same order of magnitude for both systems. The Level2 and the EF combined will give an event rate reduction factor of order 1000 to 200 Hz at mass storage. This value is limited by the offline computing power and the storage capability of the experiment. This output rate must include the contribution from all physics channels. The HLT will provide a rate reduction factor of $\sim 10^3$ from which the Level2 contribution is expected to be ~ 100 resulting in a input rate for the EF of ~ 2 kHz. The sharing of the selection task between Level2 and EF remains to be optimized. A preliminary study will be presented in Chapter 7.1. The average event size is assumed to be about 1.5 Mbyte.

Although the Level2 and EF systems are different, they use a **common software architecture** for the event selection across Level2, EF and offline studies, the ATHENA offline framework [42]. This facilitates use of common infrastructure (such as detector calibration, and alignement data) and simplifies offline studies and development of the HLT algorithms. Furthermore, it clearly enhances the HLT flexibility in dealing with changes in the LHC running conditions when it is possible to migrate algorithms freely between offline environment and Event Filter and between Event Filter and Level2 trigger.

The performance constraints imposed by the HLT are most stringent for the Level2 trigger. The Level2 software needs to be able to handle a data input rate of up to 75 kHz and to sustain a data output rate of O(2) kHz error–free and deadtime–free for extended periods of time in an average latency of 10 ms. Requirements of such stringency with respect to speed and robustness are usually not met by software designed for pure offline use. An additional complication arises from the need for multi–threading in the Level2 trigger, in order to keep the idle time of the CPUs in the Level2 Linux PC farm to a minimum, each CPU processes in parallel three different events. Therefore, the Level2 system runs in a **special multi–threaded environment**. Hence Athena cannot be used as the HLT framework for the Level2 trigger. In order to comply nonetheless with the design goal that the Level2 event selection software be usable with the Athena framework for development and maintenance purposes, an interface layer between the HLT selection and the HLT Data Flow software was implemented [43].

The HLT selection chain is based on the concept of **seeded reconstruction**, particularly fundamental at Level2. The Level2 is seeded by the Level1 result, which contains the Level1 trigger type and the information about number of primary RoIs that caused the Level1 accept, plus secondary RoIs not used for the Level1 accept. The EF selection is seeded by the Level2 result or also directly from the Level1 result. The Level2 and EF results, containing the physics signatures from the trigger menu that were satisfied and higher level reconstruction objects, will be appended to the raw event data.

4.3.1 The Data Flow

The flow of data in the ATLAS online trigger is as follows [44, 45, 46]. Data for events accepted by the LVL1 trigger are sent from the detector front-end electronics to the ROSs (the Read Out System stores the event data until the Level2 trigger has made its final decision), containing ~ 1700 ROBs (Read Out Buffers). The ROB receive their

input via uni-directional read–out links after an event has been accepted by LVL1 The ROB implements a flexible buffer manager which anwers request for event data from Level2 or the event builder. In parallel, information on the location of RoIs identified by LVL1 is sent to the Level2 Supervisor to guide the Level2 event selection. Figure 4.3 shows the TDAQ architectural components used to perform the flow of data.
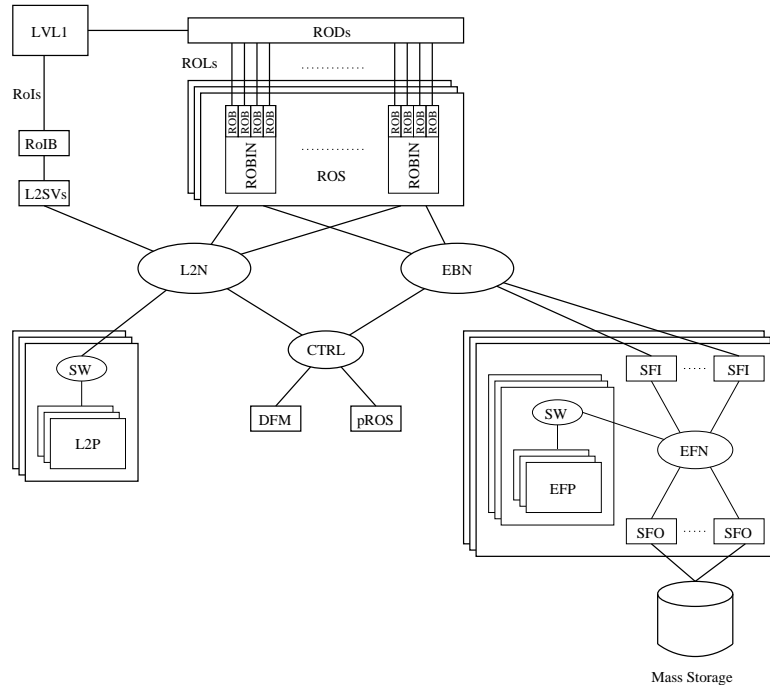
Figure 4.3: General TDAQ architectural components and their relations.

The Level2 Supervisor sends the LVL1 result to the L2PU, where the Level2 selection is performed. Using the LVL1 result as guidance, specialized Level2 algorithms request a sub–set of the event data from the ROSs to perform the event selection. In this way only a few per cent of the event data need to be transferred to the Level2 system thus considerably reducing the network bandwidth required. For events accepted by Level2, details are sent to the ROS (in the Level2 result) to be included in the event. The L2PU send the Level2 Decision back to the Level2 Supervisor, which forwards them to the Event Builder. The interface to the Level2 trigger and the event builder consists of multiple Gigabit network links.

Within the Event Builder the SFI (Sub Farm Input) assembles each accepted event into a single record, including the Level2 result. The built event is then passed to the Event Filter Processors (EFP) where offline algorithms are applied guided by information from the LVL1 and Level2 triggers to further refine the event selection. Events passing the EF are then passed to the SFO for permanent storage and offline analysis.

The Event Filter subfarms receive full events from the event building nodes. The communication protocol supports multiple SFIs per subfarm, so the size of the subfarms is flexible and can be adjusted as needed. The event is received into a shared memory buffer

by one process while the HLT software runs in separate processes. The software framework is flexible enough to accomodate a variety of Processing Tasks. These include not only trigger algorithms but also calibration or monitoring tasks. Accepted events are sent to a SFO (Sub Farm Output) node. It is responsible for forwarding the event to mass storage. Due to the modular design of the software the pieces can be arranged in various ways for installation or commissioning tasks. For example, the SFI and SFO functionality can be combined if no processing at the Event Filter level is required or the SFO functionality can be integrated into an EF task.

Events that have passed the EF will be written to mass storage. The design and support of the mass storage service will be centrally provided at CERN. However, in the first step of data storage, the SFO component will stream data directly to files on local disks. These will be large enough to accommodate typically a day of autonomous ATLAS data-taking in the event of failures in the network connecting ATLAS to the CERN mass storage system, or possible failures in the offline prompt reconstruction system.

4.3.2   The Level2 Trigger

The specific task of the Level2 trigger is to reduce the event rate from ~ 100 kHz further down to about 2 kHz: accessing the data from all detectors with full precision and full granularity. Unlike LVL1, Level2 performs asynchronous operations on events, with an average event decision latency of 10 ms.

The Level2 trigger is using regions of interest1 (RoIs) provided by the LVL1, which contain information about position (η, ϕ), p_T threshold range of the candidate and also components of E_T–miss vector and total scalar value; in this way only few percentages (up to 4%) of the data of an event are transferred from ROS to the Level2 processors thus requiring a decreased Level2 bandwidth. Each LVL1 RoI is first confirmed as a valid object.

At Level2 each RoI is first examined in the subdetector system from which it originated, i.e. in the muon or calorimeter system, to see if it is confirmed as a valid object. After the confirmation of the LVL1 RoI, additional features may be searched for in other detectors, such as the SCT/pixels and TRT. The information from all systems is then combined to take the Level2 global decision.

B–physics processing is different from standard RoI processing. It is based on a low p_T single muon trigger at LVL1. This muon may then be confirmed at Level2 in the muon spectrometer system. For events retained after this initial selection, a full track search must be performed to allow decisions based on semi-exclusive B–physics hypotheses. The present strategy is to search for tracks in the TRT with very low p_T thresholds. The resulting track candidates are used to define additional secondary RoIs that guide further track searches in the SCT/pixels. The reconstructed SCT/pixels tracks, giving information in three dimensions, allow for the calculation of invariant masses, or they may be extrapolated into the calorimeter or muon systems to confirm low pT lepton candidates, in conjunction with the transition–radiation signature from the TRT in the case of electrons.

The Level2 processors consists of the following components: RoI Builder (RoIB), the Level2 Supervisor (L2SV), the Level2 Processors (L2P), the ROS and the pROS. The RoIB assembles the fragments of information from the different parts of the LVL1 trigger and transmits the combined record to a L2SV. The L2SV selects a L2P for the event and

sends the LVL1 information to that processor and then waits for the Level2 Decision to be returned. The L2P runs the Level2 event selection software, requesting event data as required from the ROSs and returns the Level2 Decision to the L2SV. For events which are to be passed to the EF the L2P also sends a more detailed Level2 result to the pROS to be included in the event to be built.

Until the Level2 accepts or rejects an event (in ~ 10 ms), data are kept in ROBs. If the trigger decision is a reject, the data are discarded. In case of an accept, the data are moved to the Event Builder (EB), which combines event fragments from different ROBs to form a full event stored in a single memory location accessible by the EF.

4.3.3 The Event Filter Trigger

The task of the Event Filter (EF) is to make the final selection of physics events which will be written to mass storage for subsequent off–line analysis, and to reduce the trigger rates to as close to the interesting physics rates as possible. This should allow to reduce the output data rate from Level2 by an order of magnitude, giving an event rate of ~ 200 Hz if the full event data are to be recorded. Event summary information could be recorded at much higher rates, possibly for certain specific triggers (e.g. single–jet or multi–jet triggers for high–statistics QCD studies involving only the calorimeter information) but certainly not for the main-stream trigger items, which make up the bulk of the Level2 selected events. Here the access to all detector data at full granularity is possible and use of updated calibration and alignment data and non–homogenous magnetic field map is also possible.

The Event Filter online selection can be seeded by the Level2 result (or Level1 result) or it can make use of the full event information. Due to the availability of the full event, the EF is able to monitor the performance of lower trigger levels and detector performance.

The Event Filter contains two subsystems: the Event Handler and the EF Supervision. The Event Handler deals with the event selection, the monitoring and the detector alignment and calibration analysis, and the EF Supervision provides the configuration, control and operational monitoring of the Event Handler.

Because of a larger latency (order of seconds) a refined selection based on the full event information is possible using more complex offline–like algorithms, which can not be performed at Level2. Vertex reconstruction and track fitting, including bremsstrahlung recovery for electrons are examples of algorithms that could be executed at this level. Other examples are operations that require larger RoIs than those used at Level2, such as photon conversion searches (even if most conversions are identified in the size of a Level2 RoI) or calculations requiring the complete event data (as is the case for E_T–miss). The Level2 results can guide the EF processing chain in a mode that is similar to the guidance of Level2 by Level1 RoIs. The EF completes the classification of the events, establishes a catalogue of discovery–type events and stores the accepted events in the database. Events may be directed to separate output streams, for example if they are tagged as gold plated events for fast analysis or if they are needed for calibration or alignment purposes. The EF can also provide calibration data.

4.4　Event Selection Software

The tasks of the Event Selection Software (ESS) are 'event selection' and 'event clasification' [47, 40]. Abstract objects representing candidates such as electrons, jets, muons, and $J/\Psi \rightarrow e + e-$ are reconstructed from event data by using a particular set of HLT algorithms and applying appropriate cuts. An event is selected if the reconstructed objects satisfy at least one of the physics signatures given in the Trigger Menu. In both Level2 and the EF events are rejected if they do not pass any of the specified selection criteria, which are designed to meet the signal efficiency and rate reduction targets of the trigger. From a physics event selection point of view there is no precise boundary between Level2 and EF. Indeed, flexibility in setting the boundary is important to take advantage of the complementary features of these trigger stages.
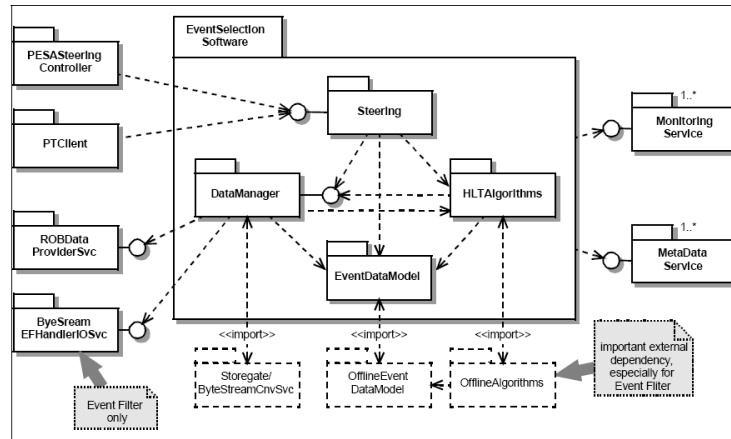
Figure 4.4: A package diagram of the Event Selection Software. Also shown are the dependencies of the subpackages.

The ESS comprises an infrastructure and the selection algorithms. In the HLT system the ESS will run in the online software environment and directly on the offline environment ATHENA to facilitate developement of algorithms and to allow performance studies for physics studies. Hence, for the the ESS needs to comply with the online requirements such as thread safety and for the latter comply with the control and services of the offline software architecture. In the offline the task of the ESS is to emulate the full online selection chain. The details of the prototype implementation of the physics electron/photon selection chain are given in Chapter 7.

The ESS is subdivided into four subpackages: the **Steering**, the **Event Data Model**, the **HLT algorithms** and the **Data Manager**. These are shown in Figure 4.4 with the most important external software dependencies.

4.4.1　The Event Data Model

The event data is structured following the Event Data Model (EDM) [47]. The EDM covers all data identities in the event and the relationships between them.

Raw Data coming from the ROS and the trigger systems are in byte stream format. This inlcudes the Level1 result, the Level2 and EF results, as well as ROB Data from the sub–detectors and from the Level1 system. For a given sub–detector several Raw Data formats might be used.

The *Raw Data Objects (RDOs)* are an object representation of the raw data from the different sub–detectors. In the trigger they are only used at the EF where they are created at the input to the reconstruction chain. In Level2, however, creating these objects poses too much overhead an thus in Level2 the the Raw Data is converted directly to Reconstructed Input Objects (RIOs).

4.4.2 The HLT Algorithms

The task of the HLT algorithms [48] is to analyse the Raw Data and to reconstruct parts of the event according to the guidence from Level1. The Level1 RoI approach implies a data–driven reconstruction . Any HLT algorithm can be executed several times per event, once per each RoI. The HLT algorithms are structured in two main parts:

- **Data Preparation** comprises algorithmic code to convert the Raw Data into objects that are used as input to reconstruction, including format changes and calibration corrections.

- **Feature Extraction** algorithms operate on abstract Features and Trigger Related data to refine the event information. Two type of algorithms are distinguished: reconstruction algorithms (produce new kinds of features like offline algorithms) and hypothesis algorithms (similar task to particle identification).

An overview of the HLT algorithms used for the electron/photon trigger selection is given in Chapter 6. The system performance of the data preparation and reconstruction of the HLT algorithms has been studied in Chapter 7.

4.4.3 The Steering

The Steering controls the HLT selection. It calls a certain subset of the available HLT algorithms in a certain sequence depending on the types of RoI received from the Level1 trigger [49].

The Level1 finds one or several RoI corresponding to an event. These can be a possible physics 'Signature'[1] (hypothesis) for which the ATLAS trigger accepts an event.

The Steering validates this hypothesis in a step–by–step process. Intermidiate signatures are produced as result of the algorithmic processing of a given step, and each intermidiate signature is examined in order to be able to reject the hypothesis at the earliest possible moment[2]. Each step is accompanied by one *Trigger Menu* (list of all intermiadiate signatures in its step for which an event can be accepted) and one *Sequence Table* (specifies which HLT algorithms are to be executed, given the seeds as input to the step.

---

[1]A signature is a combination of abstract physical objects like 'electrons', 'muons', this is of trigger menus.

[2]The primary motivating factor for the Steering is the need for fast and early rejection of uninteresting events in a flexible configurable manner and the need to pre–scale/ forced–accept some events
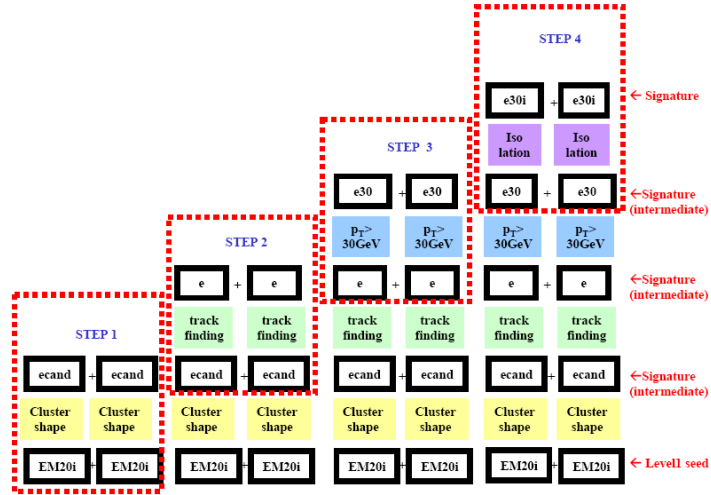
Figure 4.5: Example of the working principle of the ESS: The Level1 trigger finds two isolated electromagnetic clusters with $p_T > 20$ GeV each. This is a possible signature for the decay $Z \to e^+e^-$, for which the ATLAS trigger accpets the event if both electrons are isolated and have a minimum p_T of 30 GeV.

To guarantee early rejection, the Steering can reject an event after any step during the validation proceedure. The HLT processing is not organized vertically (carry out the full sequence of algorithms to arrive first to a reconstructed object for the first RoI and only then do the same for the second) but horizontally (carry out only the reconstruction forseen in step x for the first and second seed and use the output as seeds for the next step). Furthermore, in the same event the Steering calls the relevant algorithms once per seed, i.e. depending on the number of seeds possible several times.

4.4.4 The Raw Data Access

The Data Manager handles all event data during the trigger processing.

Raw Data from the ATLAS detector will be delivered in terms of a *ByteStream* of data consisting of hierarchically arranged fragments formatted in a sub–detector –dependant way. This ByteStream data must be converted into objects which can then be used by algorithms.

The HLT adopts a Raw Data Access scheme that aims to keep data transfers and CPU time to a minimum by only requesting and unpacking data as it is required; to encapsulate data access so that the algorithm does not have to deal with detail such as ByteStream or ROB granularity, and so the data source can be changed (Level2, EF, offline emulation) with no impact on the algorithm. A detailed description of this scheme can be found in [40].

Chapter 5

Physics Selection Strategy

This chapter provides an overview of the strategy for the online selection of events in ATLAS. The challenge faced at the LHC is to reduce the interaction rate of about 1 GHz at the design luminosity of $L = 1 \times 10^{34} cm^{-2} s^{-1}$ online by about seven orders of magnitude to an event rate of O(200 Hz) going to mass storage while selecting interesting physics events.

The discussions on this section concentrates on the initial luminosity regime ($L = 2 \times 10^{33} cm^{-2} s^{-1}$); the selection strategy for the high luminosity phase will crucially depend on observations and measurements during the first years of data taking.

5.1 Requirements

As described in Chapter 3.1 the ATLAS experiment primary goals are the understanding of the origin of electro–weak symmetry breaking, which might manifest itself in the observation of one or more Higgs bosons, and the search for new physics beyond the Standard Model. For the latter it will be of outmost importance to retain sensitivity to new processes which may not have been modelled. In addition, precision measurements of processes within and beyond the Standard Model will be carried out. The observation of new heavy objects with masses of O(1) TeV will involve very high–p_T signatures and should not pose a problem for the online selection. The challenge is the efficient and unbiased selection of lighter objects with masses of O(100) GeV. The selection criteria used in the assessment of the physics potential of ATLAS are mainly based on the selection of **high**–p_T objects, such as charged leptons, photons, jets (with or without b–tagging), and total transverse missing energy.

Event selection at LHC will have to cover a huge range in cross–section values for various processes, as shown in Figure 5.1. The interaction rate is dominated by the inelastic part of the total cross–section with a cross–section of about 70 mb. For design luminosity the inclusive production of b–quarks occurs with a cross–section of about 0.6 mb which corresponds to a rate of 6 MHz. The rate for inclusive W production, including the branching ratio for the leptonic decays to an electron or a muon is about 300 Hz and the rate for other rare signals, such as $H \rightarrow \gamma\gamma$ with 120 GeV invariant mass, will be much smaller. The online event–selection strategy has to ensure that such rare signals will be not
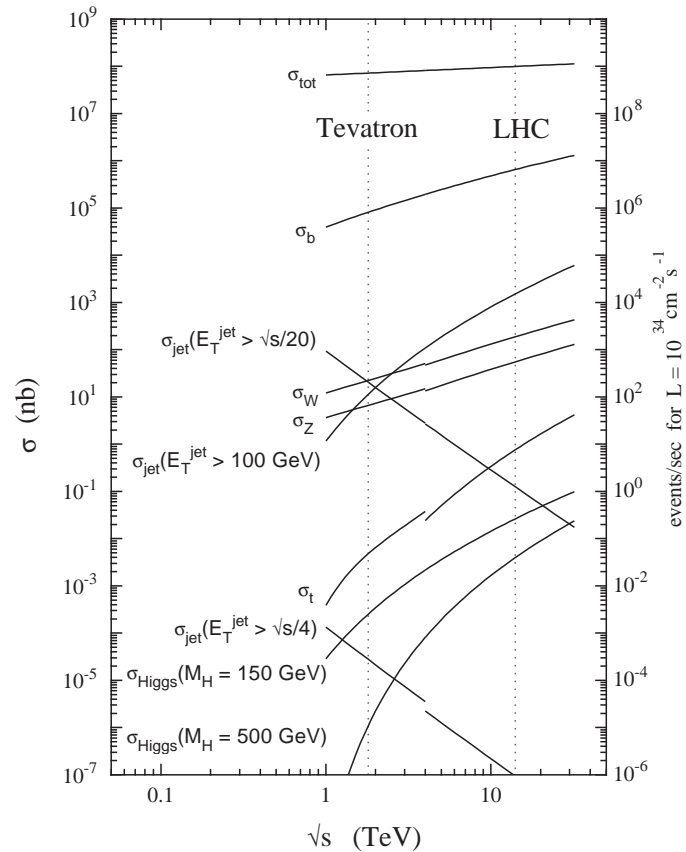
Figure 5.1: Cross–section and rates (for high luminosity) for various processes in proton–(anti)proton collisions, as a function of the centre–of–mass energy.

missed and efficiently covered, while at the same time providing the required reduction in the output rate of the HLT to mass storage to an acceptable value.

The online selection thus has to provide a very efficient and unbiased selection, maintaining the physics reach of the ATLAS detector. It should be extremely flexible in order to operate in the challenging environment of the LHC and provide a very robust, and, where possible redundant selection. It is highly desirable to reject fake events or background processes as early as possible to optimize the usage of available resources by the three trigger levels.

5.2   Selection Criteria

Presently to guarantee optimal acceptance to new physics the ATLAS online selection is based on inclusive criteria, i.e. having signatures mostly based on single– and di–object high–p_T triggers. These are objects such as charged leptons with a transverse momentum above O(10) GeV. This choice of thresholds has been made in such a way that

a good overlap with the reach of Tevatron[1] is guaranteed, and for covering a broad range of physics analysis from SM precision measurements up to searches for new physics (e.g. new light objects, e.g. Higgs bosons).

As described in chapter 4 the online selection in ATLAS is performed by a three level selection: Level1 and HLT (Level2 and EF). The selection at the HLT will in most cases be seeded by the information already obtained at Level1 (i.e. Regions–of–Interest, RoIs) and will exploit the complementary features of the Level2 trigger and EF selection. Although the Level2 and EF selection will be predominatly based on simple and inclusive signatures to allow for optimization at the analysis level, a more refined selection can be used in addition. These include the use of more elaborate algorithms and the application of more exclusive criteria, in order to enrich the available sample for certain physics processes. For example by requiring several different physics objects, e.g. the use of charged particles with transverse momenta of O(1) GeV for the selection of b-hadron decays. Another example is the use of a more elaborate algorithm for b–tagging of jets. Furthermore, it is highly desirable to select events with complementary criteria, in order to better control possible biases due to the online selection, for example due to E_T–thresholds.

The ATLAS trigger relies on the concept of physics 'objects' (muons, electrons, jets, etc.). Candidate objects are first identified and crudely reconstructed at Level1. Processing in the HLT progressively refines the reconstruction, rejecting fake objects and improving the precision on measured parameters such as E_T. The physics objects used in the HLT can be based on information from all sub–detectors of ATLAS, at full granularity. ATLAS, as a multi–purpose detector, will have charged–particle tracking in the Inner Detector covering the pseudorapidity region of $|\eta| < 2.5$ inside a solenoidal magnetic field of $2T$ and fine–grained EM calorimeter coverage for $|\eta| < 2.4$, especially in the electromagnetic calorimeter compartments, which extends up to $|\eta| < 3.2$. The hadronic calorimeter system covers the region up to $|\eta|$ of 4.9 for the measurement of missing transverse energy and jets. The coverage of the muon system extends up to $|\eta| = 2.4$ for the trigger chambers and up to $|\eta| = 2.7$ for the precision chambers (See Chapter 3).

The following overview briefly summarizes the most important physics objects foreseen for use in the HLT. More details on the concrete implementation of the selection algorithms and their expected performance for electrons and photons are given in Chapter 6.

- Electron (within $|\eta| < 2.5$): the selection criteria for electrons will include a detailed shower-shape analysis in the fine-grained electromagnetic compartments of the LAr calorimeters (within the range of $|\eta| < 2.4$), a search for high-pT tracks, and a match between the clusters and tracks in space. Further refinement is possible via the identification and correct treatment in case the electron has undergone Bremsstrahlung, use of the transition radiation tracker (TRT), and the application of isolation criteria.

- Photon (within $|\eta| < 2.5$): the selection of photons will also be based on a detailed calorimeter shower-shape analysis, including the requirement of isolation, recosntruction of converted photons and possibly on the use of a veto against charged tracks,

---

[1]Tevatron is a proton–antiproton collider currently running at center–of–mass energy of TeV

after it has been checked that the photon did not convert in the material of the Inner Detector into an $e + e-$ pair.

- Muon (within $|\eta| < 2.5$): the muon selection will in a first step make use of the external muon spectrometer to determine the muon momentum and charge. A refinement of this information will then be obtained by searching for tracks in the Inner Detector and matching and combining these candidates with the muon track segment. Isolation criteria may also be applied, using, for example, information from the calorimeters.

- Tau (within $|\eta| < 2.5$): the selection of taus in their hadronic decay modes will use calorimeter shower–shape analysis to identify narrow hadronic jets. These can be matched to one or more tracks found in the Inner Detector. As above, isolation criteria may also be applied, using, for example, information from the calorimeters.

- Jet (normally within $|\eta| < 3.2$): the jet selection will be based mostly on calorimeter information. A search can also be made for jets in the forward calorimeter, covering $3.2 < |\eta| < 4.9$.

- b-tagged jet (within $|\eta| < 2.5$): the selection will start from jets already selected. The associated tracks found in the Inner Detector are used to search, for example, for large values of the impact parameters or for the presence of secondary vertices, and/or for soft (i.e. low-pT) leptons.

- E_{Tmiss} (within $|\eta| < 4.9$): the definition of missing transverse energy will be based on the full calorimeter data, allowing for improvements via the inclusion of information from observed muons.

5.3 Trigger Menus

In this section, the trigger menu for running at an intial peak luminosity of $2 \times 10^{33} cm^{-2} s^{-1}$ is presented. There are four different types of trigger menus [50]:

- *inclusive physics triggers*: they form the backbone of the online selection and are chosen to ensure the ATLAS physics programme;

- *prescaled physics triggers*: they will extend the physics coverage for ATLAS, by having for example inclusive selections with lower thresholds to enlarge the kinematical reach and provide samples for understanding background processes and detector performance;

- *exclusive physics triggers*: they will also extend the physics coverage for ATLAS; and

- *dedicated calibration and monitor triggers*: not already contained in one of the above items, for improving the understanding of the performance of the ATLAS detector, based on physics events not needed otherwise for physics measurements. Furthermore, specific selections might be used to monitor the machine luminosity.

The derivation of the trigger menus and the threshold values starts from the physics analysis requirements, followed by an assesment of the rejection capabilities of the various selection stages, and taking into account estimates of the total HLT output bandwidth. The trigger menus will evolve continuously, benefeting from a better understanding of the ATLAS detector, and the physics experience gained when commissioning the experiment. Further progress in the understanding of the Standard Model and future discoveries prior to the start of the LHC might influence the contents of the trigger menus.

5.3.1 Inclusive Triggers

Table 5.1 gives an overview of the major selection signatures needed to guarantee the physics coverage for the initial running at a peak luminosity of $2 \times 10^{33} cm^{-2} s^{-1}$. The label of the trigger item is as follows, e.g. $2e15i$ read as '2' is the minimum number of objects required, the 'e' indicates the type of selection object, '15' gives the threshold in transverse energy (in units of GeV) and 'i' indicates an isolation requirement. The thresholds indicate the transverse–energy value above which the true object is efficiently selected. Table 5.1 also shows the HLT output rate corresponding to a Level1 trigger rate of 25 kHz and 95% efficiency for an initial peak luminosity of $2 \times 10^{33} cm^{-2} s^{-1}$. The rates shown were obtained using the selection algorithm steps at Level2 and in the EF for the various objects [40]. The single–/di–electron and single–/di–photon signatures currently account for one third of the HLT output rate. Only 5% of the HLT rate at peak luminosity is currently allocated to B–physics–related triggers (the low–p_T di–muon signature with additional mass cuts to select J/Ψ, Ψ' and rare B–meson decays). About 10% of the total rate is allocated for prescaled and other triggers.

Electron/Photon Trigger

A large part of the physics programme will rely heavily on the inclusive single– and di–lepton triggers, involving electrons and muons. Besides selecting events from Standard Model processes–such as top production, production of the W and Z bosons and the Higgs boson– they provide sensitivity to a large variety of new physics possibilities for example new heavy gauge bosons and (W',Z'), supersymmetric particles, large extra dimensions, and Higgs bosons in extentions of the Standard Model such as the MSSM. These triggers also select particle decays involving τ's where the τ decays leptonically.

In the present view of the ATLAS trigger menus [25], the inclusive electron and photon triggers are expected to contribute an important fraction of the total high–p_T trigger rate. After the selection in Level2 and the EF, the remaining rate will contain a significant contribution from signal events from Standard Model processes containing real isolated electrons or photons (b, $c \to eX$, $W \to e\nu$, $Z \to ee$, direct photon production, etc.). The identification of isolated electrons and photons is essential at the LHC, some important channels are:

- $H \to ZZ^* \to 4l$ is the most promising way to discover the Higgs boson if its mass is $m_H > 130$ GeV. A good rapidity coverage and an excellent energy resolution are

Table 5.1: ATLAS Trigger menu, showing the inclusive physics triggers, physics coverage and HLT output rate for low luminosity ($2 \times 10^{33} cm^{-2} s^{-1}$). The label of the trigger item is as follows, e.g. $2e15i$ read as '2' is the minimum number of objects required, the 'e' indicates the type of selection object, '15' gives the threshold in transverse energy (in units of GeV) and 'i' indicates an isolation requirement.

Selection Signature	Physics coverage	HLT
$e25i$	$W \to e\nu$, $Z \to ee$, t prod., $H \to WW^*/ZZ^*$, $W^{'}$, $Z^{'}$	40
$2e15i$	$Z \to ee$, $H \to WW^*/ZZ^*$	< 1
$\mu20i$	$W \to \mu\nu$, $Z \to \mu\mu$, t prod., $H \to WW^*/ZZ^*$, $W^{'}$, $Z^{'}$	40
$2\mu10$	$Z \to \mu\mu$, $H \to WW^*/ZZ^*$	10
$\gamma60i$	direct photon prod., $H \to \gamma\gamma$	25
$2\gamma20i$	$H \to \gamma\gamma$	2
$j400$	QCD, SUSY, new resonances	10
$3j165$	QCD, SUSY, new resonances	10
$4j110$	QCD, SUSY, new resonances	10
$j70 + xE70$	SUSY	20
$\tau35i + xE45$	$qqH(\tau\tau)$, $W \to \tau\nu$, $Z \to \tau\tau$ SUSY at large $tan\beta$	5
$2\mu6 + \mu^+\mu^-$+mass cuts	rare b–hadron decays $(B \to \mu\mu X)$ $B \to J/\Psi(\Psi^{'})X$	10
Others		20
Total		200 Hz

essential.

- $H \to WW, ZZ \to l\nu jj, ll\nu\nu, lljj$ channels are of interest for heavy Higgs searches, up to $m_H = 1$ TeV. A hermetic calorimeter with rapidity coverage up to 5 is essential in this case.

- $t\bar{t}$ production will be very large at LHC. A single high–p_T electron from the semileptonic decay of one top quark gives a good identification to look for rare decay modes of the other top quark. The electron 'tag' requires very good electron identification and QCD jet rejection.

- $W \to e\nu$ and $Z \to ee$, the latter is important for calorimeter calibration. Good electron identification and efficiency extraction are required.

- $H \to \gamma\gamma$ search in the low mass region demands good photon identification. A very good photon mass resolution from ECAL is needed to observe the narrow mass peak above the irreducible $\gamma\gamma$ background. A powerful photon identification is required to reject the large QCD–jet background.

5.3.2 Prescaled Triggers

There are additional contributions to the electron/photon trigger menu in the form of prescaled triggers. These triggers extend the physics coverage of the online selection by expanding the kinematic reach of various measurements towards smaller values, e.g. of the

transverse momentum of a process. For example, the selection signature of single electrons $(5-6$ thresholds between 7 and 25 GeV) for the measurement of the inclusive electron cross section. The values of the prescaled factor will evolve with time. In addition, these prescaled triggers together, with the prescaled minimum bias selection, will be crucial for determining trigger efficiencies from data. Thus, these triggers will be of particularly importance in the early phases of the data taking after the start–up of the LHC.

5.3.3   Exclusive Triggers

An example of a selection using a more exclusive criteria is the selection signature $e20i + xE25$ that requires a single electron and missing energy for the coverage of the $W \rightarrow e\nu$ process. For the first data taking, it will be essential that the full detector is read out to mass storage for all triggers in order to have the full spectrum of information available for offline studies. It is, however, envisaged that at a later stage some of the above prescaled triggers might no longer require recording of the full detector information, and thus more bandwidth could be made available for further exclusive selection criteria.

5.3.4   Calibration and Monitoring Triggers

The selection signatures presented so far will provide a huge sample of physics events which will be of extreme importance for the understanding and continous monitoring of the detector performance. A calibration electron trigger is for example one that uses $Z \rightarrow ee$ events to determine the absolute electron energy scale, to intercalibrate the electromagnetic parts of the calorimeter and for extraction of trigger efficiencies. Large inclusive samples of electrons will be used to understand the electromagnetic energy scale of the calorimeter, using the precise momentum measurements from the Inner Detector,and to understand the energy–momentum matching between the Inner Detector and Calorimeter.

A further example of monitor and calibration triggers is the random trigger on unpaired bunch crossing that will select bunch crossings, where only one of the two packets is actually filled, and can thus be used to monitor beam–related backgrounds. The monitor and calibration triggers provide examples of selections which do not always require the full detector information to be read out to mass storage. For some monitoring aspects it could be envisaged to record only the results of the processing of the event in the EF, and not to store the raw data.

Chapter 6

The Electron/Photon Trigger Selection

This chapter describes the inclusive electron/photon selection and the rejection capability against QCD–jets at the different trigger selection steps (Level1–Level2–Event Filter) using information from the e.m. LAr Calorimeter and Inner Detector systems.

The electron and photon triggers can be viewed as a series of selection steps of increasing complexity. At Level1, electrons and photons are selected using calorimeter information on a reduced granularity. After receving the Level1 electromagnetic (e.m.) trigger Region of Interest positions, the Level2 trigger performes a selection based on isolated e.m. clusters using the full calorimeter granularity within the RoI of size $\Delta\eta \times \Delta\phi = 0.4 \times 0.4$. To calculate the cluster E_T the most up–to–date available calibration data are used. Electrons and photons are selected based on the cluster E_T and shower–shape quantities that distinguish isolated e.m. objects from jets. A further, more refined calorimeter–based selection classifies the e.m. cluster as a candidate photon trigger object. In the next step, electrons are identified by associating the e.m. cluster with a track in the Inner Detector. In general, track candidates are found by independent searches in the TRT and SCT/Pixel ('Precision') detectors in the region identified by the Level1 RoI. For electron candidates, matching in position and momentum between the track and the cluster is required. Electron Candidates passing the Level2 selection criteria are retained to be examined by the Event Filter.

In the Event Filter electrons are selected with a strategy very similar to that for the Level2 using information from the calorimeters and the Inner Detector. The main differences with Level2 arise from the availability of calibration data and the possibility to use more sophisticated algorithms, such as bremstrahlung recovery and photon conversion recovery, with access to the detector data for the full event or seeded from the Level2 result.

6.1 Selection Strategy at the Level1

The primary function of the Level1 trigger is to reduce the incoming rate and select EM candidates that should be retained for further analysis because they contain a potentially interesting physics signature. For the electron/photon trigger the decision

is based on the coarse granularity information received from the calorimeters. At this level electrons and photons can not be distinguished. The Level1 trigger will provide the electromagnetic Region of Interest information to guide the Level2 trigger where full detector granularity is available and electrons and photons can be identified.

The task of the electron/photon trigger are: to identify electron and photon candidates using the calorimeter data, to classify these according to electromagnetic and hadronic E_T and isolation, to provide multiplicities of candidates passing each classification and to calculate the coordinates of candidates (η and ϕ) and their classification to the Level2 trigger. The main requirements for the Level1 are then [41]:

- good discrimination between isolated electromagnetic (e.m.) showers and QCD jets (the dominant high–E_T process and the main background for the e.m. cluster triger);

- high efficiency for electrons and photons of $p_T > 10\ GeV$, even in events wth complex topologies (multiple electrons/photons plus jets);

- accurate location of candidates within the calorimeters, to minimize the size of RoI the Level2 trigger needs to read out tower size driven by hrdware;

- unambigous classification of candidates found, and accurate count of their multiplicity.

6.1.1 The Level1 Calorimeter Simulation

An essential input to the HLT process is the seeding of the selection with the results from Level1. When making electon/photon perfomance studies for the HLT, a detailed emulation of the Level1 result is needed. This simulation allows to model the Level1 response in a 'realistic' way using the same procedures that will be implemented in custom hardware in the experiment.

The calorimeter trigger uses as input signals from trigger towers which are analog sums over calorimeter cells in the liquid–argon or scintillator–tile calorimeters. The trigger tower signals are digitized in the preprocessor electronics, which also performs digital signal processing to calculate transverse energy and bunch–crossing identification. The Cluster Processor searches for electron/photon candidates within 3200 trigger towers of granularity 0.1×0.1 in $\Delta\eta \times \Delta\phi$.

The electromagnetic cluster trigger uses data from the region $|\eta| < 2.5$, which is the limit of inner detector coverage and of high–granularity electromagnetic calorimetry. The algorithm is required to be efficient out to the ends of this region. A trigger–tower granularity of 0.1×0.1 was chosen as giving good compromise between performance (rejection of jet background) and the cost and complexity of the trigger.

In the electron/photon trigger a candidate object is defined by a local E_T maximum in a region of $2{\times}2$ trigger towers (electromagnetic plus hadronic), corresponding to a $0.2{\times}0.2$ region in $\eta-\phi$ space. Vetoes may be applied on the hadronic transverse energy in the region and/or on the transverse energies in the rings of towers surrounding the 2×2 region in the e.m. and hadronic calorimeter.

The electron/photon trigger algorithm is based on a window of 4×4 towers in the electromagnetic and hadronic calorimeters, and consists of four elements (figure 6.1):
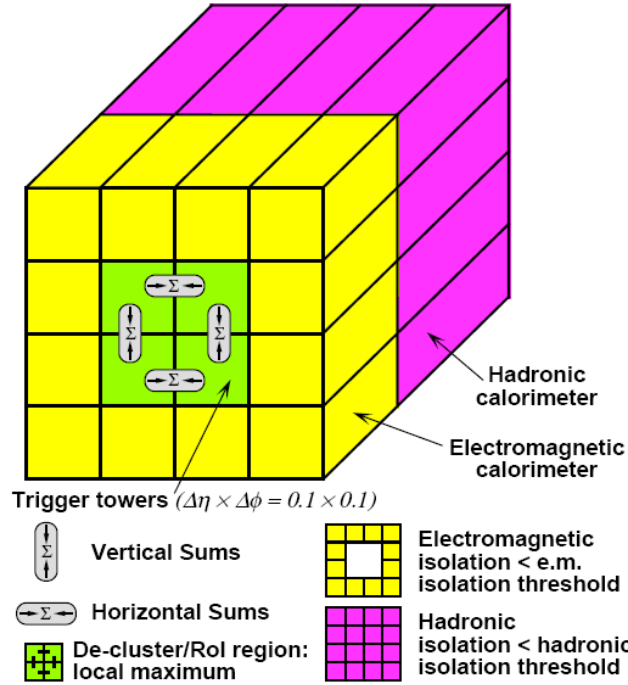
Figure 6.1: The Level1 electron/photon algorithm.

- a 2×2–tower electromagnetic cluster, used to identify RoIs.

- A 2–tower electromagnetic cluster, used to measure the E_T of electromagnetic showers. There are four such clusters within the RoI cluster, and the most energetic of these is used.

- A ring of 12 electromagnetic towers surrounding the clusters, which is used for isolation tests in the electromagnetic calorimeters.

- The 16 hadronic towers behind the electromagnetic clusters and isolation ring, which are used for isolation tests in the hadronic calorimeters.

The window slides in steps of one trigger tower in both the η and ϕ directions, so there is one window for each tower within the acceptance of the electron/photon trigger. The requirements for a trigger object to be found within the window are:

- the RoI must be a local E_T maximum;

- the most energetic of the four trigger clusters must pass the electromagnetic cluster threshold;

- the total E_T in the electromagnetic isolation region must be less than the e.m. isolation threshold;

- the total E_T in the hadronic isolation region must be less than the hadronic isolation threshold.

If all of these conditions are met, the window is considered to contain an electron/photon candidate (no distinction can be made here between electrons and photons). Eight set of trigger E_T thresholds are foreseen, and the candidate is classified according to which one it passes. The E_T cluster thresholds, e.m. isolation and hadronic thresholds used for the electron/photon studies presented in chapter 5 can be found in Appendix 1. The physics performance of the Level1 calorimeter trigger simulation for electrons and photons is addressed in Chapter 7.

6.2   Selection Strategy at the Level2

The Level2 algorithms are performed on RoI data, provided by the Level1 Trigger, for the calorimeter system and by the calorimeter system for the tracking system. An average processing time of ~ 10 ms per event is assumed for Level2 selection, and full detector information is available at this stage. Therefore, there are many requirements on the Level2 algorithms:

- high efficiency for the signal process larger than 95% with respect to Level1. This trigger efficiency depends on offline needs;

- uniform efficiency in η and constant or increasing efficiency with increasing E_T above threshold which is difficult to achieve in certain regions of the detector;

- reduction of the background rate which is achieved by improving object identification, sharper thresholds, good p_T resolution and

- robustness with respect to luminosity, noise, dead channels, alignment constants.

The Level2 electron/photon trigger is the starting point for the formation of the Level2 electron and photon triggers.

6.2.1   Calorimeter Electron/photon Selection

T2Calo ([51, 52, 53] is a clustering algorithm for electromagnetic e.m. showers, seeded by the LVL1 e.m. trigger RoI positions [41]. This algorithm can select isolated EM objects from jets using the cluster E_T and shower–shape quantities. The RIOs from which it starts are calibrated calorimeter cells (LAr or Tiles), as in the offline reconstruction.

The first step for the Level2 trigger algorithm is the refinement of the calorimeter information contained in the Level1 EM RoI. By using the full calorimeter granularity and a Level2–specific energy calibration, the Level1 decision is first confirmed and the quantities used in the Level2 decision are then calculated. Since photons and electrons deposit most of their energy in this layer, the cell with maximum energy is first searched for in the second sampling of the calorimeter . Then, a cluster is built around this position, typically in a window size of 3×7 cells.

The Level2 calorimeter algorithm T2Calo calculates the energies contained in 3×3, 3×7, and 7×7 cell clusters[1]. The total cluster transverse energy, E_T, is calculated by using the e.m. calorimeter layers and the pre–sampler contained in a window of 3×7 cells. Windows corresponding to approximately the same total $\eta \times \phi$ area in the second sampling are used in the other layers. The E_T is then corrected for lost energy due to the finite cell cluster size by using the expected lateral energy deposition for an e.m. shower.

After the energy correction, the η and ϕ energy–weighted cluster centre, (η_c, ϕ_c), is calculated using the second sampling of the calorimeter. No further position corrections are applied. The energy that leaks into the 1st sampling of the hadronic calorimeter, E_T^{had}, is then calculated in a window of size $\Delta\eta \times \Delta\phi = 0.02 \times 0.2$, centered on (η_c, ϕ_c).

Taking advantage of the fine granularity in η in the first sampling, the transverse shower shape is examined. All strips within a window of $\Delta\eta \times \Delta\phi = 0.125 \times 0.2$ at (η_c, ϕ_c) are associated to the e/γ cluster. The energies of the two strips in ϕ are summed into a single strip.

After the Level2–refined full–granularity information is available, trigger quantities sensitive to lateral and longitudinal shower shapes are built. In what follows, a description of each of the Level2 trigger quantities will be given:

Transverse energy in the e.m. calorimeter

Owing to the energy dependence of the QCD background, a cut on E_T provides the best rejection against jets for a given high–p_T signal process. The transverse energy E_T is calculated by using the e.m. calorimeter and the presampler over 3×7 cells in η and ϕ. The larger acceptance in ϕ reduces the low–energy tails due to photon conversion and electron bremsstrahlung.

Transverse energy in the hadronic calorimeter

Photons and electrons typically deposit very little of their energy in the hadronic calorimeter. Since jets, especially with high–p_T, can deposit a large fraction of their energy in the hadronic calorimeter, the hadronic energy can be used to tag those jets. The e.m. energy that leaks into the hadronic calorimeter increases with the incident e/γ energy and for low energy is not significant when compared with the contributions from noise and pile–up. In order to be efficient for e/γ clusters at high E_T, a hadronic isolation requirement must take this energy dependence into account.

Lateral shape in the second sampling

Photon and electron showers are on average much smaller laterally than showers initiated by jets. Most of the energy of e.m. showers (typically more than 70%) is deposited in the second sampling of the e.m. calorimeters. Therefore, this layer is relatively less affected by noise and pile–up effects. Thus in order to distinguish between e/γ clusters and

---

[1]a standard cell corresponds to the segmentation in the second sampling of the e.m. calorimeter $\Delta\eta\times\Delta\phi = 0.025 \times 0.025$
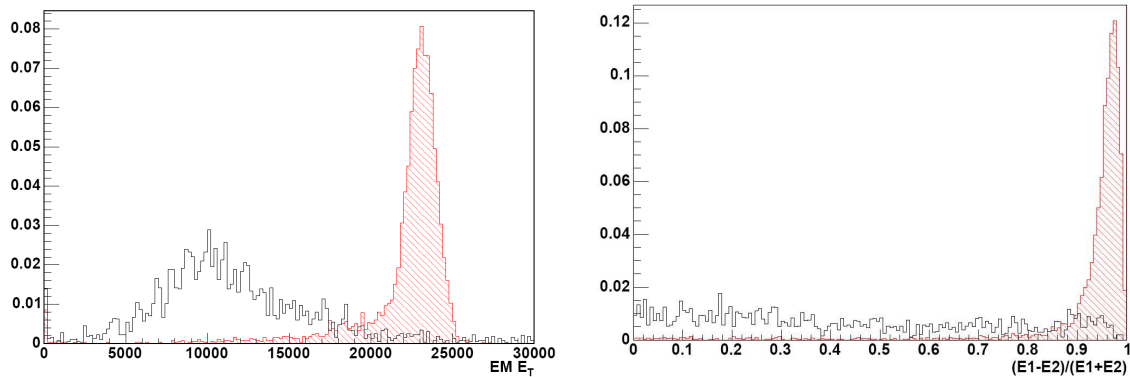
Figure 6.2: The left plot shows the E_T normalized distribution for jets with $p_T > 17$ GeV (empty histogram) and for single 25 GeV electrons (shaded histogram). The right plot shows the R_η^{shape} distribution for the same samples.

the jets the quantity R_η^{shape}:

$$R_\eta^{shape} = E_{3\times7}/E_{7\times7} \tag{6.1}$$

is calculated for the second calorimeter sampling. As for E_T, a wider window in $\Delta\phi$ allows for photon conversions and electron radiation so that most of the electron and photon energy is well–contained. This ratio is typically larger than 0.9 for electrons as shown in Figure 6.2.

Lateral shape in the first sampling

After applying the cuts in the hadronic calorimeter and the second sampling of the e.m. calorimeter, only jets with very little hadronic activity and narrow showers in the calorimeter remain. These 'electromagnetic' jets frequently consist of single or multiple π^0s or ηs decaying to two photons. In order to reject these jets the very fine granularity of the first sampling of the e.m. calorimeter can be exploited by looking for substructures within one shower in the η–direction and by analysing the shower shape. This analysis can only be done if enough energy is deposited in the first sampling. Thus, it is required that at least 0.5% of the total energy is deposited in the first sampling. In the case of jets one might find two maxima, e.g. from the two photons of a π^0 decay. Sometimes more than two maxima are found (e.g. in jets containing several π^0s). In order to reject this events, an algorithm which searches for secondary maxima is applied.

In this algorithm, the energy deposited in a window of $\Delta\eta \times \Delta\phi = 0.125 \times 0.2$ in the first calorimeter sampling is examined on a strip–by–strip basis. Two ϕ–bins are summed an the shower in the η–direction is scanned for a first and second local maximum. Here a local maximum is defined as a single strip with energy greater than its two adjacent strips. In case more than two maxima are found the second highest maximum is considered. After the first two maxima are found, the ratio R_η^{strip} is formed:

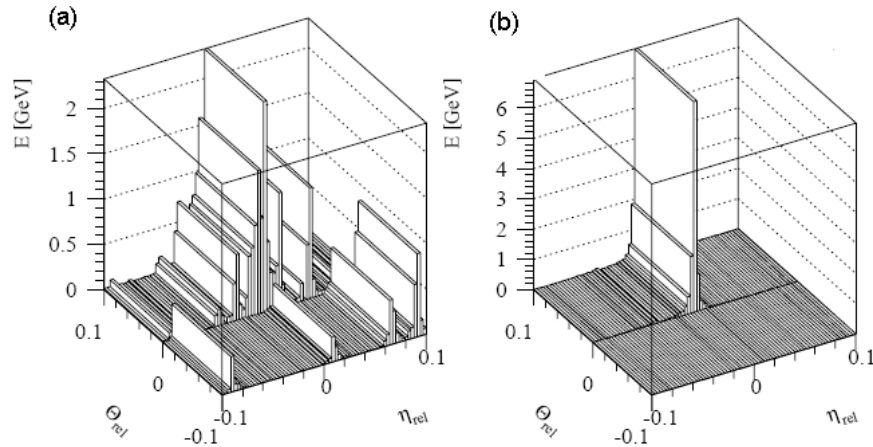$$R_\eta^{strip} = (E_{1st} - E_{2nd})/(E_{1st} + E_{2nd}) \tag{6.2}$$

Figure 6.3: Lateral shower distribution with respect to the centre of gravity of the shower in the first sampling of the e.m. calorimeter for (a) jet and (b) a photon. The distributions are for single events at low luminosity.

where E_{1st} refers to the energy of the highest–energy strip maximum and E_{2nd} is the energy of the second–highest–energy strip maximum. The ratio is found to be stable against fluctuations and no improvement is obtained if two or even three strips are considered to characterize the second maximum. Furthermore, since the strips are parallel to the ϕ–direction, this quantity is not affected by photon conversions or radiation of electrons.

6.2.2 Calorimeter Photon Selection

The trigger quantities used for photon identification are based on those used for the Level2 e/γ cluster trigger described in the previous section.

Also calculated are the following variables, which can be used to reject jets:

- shower width in the η direction (w_η). The shower width is calculated in 3×5 cells in the second sampling of the electromagnetic calorimeter, using the energy–weighted sum over all cells.;

- shower shape in η, R_η^{shape} (first sampling). Adding two ϕ–bins in the first sampling, the ratio of the difference between the energy deposited in ±3 and ±1 strips around the strip with the highest energy, to the energy deposited in ±1 strips is calculated ($(E_{7strips} - E_{3strips})/E_{3strips}$). This quantity measures the fraction of the energy outside the shower core. In ±1 strip around the maximum, typically more than 75% of the total energy deposited for photons in the first sampling is measured. Jets generally produce broader showers, and the fraction of energy outside of the shower core is larger than for photons;

The photon trigger is optimized such that converted and unconverted photons have a similar selection efficiency so that they are not rejected prematurely and can be 'treated' at the EF selection step [54].

6.2.3 Calorimeter–ID Electron Selection

Electron candidates are selected using calorimeter information, as described in the previous section, and Inner Detector information. A track search in the inner detector in the vicinity of the calorimeter cluster is performed to select electrons. Owing to differences in the information provided by the precision tracker (SCT and pixel detectors) and TRT, one approach to providing a simple, fast and robust trigger is to search for track segments separately in the TRT and SCT/pixel detectors in the region identified by the Level2 calorimeter RoI.

Inner Detector Selection

Typically, a histogramming method is used to identify sets of hits likely to form an initial set of track candidates for both precision and TRT detectors; the best track candidate is then selected on the basis of a fit to each set of selected hits. Details on the method can be found in [24]. The histogram is formed of the number of hits along possible track trajectories, thus the track candidate can be identified from peaks in the histogram. For all trajectories with a number of hits above some pre–defined threshold, a fit is performed. The TRT and precision trackers each return the parameters of a track candidate found by the Level1 calorimeter RoI.

IdScan [55, 56] is a track–reconstruction algorithm for LVL2. It takes as input Space Points found in the Pixel and SCT Detectors. A series of steps then process these inputs and output Tracks and the Space Points associated with them:

- The z–position of the primary interaction vertex is determined . The algorithm assigns the input hits to narrow ϕ–bins. For each bin it then extrapolates lines joining pairs of hits back to the beam line, entering in a histogram the z values obtained for all hit–pairs. After integrating over all ϕ-bins, it takes as the z–position of the primary vertex the histogram region with the most entries.

- Groups of hits compatible with tracks coming from the z position are found. All hits are put into a histogram binned in ϕ and η. The algorithm then finds clusters of hits within this histogram. Then, it creates a group of hits if such a cluster has hits in more than a given number of layers.

- The groups of hits found are split into tracks and noise hits are removed. Each triplet of hits forms a potential track for which p_T, ϕ_0, and the impact parameter d_0 are calculated. A track candidate is accepted if a group contains enough hits.

- Finally, track candidates are verified and track parameters are calculated using a fitting algorithm adapted from [57]. It returns a list of Space Points on the track, the track parameters, and an error matrix.

The first selection step is a p_T cut applied to the track candidates. This discriminates against the low–p_T tracks predominantly found in jet events. Since a significant proportion of electrons loose a large fraction of their energy via bremsstrahlung before entering the TRT, the efficiency for reconstructing a track in the TRT increases slowly with

decreasing value of the p_T cut. The different p_T cut values of the precision and TRT track for selecting electrons at high and low luminosity are given in Appendix 1. This is done to minimize efficiency with respect to Level1 of 95% for events passing the Level2 calorimeter selection.

After the calorimeter cuts, the contamination of the inclusive signal from charged hadrons is greatly reduced and the remaining background is dominted by photon conversions and multiple jets containing high p_T π^0 mesons [58]. An important variable is obtained when the Inner Detector idicates the presence of a good high p_T track pointing to the EM cluster indicating a good energy–momentum match for the reduction of the Level2 calorimeter trigger rate from this background, Figure 6.4. This is important as it allows a lower calorimeter E_T threshold to be used for the electron trigger than for the photon trigger. Even in the cases where a conversion has occured, a significant rejection is still obtained by requiring an inner detector track. The transition–radiation tracker can be used to further discriminate electrons from pions (see Chapter 9).
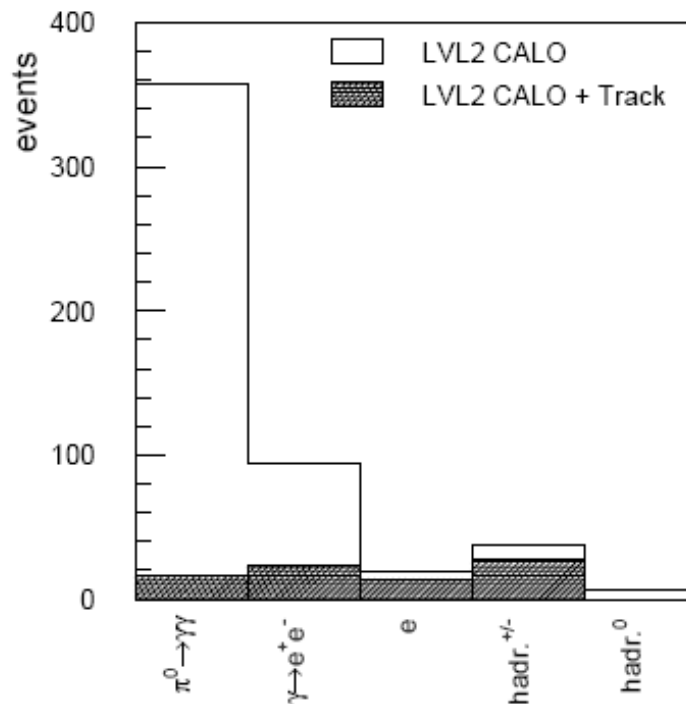

Figure 6.4: The highest p_T particle in events passing Level1 and Level2 calorimeter selections (open histogram) and for those events containing, in addition, tracks in the precision tracker matched to the calorimeter cluster (hatched) for jet events with $p_T > 25$ GeV at high luminosity.

ID/Calorimeter Matching

The jet rejection achived by the ID selection is significantly improved by insuring consistency between the EM calorimeter and ID information. In a significant fraction of jet events passing the common electron/photon selection the e.m. cluster is formed by the energy deposition from several low–p_T particles. Therefore it does not match well in position or energy with the track extrapolated from the ID. A cut on the azimuthal angle $|\Delta\phi|$ between the extrapolated track and the cluster position provides additional discrimination against jet events. The $\Delta\phi$ distribution is more narrow for electrons than for tracks in jet events [24]. This difference is more visible for the extrapolated precision tracks than in the TRT case.

An additional cut is performed on the difference in pseudorapidity between the cluster position and the position of the extrapolated precision track $|\Delta\eta|$. The discrimination power of this cut is better at low luminosity, while at high luminosity an important fraction of the track candidates contain one or more points incorrectly assigned to the track. The inclusion of these points affects the measurement of the track direction and in consequence the precision in η.

The momentum spectrum for tracks in jet events peaks toward low values. The cluster energy in these events can be much larger than the p_T of any single track. Therefore the ratio E_T/p_T provides additional discrimination against jet events.

6.3 Selection Strategy at the Event Filter

At the Event Filter the complete event data using full granularity of the Calorimeters and Inner Detector is available. At this selection step more precise calibration and alignment constants are available.

The baseline option for the selection at the Event Filter stage is to adopt algorithms from the ATLAS offline software suite. The present study uses the available ATLAS offline reconstruction software as a prototype of a future EF, as described in Chapter 4.3. Some improvements on the software suite allow for seeding of the EF by the Level2 result, including RoI position and features, in a similar way as Level2 is seeded by Level1 RoI [59], [60].

The selection at the EF (Calorimeter, Inner Detector and particle identification) follows the same scheme described for the Level2 selection, the looser timer constrains enable to employ more sophisticated reconstruction algorithms, being able to take care of bremsstrahlung recovery for electrons and conversion reconstruction for photons.

6.3.1 Calorimeter Electron/Photon Selection

Significant separation between electrons and jets can be achieved by the Level2 Calorimeter Trigger. Subsequently, the EF algorithms can refine the cuts made by the Level2 trigger as well as making additional ones. Only e.m. clusters with $E_T > 22$ (27) GeV at low (high) luminosity were considered for the study. These values correspond to the threshold cut of the single electron trigger item, which are chosen to be efficient for 25 (30) GeV electrons.

The variables used to distinguish high–E_T electrons and photons from jets are the same used for the Level2 calorimeter selection described in Chapter 6.2. A detailed description can be found in [61]. Since the variables are pseudo–rapidity dependent, they were optimized in several intervals to allow for varying granularities, lead thickness and material in front of the calorimeter. The quantities calculated using the first compartment can be used only in the regions $|\eta| < 1.37$ and $1.52 < |\eta| < 2.35$ since there are no strips in $1.4 < |\eta| < 1.5$ nor beyond $|\eta| = 2.4$. The cuts on the variables were tuned in such a way that a electron trigger efficiency of 98% is found for electrons after the Level1 and Level2 triggers. The cut values applied for the EF calorimeter selection can be found in Appendix 1.

LArClusterRec is the offline algorithm used as an EF calorimeter algorithm. The difference with the Level2 calorimeter algorithm is that the cluster energy is corrected for η and ϕ modulations of the calorimeter response and for leakage outside the cluster in a given window. In the region between the barrel and end–cap calorimeters, the cluster energy is in addition corrected for energy losses using the energy deposit in the crack scintillators. The η position in the first and second sampling is corrected for s–shapes, the ϕ position is corrected for an offset: both of them are geometry effects.

6.3.2   Inner Detector Electron Selection

After the calorimeter cuts, the contamination of the inclusive signal from charged hadrons is greatly reduced. The remaining background is dominated by photon conversions and low multiplicity jets containing high–p_T π^0 mesons. This background is further reduced by requiring the presence of a good ID track pointing to the e.m. cluster and with a good energy–momentum match like in the Level2 ID selection strategy.

xKalman++ and IpatRec are offline algorithms for global pattern recognition and Track fitting in the Inner Detector that are used as the prototype for EF tracking algorithms. In this prototype the EF algorithms receive as input the complete event. A more detailed description of these algorithms is available in [62, 63, 64].

All tracks above a certain transverse momentum are reconstructed in a given region (called cone or road) parametrized by $\Delta\eta$, $\Delta\phi$ around the selected e.m. cluster to find tracks with pattern recognition algorithms. Whenever possible, a bremsstrahlung recovery procedure which combine in 3–D the standard track parameters, coming from a fit allowing for multiple scattering, and dE/dx, with the position of the calorimeter cluster centroid, is used [25]. In case the bremsstrahlung recovery procedure is not available (especially for charged pions where the matching between cluster and track is not good), the simple track fit is taken as a measure of the p_T of the track. The reconstructed track with the highest p_T in the cone is required to satisfy the extended ID track quality cuts. The selection criteria are: number of precision SCT hits, number of pixel hits, number of B–layer hits, transverse impact parameter, and number of TRT straw hits. The value for these cuts are shown in Table1 of Appendix 1. The cuts on the number of pixel hits and B–layer are very effective to reject electrons from photon conversions, reducing them by a factor of 5 at low luminosity.

6.3.3   ID/Calorimeter Matching Electron Selection

The jet rejection achieved by the ID selection is significantly improved by insuring consistency between the EM calorimeter and ID information. Firstly, the angular matching between the track and the EM cluster was checked, allowing for the track curvature and the vertex position:

- $\Delta\eta = \eta_{CALO}^{strips} - \eta_{TRACK}$; η_{CALO}^{strips} is computed in the strips of the calorimeter with a correction for the spread of the primary vertex in z, and η_{TRACK} is the extrapolation of the track pseudorapidity into the first sampling of the EM calorimeter.

- $\Delta\phi = \phi_{CALO}^{2nd} - \phi_{TRACK}$; ϕ_{CALO}^{2nd} is computed in the second sampling of the EM calorimeter and ϕ_{TRACK} is the extrapolated track into the second sampling of the EM calorimeter.

In both distributions of the absolute value of this variables the electrons clearly peak at zero while charged hadrons and conversions show tails at higher values because of incorrect position matching [58]

Subsequently, the energies of the EM calorimeter cluster and the Inner Detector reconstructed track were compared, E^{CALO}/p_T^{TRACK}. The tail at low values of E/p arises from π^0 decays in which one of the photons is converted while the second photon is included in the EM cluster causing the track fit (incorporating the calorimeter bremsstrahlung recovery procedure) to overestimate the momentum.

6.3.4   Use of TRT for Electron Selection

The jets which survived the selection procedure described so far consist mainly of isolated electrons. The fraction of e–like jets arising from the mis–identification of charged hadron background was 30% (40%) at low (high) luminosity [58]. The fraction of e–like jets coming from photon conversions was greatly reduced by the previous cuts.

The emission of transition radiation (TR) photons in the straw tubes of the TRT is a threshold effect proportional to the inverse of the mass of the passing particle. The seperation between electrons and pions is effective for $E < 100\ GeV$ and vanishes at higher energies because the rate of TR photons emitted by pions and electrons are comparable. A further reduction of the charged hadron contamination is thus obtained by rejecting tracks having a low fraction of TRT straw hits with a high–threshold TR hits. The cut applied are arranged in p_T bins and η bins, see Appendix A. They are tuned to obtain 90% electron efficiency at both low and high luminosity [25]. The selection strategy used to seperate electrons from pions using the TRT detector is presented in Chapter 9.4.

Chapter 7

Electron/Photon Trigger Studies

The physics performance (signal efficiency against background rejection) and system performance (execution time of the algorithm) for the inclusive selection of electrons and photons by the HLT are studied in this Chapter. The study includes pile–up effects addressing both the low and design luminosity scenarios. Although the emphasis on this study will be on the contribution of the Level2 and Event Filter trigger selection to the reduction in rate, the final overall optimization of the selection procedure also includes the Level1 selection.

The electron/photon trigger physics performance studies presented have been all performed using a realistic simulation of the ATLAS detector with pile-up and electromagnetic noise in the calorimeter. This is the first electron physics performance study performed with full reconstruction, access to raw data [1], pile–up (start–up and the design luminosity) and almost 'final' ATLAS reconstruction software.

7.1 Detector Layout

In this study the simulated data sets have a detector layout referred to as Data Challenge 1 [65]. A more up to date detector layout is used compared to earlier studies [27, 66]. The inner detector now contains more material compared with the older layout especially due to the support of the first pixel layer, which will not be present at start–up due to deferrals. Specially in the end–cap bremsstrahlung is becoming more pronounced, because electrons have to pass more material before arriving to the calorimeters. The material increase near the beampipe is potentially more harmful because hard bremsstrahlung occuring in this region cannot be recovered. In the simulations of the ATLAS detector used for these studies the magnetic field decreases from $B \approx 2T$ at $\eta \approx 0$ to $B \approx 1T$ at the end of the solenoid down to $B \approx 0.4T$ at $\eta \approx 2.5$. In the calorimeters the end–cap is shifted by $4\ cm$ to leave more space to bring out cables in the crack between barrel and end–cap cryostat. This will mainly affect the shower shape variables which tend to be slightly broader than previous studies.

---

[1]raw data means as it comes out of the detector electronics

Table 7.1: Data samples at different p_T used for the e/γ physics performance study.

type	low luminosity	high luminosity
electron	25 GeV	30 GeV
γ	20 GeV	
jet	17 GeV	25 GeV
signal	$W \rightarrow e\nu$	

7.2   DataSets

The performance of the HLT electron selection has been evaluated on MonteCarlo simulated samples, in terms of the efficiency for the real electron signals and of the expected output rates, directly related to the rejection power for fake candidates.

To study electron trigger efficiencies fully simulated single electrons with $p_T = 15$, 25 (30) GeV have been used at low (design) luminosity. To evaluate the trigger rates fully simulated QCD dijet events have been used. At the parton level each jet was required to have a transvere momentum p_T of at least 11, 17 and (25) GeV at low (design) luminosity (see Table 7.1). The events were generated with Pythia 6.203 [67]. Initial as well as final state radiation was simulated. In addition to QCD dijet events, other physics processes such as prompt photon events, intermediate W and Z production, and top production were generated according to their cross sections. Events which would not pass the Level1 trigger were inmediatly rejected before being processed by GEANT [68] using a particle level filter applied at generator level. Only 8.33% (10.2%) of all generated events have been accepted by the particle level filter.

Pile-up was added to these datasets for the low luminosity ($L = 2 \times 10^{33} cm^{-2} s^{-1}$) and design luminosity ($L = 1 \times 10^{34} cm^{-2} s^{-1}$) scenarios. The number of minimum bias events that are added per bunch crossing in the calorimeters and the inner detector are 4.6 (23) for low (design) luminosity. In the calorimeters the readout time is around 500 ns so the correct shaping functions have to be used (see Appendix 2). In the pixel detectors and the SCT the response to charged particles is fast enough so that only minimum–bias events from bunch crossing zero are seen. There is small contamination arising from minimum–bias events from previous or following bunches. In the TRT the maximum drift time is around 40 ns, which is longer than the time between two bunches. Thus, hits from 'out of time' events also have to be considered.

7.3   Software

Whenever possible, realistic raw data [2] formats have been used as a starting point for the HLT algorithm selection, using a very detailed simulation of the raw data as they

---

[2]Raw data from the ATLAS detector will be delivered in terms of a ByteStream. Data is hierarchically arranged in fragments formatted in a sub–detector–dependent way
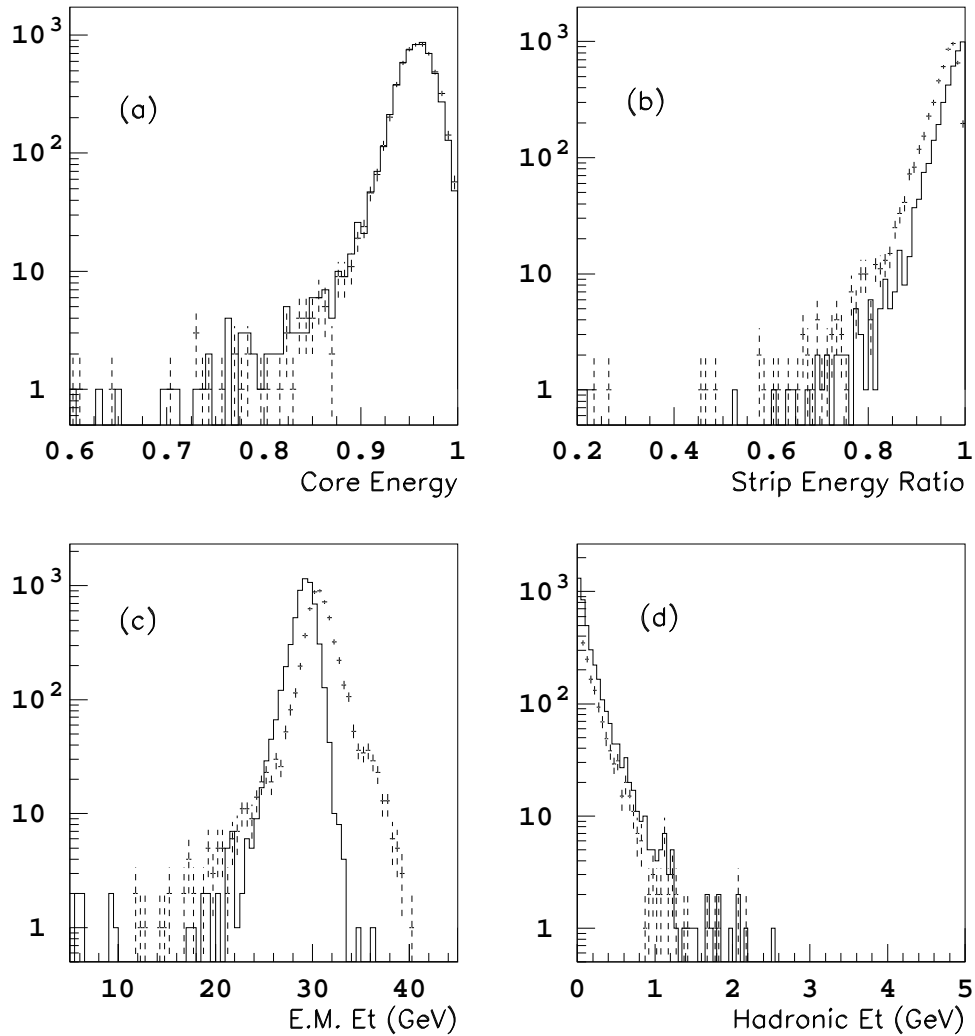
Figure 7.1: Comparison of the different variables used for electron jet rejection at Level2 for T2Calo (solid lines) and offline (dashed lines) for electrons $p_T = 30\ GeV$. (a) core energy sampling 2, (b) strip energy ratio of sampling 1, (c) e.m. p_T and (d) leakage into the hadronic calorimeter. The crosses indicate the results obtained from T2Calo, the solid line the ones from the offline cluster reconstruction.

will appear when accessed from the Read Out System (see Chapter 4.4). This is deemed to be extremely important since, data unpacking and data preparation for the algorithm processing represent a sizable fraction of the computing time, even when using optimized data–preparation software. Currently, quite some work is ongoing to reduce the latency of this step.

Steering Control (as described in Chapter 4) has also been employed, highlighting the flexible boundary between Level2 and EF. Selection schemes are then derived, which contain the signatures used to decide wether or not to reject events.

Signal and background generated samples were fully reconstructed in the ATHENA
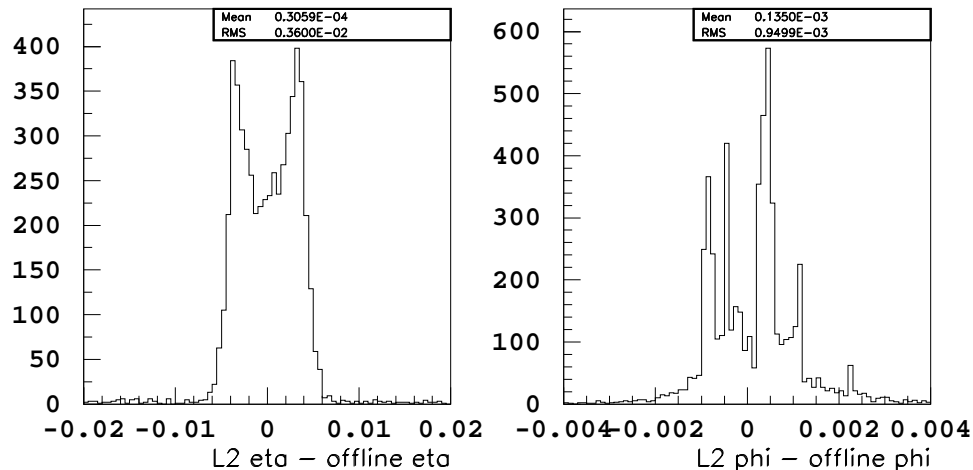
Figure 7.2: Difference in (a) η and (b) ϕ between the reconstructed cluster values at Level2 and offline for 30 GeV electrons at high luminosity.

framework written in $C++$ [42] by trigger and offline algorithms[69, 48, 70] described in Chapter 6. The present study uses the currently available ATLAS offline reconstruction software as a prototype of the future EF algorithms as described in chapter 6.3.

7.4 Physics Validation of the Level2

At Level2, two algorithms were used for electron/photon physics performance studies that made use of the calorimeter and SCT/pixel information available online: T2Calo and IdScan. A detailed description of the selection performed by these two Level2 algorithms has been given in Chapter 6.2.

The T2Calo algorithm running within the HLTSSW, has been validated with the offline e.m. cluster reconstruction. In order to study possible differences, the quantites calculated by T2Calo have been compared with those obtained from the online in an event–by–event basis.

Using 30 GeV electrons, Figure 7.1 compares reconstructed e.m. cluster quantities at Level2 and the offline for the four variables used in the rejection at Level2: core energy of sampling 2 (R_η^{shape} 6.1), strip energy ratio of sampling 1 (R_η^{strips} 6.2), total e.m. E_T, and hadronic energy. The agreement is good except for the total e.m. E_T, for which the online reconstruction underestimates the energy. This is due to the fact that the online currently does not apply calibration constants and cluster corrections.

Figure 7.2 presents the difference between the η and ϕ values reconstructed with T2Calo and those obtained with CaloRec. The difference can be explained by the cluster corrections applied in the offline for η and ϕ. In the offline s–shape corrections are applied for the measured η values. The ϕ direction is corrected for an offset [27].

IdScan is a Level2 track reconstruction algorithm. This tracking algorithm is implemented in the Online Athena environment and the Online HLTSSW environment [48]. The Level2 tracking algorithm recieves SCT/pixel online space points while the offline

pattern recognition algorithm xkalman starts reconstruction from offline space points. Validation of the Offline and Online versions of IdScan has been carried out with respect to the xKalman full reconstruction package. Only events where xKalman is able to reconstruct tracks satisfying the following criteria are considered: $\Delta r = sqrt(\eta - \eta_{true})^2 + (\phi - \phi_{true})^2 <$ 0.1, $Z_0 - Z_{0true} < 0.2$, and $|(p_T - p_{Ttrue})/p_{Ttrue}| < 0.5$. Plots for the p_T, η, ϕ, Z_0 and d_0 distributions for high luminosity are presented in Figure 7.3. These highlight problems with the η and Z_0 resolutions at high luminosity for the online version. These issue has been solved in recent productions.

7.5   Level1 Electron Physics Performance

The performance of the electron and photon trigger menus has been estimated for electrons and photons, and for some standard physics channels e.g. $W \rightarrow e\nu$. The physics performance is characterized in terms of efficiency for the signal channel, and the rate expected for the selection. Here the single–electron and double–electron trigger are considered for both low and high luminosity scenarios, the single photon and double–photon triggers are considered only for low luminosity.

The physics performance of the Level1 calorimeter trigger simulation has been validated [71]. The rate of the Level1 electron/photon trigger is dominated by misidentified jets. Figure 7.4 shows the estimated trigger rate for the single electron/photon trigger as a function of transverse–momentum threshold for a luminosity of $2 \times 10^{33} cm^{-2}s^{-1}$ (low) and $1 \times 10^{34} cm^{-2}s^{-1}$ (high). The upper and lower bands give the rate before and after applying the isolation requirements. The E_T–threshold scale in the plot is defined so that the efficiency for selecting genuine electrons with transverse energy equal to the quoted value is 95%.

The results obtained using the new Level1 software have been compared against previous studies [41] altough details of the trigger tower simulation and detector model were different. In general there is fair agreement between the old and new results. For example, the estimated rates for the single electron/photon trigger for low luminosity agree with the earlier simulations to within 20%. The rates in the new results are underestimated due to biases in the particle level filtering.

7.6   HLT Electron Physics Performance

7.6.1   Low Luminosity

The currently achieved HLT performance for the single isolated–electron $e25i$ trigger is summarized in Table 7.3 as a function of the main steps in the Level2–EF trigger chain for the $2 \times 10^{33} cm^{-2}s^{-1}$ luminosity scenario. The trigger steps have been factorized by detector in order to show the rejection contributed by each trigger step. It should be noted that there are strong correlations between the different selection criteria. Efficiencies are given for single electrons of $p_T = 25\ GeV$ already selected by Level1, averaged over the full pseudorapidity range $|\eta| < 2.5$, excluding the barrel/EC region $1.37 > |\eta| > 1.52$. As

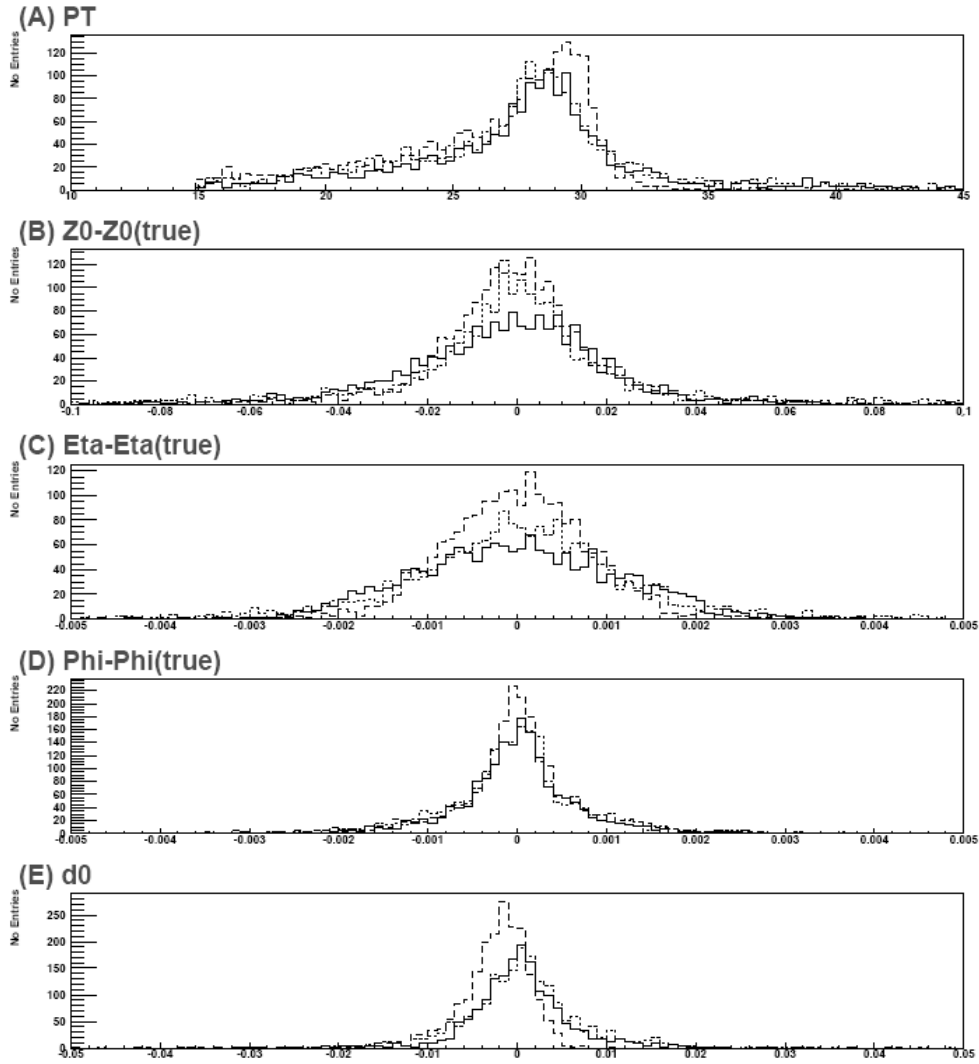Figure 7.3: Comparison of different track reconstruction parameters between IdScan and xKalman for $p_T = 20\ GeV$ single electrons at high luminosity. In the plots the distribution for the online implementation of IdScan (solid lines), offline implementation of IdScan (dotted lines) and offline xKalman (dashed lines) are shown. From top to bottom plots for the p_T, η, ϕ, Z_0 and d_0 distributions are shown.

quoted before the efficiency of the Level1 selection is 95%. The rates are normalized to a Level1 rate for e.m. clusters of 8 kHz. The quoted errors are statistical, there are very large systematic uncertainties on the rate estimates, e.g. from cross–section uncertainties.

For the single electron $e25i$ trigger an overall efficiency of 76% for a final rate of 40 Hz is achieved after all the HLT selection steps, as shown in Table 7.3. This corresponds to a trigger efficiency of 79% with respect to the Level1 trigger. The overall reduction in
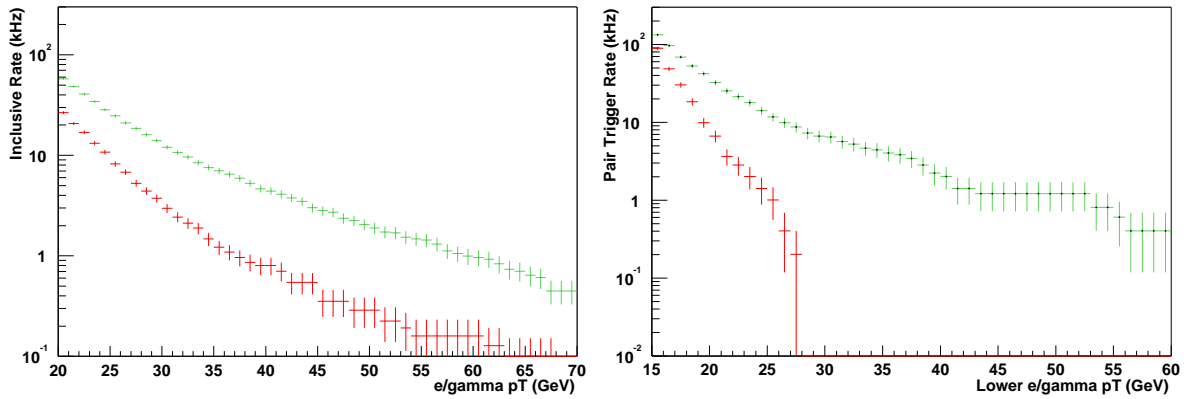
Figure 7.4: Inclusive level1 electron trigger rates vs. E_T threshold without (upper band) and with (lower band) isolation requirements at low (left) and high (right) luminosity.

Table 7.2: Final rate composition for the single electron trigger $e25i$ at low luminosity and the $e30i$ at high luminosity.

Rate Compostion	$e25i$	$e30i$
b and c decays	44%	20%
converted γs	21%	18%
$W \to e\nu$	19%	32%
$Z \to ee$	1%	1%
others	15%	29%

rate achieved by Level2 calorimeter is 10 for a loss of efficiency of 3% with respect to Level1. The additional rate reduction provided by the Event Filter is a factor of about forty for a further efficiency loss of 17%. This shows the power of the two–tier HLT selection. The final rate composition comes mainly from real electrons (electrons from b and c decays and conversions) and only 15% of the rate comes from fake clusters. The rate compostion for thsi trigger menu is shown in Table 7.2.

As noted in Chapter 6 the Level2 Inner Detector selection was excluded from the physics performance studies of the electron trigger. Technical problems in the z–finder of the Level2 tracking algorithms IdScan was discovered in the production used for these physics performance studies. This meant idScan did not find tracks that would have been accepted by the EF inner detector pattern recognition algorithm xKalman, thus rejecting events prematurely. In the case were online space–points are used the Level2 tracking efficiency loss is 4% compared to offline space–points at low luminosity. Therefore, for further electron trigger studies the Level2 tracking trigger step will be excluded from the selection. This problem of Level2 tracking efficiency loss has been solved in recent productions and the physics performance for single electrons has been re–evaluated.

Compared with previous studies [72], the rate reduction at Level2 was found to

Table 7.3: Trigger efficiencies and rates for the single electron trigger $e25i$ and double electron trigger $2e15i$ at low luminosity. The trigger selection at each level is factorized by detector: calorimeter, inner detector, combined calorimeter–inner detector.

Trigger Selection	$e25i$		$2e15i$	
	Trigger Efficiency (%)	Rates	Trigger Efficiency (%)	Rates
L1	95.5 ± 0.2	8.6 kHz	94.4 ± 0.5	3.5 kHz
L2Calo	92.9 ± 0.3	1.9 kHz	82.6 ± 0.9	159 Hz
EFCalo	90.0 ± 0.4	1.1 kHz	81.2 ± 1.0	110 Hz
EFID	81.9 ± 0.2	108 Hz	69.2 ± 1.0	5.6 Hz
EFIDCalo	76.2 ± 0.4	46 Hz	57.3 ± 1.5	1.9 Hz

be almost identical for the same electron p_T. This is a useful cross check and a significant achievement given the completely different selection–software architectures (C++/fortran). At the Event Filter the rate reduction is currently 4.6, compared to 5.2 as reported in [72].

If the rate for a trigger item from any level in the selection is too high, one can reduce it either by raising the E_T threshold of the item or by tightening the selection criteria. However, this might result in a loss of efficiency in interesting physics events, partly recoverable by adding more exclusive triggers for the channels of interest. To ensure the physics programme at the LHC and the correct set–up of the trigger menus, cross–checks have been performed using important physics channels such as $Z \rightarrow ee$, and $W \rightarrow e\mu$. As further validation of the above results, the electron efficiencies have also been extracted using fully simulated $W \rightarrow e\nu$ signal events. With respect to Level1, efficiencies wrt Level1 of $(90.6 \pm 0.8)\%$ after Level2 and $(83.2 \pm 1.0)\%$ after EF have been obtained [40]. The simulation included pile–up for a luminosity of $2 \times 10^{33} cm^{-2} s^{-1}$ and the W events were required to have the electron with $p_T > 25~GeV$ at the generator level. These efficiencies are slighlty higher than the ones given in Table 7.3 for single electrons of $p_T = 25~GeV$. This is expected since the efficiency is better for electrons with p_T well above the threshold value than for those at the threshold value. Preliminary studies of the full offline electron/jet separation analysis, which uses even more powerful selections than the ones that can be exploited at the EF, also confirm the rates and efficiencies found here.

The currently achieved HLT performance for the double isolated electron $2e15i$ trigger is summarized in Table 7.3 as a function of the main steps in the Level2–EF trigger chain for the $2 \times 10^{33} cm^{-2} s^{-1}$ luminosity scenario. The physics performance of the double electron trigger is evaluated for single electrons with $p_T = 15$ GeV. Therefore the efficiency of the $2e15i$ trigger is calculated as the efficiency product of the single $e15i$ trigger. For the double electron trigger an efficiency of 64% for a final rate of ~ 2 Hz is achieved with respect to Level1 after all the HLT selection steps. Compared to previous studies [72], the rate obtained after at Level2–EF was found to be identical although higher–statistics of the dijet samples are needed for further comparison.

It should be noted that the HLT output rate estimates are the result of simulation,

which start with a physics event generator (mostly PYTHIA) and then involve a detailed GEANT–based simulation of the ATLAS detector response. The rate estimates are thus subject to several sources of uncertainties: knowledge of cross–sections (e.g. the multi–jet production has an uncertainty more than a factor of two), realistic detector behaviour and performance, background conditions, resources constraints and software performance.

Based on previous experience, a reasonable target at the EF is to accept electrons with an overall efficiency of about 80% with respect to Level1 in order not to cut too hard on the physics. From present understanding, one can conclude that, with an improved tuning of the different selection steps and for at least 80% electron efficiency, a final rate of 40 Hz at low luminosity (as obtained in previous studies [73, 74]) is still valid using the new selection algorithms with updated detector geometry, and allowing for the changes at the generator level. Further Work is needed to optimize and cross–check the current selection cuts. For example, the cuts can be tuned in a more optimized way as a function of pseudorapidity, and additional criteria such as isolation in the Inner Detector around the electron track, isolation around the the e.m. cluster can be studied.

7.6.2 High Luminosity

The analysis of the performance of the single electron trigger $e30i$ at high luminosity is presented in Table 7.4. A trigger efficiency of 73% for a rate of 213 Hz is obtained after the Level1 and EventFilter trigger selection steps. The final rate of ~ 200 Hz is comparable to the HLT total output rate. Therefore, further work is needed to optimize the signal efficiency and rate reduction, including also the Level2 trigger. The overall trigger efficiency for the double electron trigger $2e20i$ after the EF selection is 61.4%; the associated rates were not estimated due to the unavailability of the corresponding dijet sample.
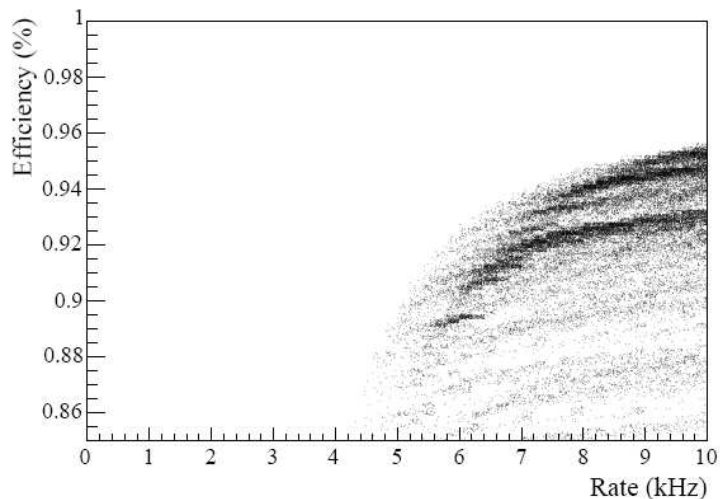

Figure 7.5: Rate–efficiency curve for the Level2 calorimeter selection at low luminosity. The curve shows the lowest rate for a given efficiency after the optimization procedure.

Table 7.4: Trigger efficiencies and rates for the single electron trigger $e30i$ and double electron trigger $2e20i$ at high luminosity. The trigger selection at each level is factorized by detector: calorimeter, inner detector, combined calorimeter–inner detector.

	$e30i$		$2e20i$	
Trigger Selection	Trigger Efficiency (%)	Rates	Trigger Efficiency (%)	Rates
L1	95.5 ± 0.2	23.9 kHz	93.5 ± 0.5	
EFCalo	92.8 ± 0.4	4.2 kHz	87.2 ± 1.0	
EFID	82.1 ± 0.2	695 Hz	71.6 ± 1.0	
EFIDCalo	73.8 ± 0.4	219 Hz	61.4 ± 1.5	

The final rate composition comes mainly from real electrons (electrons from b and c decays and conversions) and only 29% of the rate comes from fake clusters. The rate compostion for this trigger menu is shown in Table 7.2. The final rate of ~ 200 Hz is very high–it is the total HLT rate output possible for all inclusive signatures– and 70% of the clusters come from "real" electrons.

7.6.3 Optimization of Level2 Selection

The strategy followed in optimizing the Level2 electron/photon trigger selections is to obtain high efficiency while keeping the cuts simple. This allows further refinement in the electron and photon trigger stage (e.g. η–dependent cuts) while maintaining a common set of cuts for the e.m. cluster trigger. Also for this reason the cuts are chosen such that unconverted and converted photons are affected the same way.

The optimal cut values for the four Level2 calorimeter trigger quantities are found by a procedure which scans the allowed four-dimensional parameter space and finds, for each efficiency, the set of cut values which gives the lowest background rate. The method is illustrated in Figure 7.5: The parameter space is scanned in equal probability bins for reasonable values of the selections; Figure 7.5 shows the efficiency for signal and the background rate corresponding to each parameter set at low luminosity. The left edge of the collection of points corresponds to the parameter sets with highest efficiency and lowest background. Each point on the curve represents a set of selections which give the best performance. This procedure takes into account all possible correlations amongst the trigger quantities.

7.6.4 Efficiency vs. E_T Studies

As explained in chapter 5 the cluster–E_T threshold value for a trigger menu is below the E_T value on the menu. For example, for the trigger menu single electron at low luminosity $e25i$ the cluster–E_T threshold value is 22 GeV for both Level2 and Event Filter. Figures 7.6 (a), (b) and (c) show the efficiency as a function of the Level2 and Event Filter E_T threshold value for single 15 GeV electrons at low luminosity, 25 GeV single electrons
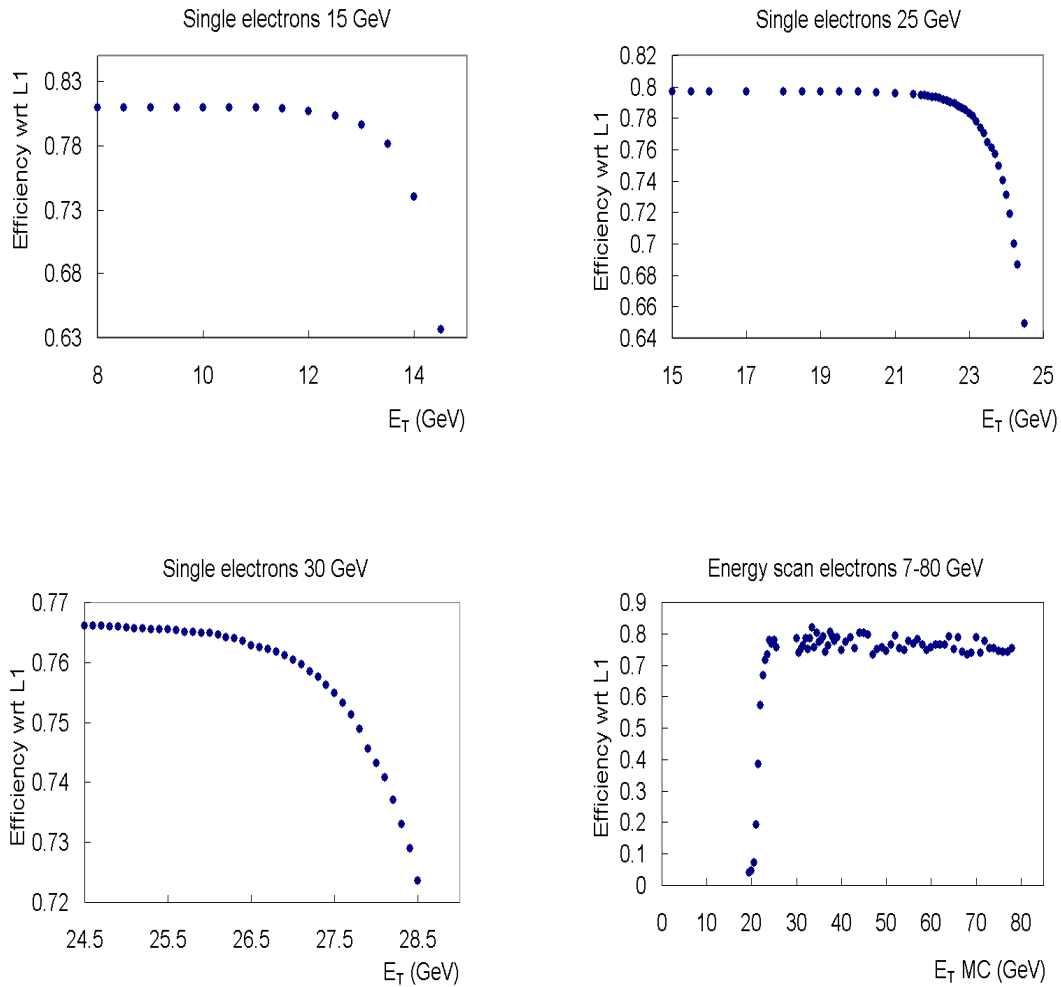
Figure 7.6: Inclusive electron trigger efficiency vs. E_T

at low luminosity, and 30 GeV single electrons at high luminosity respectively. For the low luminosity electrons the efficiency is constant and abruptly drops after the E_T threshold cut value for the trigger menu: 22 GeV for $e25i$, 27 GeV for $e30i$ and 12 GeV for $e15i$. On the contrary for the high luminosity case the drop in efficiency after the E_T threshold value is smoother due to the difference in pile–up. This is due to the fact that the energy spectrum of high luminosity electrons is broader than for low luminosity single electrons due to pile–up effects.

Since the lateral and longitudinal extent of both e.m. and hadronic showers depend on the incident energy, the shape–dependent trigger quantities depend on E_T. For example, as showers become more energetic, they deposit more energy in the hadronic calorimeter and in the last sampling of the e.m. calorimeter. Figure 7.6(d) shows the efficiency as

Table 7.5: Trigger efficiencies and relative efficiency for the single electron trigger $e25i$ for no pile–up and low luminosity. The trigger selection at each level is factorized by detector: calorimeter, inner detector, combined calorimeter–inner detector.

| | $e25i$ | $e25i$ low | |
Trigger Selection	Trigger Efficiency (%)	Trigger Efficiency (%)	Relative Difference (%)
L1	95.5 ± 0.2	96.8 ± 0.2	1.3
L2Calo	92.9 ± 0.3	93.4 ± 0.4	0.5
EFCalo	90.0 ± 0.4	91.6 ± 0.3	1.6
EFID	81.9 ± 0.2	82.9 ± 0.2	1
EFIDCalo	76.2 ± 0.4	78.4 ± 0.4	2.2

function of the MonteCarlo cluster–E_T for the 25 GeV trigger thresholds $E_T = 22$ GeV for an energy scan $7 - 80$ GeV of single electrons at low luminosity. The efficiency is constant or increases for higher E_T, within the E_T range shown (data samples at higher E_T were not available). Thus, proving that the electron trigger selection cuts are independent of the E_T for a given trigger menu.

7.6.5 Pile–up Studies

As described in Chapter 3 any collision recorded in the ATLAS detector contains a superposition of particles coming from several events. Therefore it is essential to understand the effect of pile–up on the electron trigger efficiency for both low and high luminosity scenarios.

The currently achieved HLT performance for the single isolated–electron $e25i$ and $e30i$ trigger was studied as a function of the main steps in the Level2–EF trigger chain for simulated events with no–pileup added. Efficiencies are given for single electrons of $p_T = 25$ GeV and $p_T = 30$ GeV already selected by Level1, averaged over the full pseudorapidity range $|\eta| < 2.5$. As quoted before the efficiency of the Level1 selection is 95%. If we compare the trigger efficiencies obtained with and without pile–up for these trigger items (see Table 7.5 and Table 7.6) we observe that the efficiency is increased when adding pile–up: 2% for the the $e25i$ at low luminosity and 4% for the $e30i$ trigger at high luminosity.

7.6.6 Level2–Event Filter Boundary Studies

The use of system resources in the electron HLT can be minimized by exploiting the modularity of the trigger. By ordering the trigger steps so that events are rejected as early as possible, both the overall processing times and data transfer rates may be reduced. Factorizing the trigger algorithm components also provides felxibility to shift the rejection power from Level2 to Event Filter or vice–versa, to optimize efficiency of the physics selection, rejection of high–rate backgrounds, and use of system resources. These

Table 7.6: Trigger efficiencies and relative efficiency for the single electron trigger $e30i$ for no pile–up and high luminosity. The trigger selection at each level is factorized by detector: calorimeter, inner detector, combined calorimeter–inner detector.

	$e30i$	$e30i$ high	
Trigger Selection	Trigger Efficiency (%)	Trigger Efficiency (%)	Relative Difference (%)
L1	95.7 ± 0.2	98.8 ± 0.2	3.1
L2Calo	91.3 ± 0.2	95.3 ± 0.3	4
EFCalo	89.3 ± 0.4	94.3 ± 0.2	5
EFID	79.2 ± 0.2	85.7 ± 0.4	6.5
EFIDCalo	73.4 ± 0.4	77.7 ± 0.4	4.3

issues have been extensively studied in the past [59].

If the rate for a trigger item from any level in the selection is too high, one can reduce it either by raising the E_T threshold of the trigger menu item or by tightening the selection criteria. However, this results in a loss in efficiency for physics signals. The loss in physics may partly be recovered by adding more exclusive trigger selections for the channel of interest, but the contribution to the overall rate of these extra items must be taken into account. There are long–term ongoing studies, performed together with the ATLAS physics community, to assess the impact of such changes in order to prepare for alternative scenarios.

The preferred and easiest way to reduce the rate is to raise the energy thresholds. The Level1 is dominated by the contribution from single high–p_T e.m. objects. As an example, raising the thresholds by $E_T = 5$ GeV of the single electron trigger would yield in a final HLT rate of 12 Hz at low luminosity. This is also seen in figure 7.7, which illustrates the impact of raising the threshold for the single–electron HLT selection at low luminosity (nominal threshold of 25 GeV) for $W \rightarrow e\nu$ events. Only events that passed the Level1 selection and for which the electron has $p_T > 25$ GeV at the generator level have been considered. As the threshold is increased, the efficiency to select these events decreases gradually.

As illustrated above, the HLT strategy contains considerable flexibility. Various possibilities exist to adjust the balance between minimizing the required computing resources and maximizing the physics performance. For many channels of interest, the selection scheme also provides considerable redundancy.

7.7 HLT Photon Physics Performance

Trigger efficiencies and jet rejection have been studied for the double object photon trigger $2\gamma 20i$ at low luminosity [75]. The single object photon trigger $\gamma 60i$ has not been studied due to technical problems with the simulation. The high luminosity scenario have
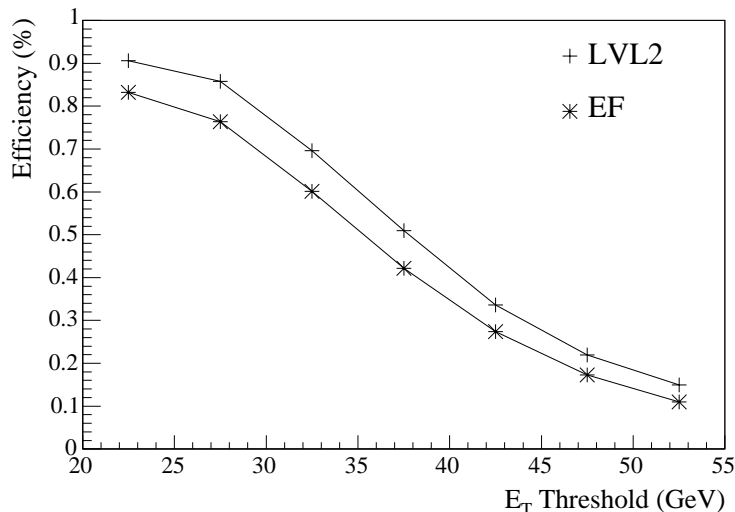
Figure 7.7: Efficiency to select $W \to e\nu$ events at Level2 and Event Filter as a function of E_T threshold in the trigger menu $e25i$ at low luminosity.

Table 7.7: Rejection of jets with $p_T = 17$ GeV at low luminosity in $\eta < 1.37$ or $1.52 < \eta < 2.47$. The jet rejection is given relative to the number of jets after the Event Filter calorimeter selection.

η region	Jet Rejection
$0 < \eta < 0.8$	1250
$0.8 < \eta < 1.37$	1000
$1.80 < \eta < 2.00$	1150
$2.00 < \eta < 2.35$	1050
$2.35 < \eta < 2.47$	2050
all	1100

not been studied do to unavailable data samples.

7.7.1   Efficiency and Rates

The overall trigger efficiency of the double–photon trigger $\gamma20i$ at low luminosity after Level2 calorimeter selection is 93% which is further reduced to 81% after the Event Filter calorimeter selection. The final rate after the Level2–Event Filter calorimeter selection is 8 ± 3 Hz. The overall jet rejection rate after the Level2–Event Filter selection for different η ranges is presented in Table 7.7. A more detailed descreption about the photon calorimeter trigger selection can be found in [75].

Figure 7.8 shows the photon efficiency and jet rejection factor with respect to Level1 as a function of two Level2 shower shape variables: lateral shape in the second sampling R_η^{shape}, and lateral shape in the first sampling R_η^{strip}. The jet rejection with respect to Level1 after the Level2 calorimeter selection is ~ 10 for the $\gamma 20i$ trigger.
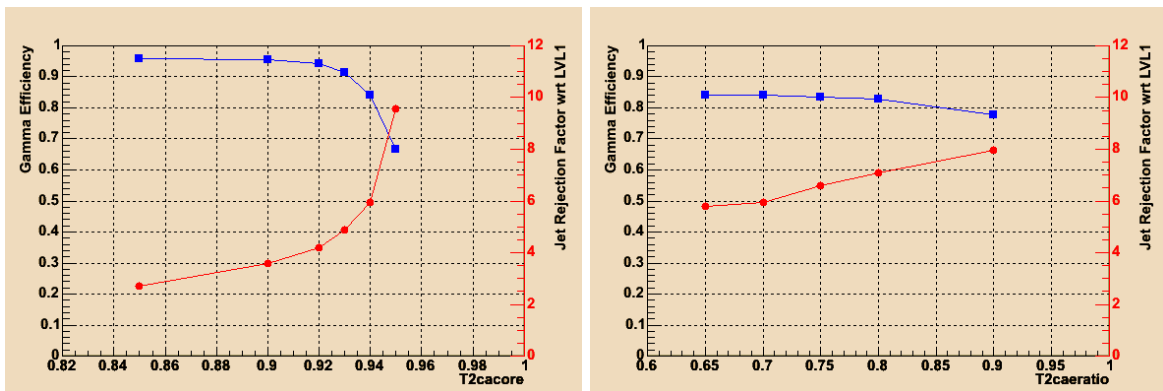

Figure 7.8: Photon Trigger Efficiency and Jet rejection with respect to Level1 as a function of the Level2 shower shape variables cuts at low luminosity for photon trigger $p_T = 20$ GeV: lateral shape in the second sampling R_η^{shape} (left), and lateral shape in the first sampling R_η^{strip} (right). On the plot the squares is the photon sample and the circles is the jet sample $p_T = 17$ GeV.

The photon trigger efficiency for $\gamma 20i \times 2$ obtained is comparable with previous past studies were a single photon efficiency of $\sim 80\%$ is obtained for a final jet rejection of 1270 ± 80. These latter studies include the use of Inner Detector information at the Event Filter to recover photons from conversions [54].

7.8   System Performance

Timing performance is one of the most crucial issues related to HLT selection and reconstruction algorithms, especially at Level2, and thus has to be continously optimized to meet the design target.

A first assessment of the system performance has been made for the HLT selection in view of its high demanding environment in terms of execution time and latencies for data transfers. The algorithm execution times per RoI have been measured for both calorimeter and tracking reconstruction as well as data preparation times.

7.8.1   Level2 Selection

As described in Chapter 4.4 the HLT algorithms are structured in a data preparation and feature extraction (execution) part. The raw data in the bytestream format in which they are held by the ROBs can be viewed as a representation of the raw data information in an event. The RDOs, organized by Detector Element, are another representation of this information. The conversion from bytestream representation to RDO representation

is called data preparation . The conversion is performed on demand of an HLT algorithm. Their implementation consists of a general infrastructure part that uses subdetector specific methods for decoding the information from bytestream format to RDO format.

The algorithm execution times per RoI for calorimeter cluster reconstruction and the corresponding data preparation time (raw data access time and the preprocessing time of these data in such a way, that they can be easily and efficiently used by the algorithms) were estimated for the Level2 in a dedicated test-bed which consisted of a farm of 2.2 GHz processors.

Figure 7.9 shows the main contributions to the total latency for a sample of di–jets events at start–up luminosity in a RoI size of $\Delta\eta \times \Delta\phi = 0.3 \times 0.3$ RoIs. Pure algorithm execution is completed within 500 μ s, while data access is typically completed within 1.8 ms for 95% of the events.The reconstruction algorithm time per RoI is ~ 3 ms for the tracking reconstruction. Continuous effort is put in improving these timings, nonetheless, they are already within target mean processing time at start-up (~ 10 ms).
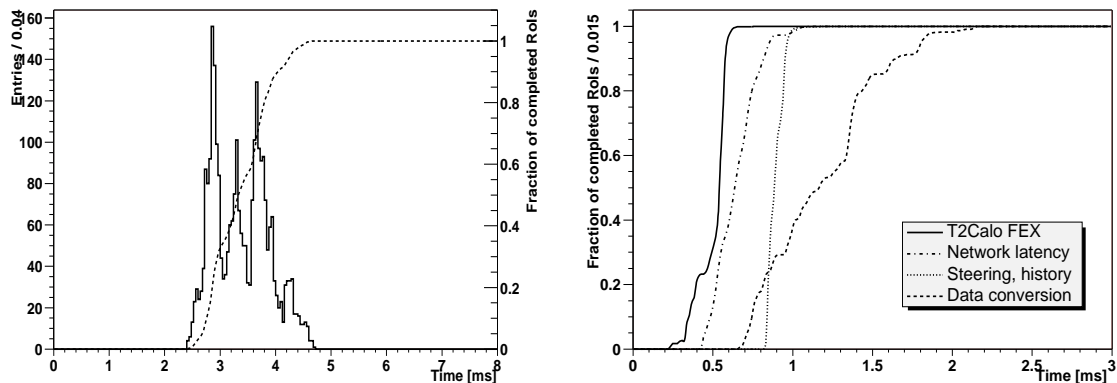

Figure 7.9: Total latency for RoI processing (shown at left) in the Level2 calorimeter trigger for di-jet events at startup luminosity. The dotted curve is the integral of the distribution, showing that 95% of the events are processed within 5ms. The four main contributions to the total latency are shown (right) as curves of integrals. The contributions are (in order of decreasing importance): data preparation and conversion, framework overheads, network access time, and algorithmic processing.

7.8.2   Event Filter Selection

A first study of the system performance of the offline calorimeter, patter recognition and cluster–track matching algorithms has been performed. The overall timing per event is not in the design target of the Event Filter average processing time. The main concern was not the absolute time but by which factor the time is increased when pile–up and electromagnetic noise are added in the calorimeter.

Table 7.8 shows the average processing time for calorimeter and Inner Detector reconstruction of the full event recosntruction of single electrons $p_T = 25$ GeV ($p_T = 5$ GeV; $\Delta\eta \times \Delta\phi = 0.5x0.5$) in the case of signal with no pile–up and pile–up added (low

Table 7.8: Average recosntruction time per event including the time to reconstruct the first event for single electrons $p_T = 25$ GeV at signal, and low luminosity.

Selection	Signal	Low Luminosity
EM Calorimeter	155 ms	0.945 s
ID: iPatRec	40.3 ms	1.01 s
ID: xKalman	52 ms	0.5 s
Cluster–Track Matching	61.8 ms	0.918 s
Total time/event	0.3 s	3.34 s

Table 7.9: Average reconstruction time per event including the time to reconstruct the first event for single electrons $p_T = 30$ GeV with and without electronic e.m. noise in the calorimeter.

Selection	No Noise	With Noise
EM Calorimeter	0.205 s	20.75 s
ID: xKalman	24.2 ms	29 ms
Cluster–Track Matching	31.4 ms	450 ms
Total time/event	0.52 s	22.8 s

luminosity). The timing results were obtained using a 1 GHz CPU and they include the time to reconstruct the first event. The table shows that at low luminosity the average time to reconstruct an event is incremented by a factor of ~ 10 compared to no pile–up. The system performance was also studied for a physics sample $Z \rightarrow ee$ were the average time per event was incremented by a factor of 4.5 when going from a low to a high luminosity scenario.

The effect in the processing time of a full event when adding calorimeter electromagentic noise has also been studied. Table 7.9 shows the average processing time for calorimeter and Inner Detector reconstruction of the full event of single electrons $p_T = 30$ GeV with and without calorimeter e.m. noise added. The addition of noise results in a factor of ~ 40 more in the average processing time.

Recently a seeded Event Filter selection software has been implemented and its system performance on a jet data sample at nominal design luminosity of 1×10^{34} $cm^{-2}s^{-1}$ has been assesed.

The Event Filter reconstruction processing time takes much less than the total average allowed time of one second. The times are per RoI calculated with a 2.8 GHz processor and extrapolated to the expected run conditions of 8 GHz or equivalent multicore hardware.[60]. The data preparation for both calorimeter and inner detector algorithms is around ~ 2 ms and the feature extraction time is ~ 5 ms for the calorimeter algorithm
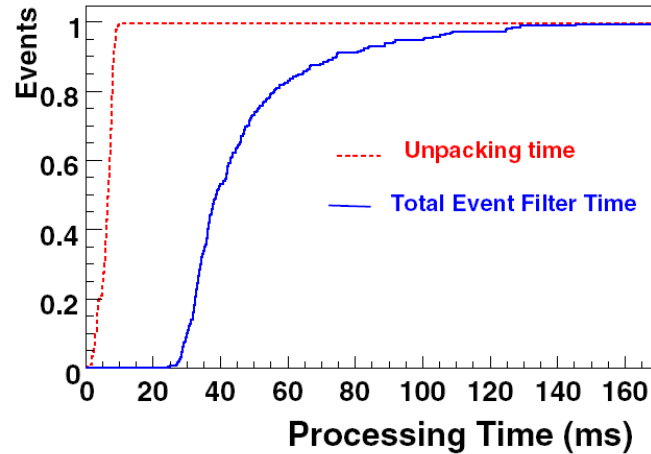
Figure 7.10: Total latency for RoI processing in the Event Filter calorimeter trigger for di–jet events at high luminosity. The integral distribution for both the data preparating and algorithm execution time are shown.

and ~ 20 ms for the tracking algorithm. The integrated distribution of the Event Filter execution time is shown in Figure 7.10.

The short consumption time opens up new possibilities in the use of the Event Filter which could lead to a better physics performance (efficiency increase). Nevertheless, further studies are needed.

Chapter 8

Triggering for Standard Model Higgs

The trigger efficiencies of the following Higgs decay channels with lepton and photons in the final state: $H \rightarrow \gamma\gamma$, $H \rightarrow ZZ^* \rightarrow 4l$, and $H \rightarrow WW^* \rightarrow l\nu l\nu$ decay via VBF have been studied for the low mass region, $m_H < 2m_Z$, . A large part of the physics programme will rely heavily on lepton and photon triggers. Given the required large selectivity of the ATLAS trigger $O(10^{-7})$ due to the rare signals of some of the Higgs decays at the LHC collider, it is essential to understand the efficiency at each step of the online e/γ event selection of a Higgs processes .

In the present study, the analyses of the lepton and photon Higgs decay modes in the low mass region ($m_H < 190$ GeV) have been performed using fully simulated events in the ATLAS detector. The trigger performance for these channels at start–up LHC luminosity (2×10^{33} $cm^{-2}s^{-1}$) and at design luminosity (1×10^{34} $cm^{-2}s^{-1}$) are presented. The electron and photon inlcusive triggers studied in Chapter 7.6 have been applied to select these Higgs processes. In addition, results from a trigger and offline electron/photon selection comparison of these channels has been addressed. As mentioned in Chaper5, the Higgs process $H \rightarrow 4b$ has the largest branching ratio but since the background is to high it cannot be triggered on (see Figure 5.1).

8.1   DataSets

The following Higgs boson decay modes have been considered in this analyses: $H \rightarrow \gamma\gamma$, $H \rightarrow ZZ^* \rightarrow 4e$, $H \rightarrow ZZ^* \rightarrow 2e2\mu$ and $H \rightarrow WW^* \rightarrow e\nu e\nu$ via VBF. All final states consist of at least one high p_T lepton or gamma.

The signal processes have been generated using PYTHIA 6.2 Monte Carlo event generator [67]. Initial–and final–state radiation have been switched on.

GEANT3 [68], the package for the full simulation of the ATLAS detector, has been used to perform the detector simulation for all processes considered. Pile–up was simulated by adding in average to these processes for the low (design) luminosity (4.6) 23 minimum bias events per bunch crossing in order to simulate the real LHC conditions. The effect due to electronic noise has been simulated as well.

Table 8.1: Trigger Menus, showing the inclusive trigger for Higgs processes including leptonic and photon decays for low and high luminosity. The trigger item e25i refers to the requirement that within the event at least one electron with an p_T of at least 25 GeV is efficiently selected, i means this object fulfills isolation criteria.

Object	Low luminosity	Design luminosity	Higgs Coverage
electrons	$e25i$ or $2e15i$	$e30i$ or $2e20i$	$H \to WW^*/ZZ^*$
photons	$\gamma60i$ or $2\gamma20i$	$\gamma60i$ or $2\gamma20i$	$H \to \gamma\gamma$
muons	$\mu20i$ or $2\mu10$	$\mu20i$ or $2\mu10$	$H \to WW^*/ZZ^*$
electrons + muons	$\mu10 + e15i$	$\mu10 + e20i$	$H \to WW^*/ZZ^*$

AS described in Chapter 7.6 the electron and photon trigger efficiencies fully simulated single electrons with transverse energy $p_T = 25(30)$ GeV and single photons with $p_T = 20(60)$ GeV have been used at low (design) luminosity to obtain the selection cuts for each trigger menu. To evaluate the trigger rates for these thresholds, around ten million fully simulated QCD dijet events were used. In addition, physics events such as $Z \to ee$, $W \to e\nu$, and direct photon production have been added according to their cross–sections. The events were generated with PYTHIA and on the parton level each jet was required to have a p_T of at least 17(25) GeV at low (design) luminosity. Events which would not pass the first level trigger are immediatly rejected before being processed by GEANT3 by applying a particle level filter before full simulation [65].

8.2   Selection Strategy

As described in Chapter 5 to guarantee optimal acceptance to new physics, the ATLAS online selection is presently based on an inclusive selection criteria, such as high p_T single and double object triggers. A large part of the physics programme will rely heavily on the inclusive single and dilepton triggers, involving electrons and muons for Higgs boson searches.

Table 8.1 shows the electron/photon trigger menus used for selecting the Higgs processes. For each trigger menu item the SM Higgs decay channels with electron and photons in the final state are shown for the low and high luminosity scenarios. In addition the table shows the trigger menu items for selecting the various Higgs decay channels in the low mass region. The energy thresholds of the trigger menus indicate the transverse energy value above which the selection has good efficiency for true objects of the specified type. For example, the inclusive single and di–photon triggers will select a light Higgs boson via its decay $H \to \gamma\gamma$ in case $m_H < 150$ GeV.

All channels considered in this study have electrons or photons in the final state and should be triggered by at least one of the trigger menu items for electron or photon objects. The ATLAS trigger acceptance covers the pseudo–rapidity region $|\eta| < 2.5$ for electrons and photons.

In the Higgs event selection, the electron–gamma selection applied has been optimized using single electrons and photons.

Using Monte Carlo simulations the performance of the electron/photons triggers has been evaluated in terms of the efficiency for the signal channels and the rate expected for the selection of the Level1, Level2 calorimeter and Event Filter trigger.

The online trigger steps are set up to select efficiently isolated electrons with a transverse energy (E_T) of at least 25 GeV at start-up luminosity. The electron efficiencies and expected rates for the single and double electron trigger after each trigger step factorized by detector are given in Chapter7. For an overall $76.2 \pm 0.4\%$ electron efficiency a rate of 46 ± 4 Hz has been found. This final rate is composed of 50% of clusters coming from 'real' electrons, (electrons from b and c decays and conversions). An efficiency of $57.3 \pm 1.5\%$ is found for the double electron trigger at low luminosity corresponding to a rate of a few Hz [76]. The efficiency to select two isolated photons was found to be 64% corresponding to a rate of 8 ± 3 Hz.

8.3 Physics Performance

The potential to trigger on Standard Model Higgs boson with electrons or photons in the final state has been studied for the low mass range $m_H < 2m_Z$ for the ATLAS experiment at the LHC. Analyses for the $H \rightarrow ZZ^*$, $H \rightarrow \gamma\gamma$ and $H \rightarrow WW^*$ decay modes have been evaluated using a realistic simulation of the expected detector performance for both the low and high luminosity scenarios.

In the present study the efficiency to trigger on a SM Higgs process is defined in two ways. The Trigger Efficiency is defined as the number of events accepted in a geometrical region in η and with certain transverse momentum. The Overall Trigger Efficiency is normalized with respect to events accepted in the whole phase space region.

The value of the kinematical cuts applied at Monte Carlo level were chosen to resemble as closely as possible the offline selection cuts applied in the physics performance study for a given Higgs channel decay [25, 77].

8.3.1 $H \rightarrow ZZ^* \rightarrow eeee$

Overall Efficiency

In addition to the electron identification criteria described in Chapter 6, the following kinematical cuts are applied at Monte Carlo level to the reconstructed events: two electrons with $p_T > 20$ GeV and $|\eta| < 2.5$ and two additional electrons with transverse momentum $p_T > 7$ GeV and $|\eta| < 2.5$.

The trigger efficiency for a Higgs with $m_H = 130$ GeV is shown in Table 8.2 for low and high luminosity scenarios. The trigger efficiency as well as the efficiency per electron trigger menu item are given. For the low luminosity scenario the trigger is found to select 96.7% of these Higgs events fulfilling the kinematic cuts specified above. The overall trigger efficiency for this scenario is 45.8%. The trigger efficiency for the high luminosity case is 95.5%. The trigger efficiency is very high because only one or two electrons are required at trigger level while four electrons are present in the event for this process.

Table 8.2: Trigger Efficiencies with respect to kinematical cuts as described in the text for the Higgs channels: $H \to 4e$ (130 GeV), $H \to 2e2\mu$ (130 GeV), and $H \to e\nu e\nu$ (170 GeV) at low and high luminosity.

Trigger	Luminosity	$H \to 4e$	$H \to 2e2\mu$	$H \to e\nu e\nu$
$e25i$	low	96.5 ± 0.2	76.2 ± 0.4	89.1 ± 1.2
$2e15i$	low	95.8 ± 0.2	63.7 ± 0.5	84.4 ± 1.4
$e25i$ or $2e15i$	low	96.7 ± 0.2	76.9 ± 0.4	89.5 ± 1.2
$e30i$	high	96.0 ± 0.4	70.1 ± 0.5	
$2e20i$	high	94.5 ± 0.4	59.4 ± 0.5	
$e30i$ or $2e20i$	high	95.5 ± 0.3	71.0 ± 0.5	

The Higgs invariant mass distribution for this channel $H \to ZZ^* \to 4e$ for a Higgs mass of 130 GeV at low luminosity is shown in Figure 8.1. The invariant mass was calculated with an offline analysis. The offline analysis used the same electron selection cuts used at the trigger electron selection. In the former case, the selection starts from e.m. clusters, a better calibration is performed and two additional cuts are used: e.m. cluster isolation and ID isolation. For further details on the Higgs mass window cuts see [78].
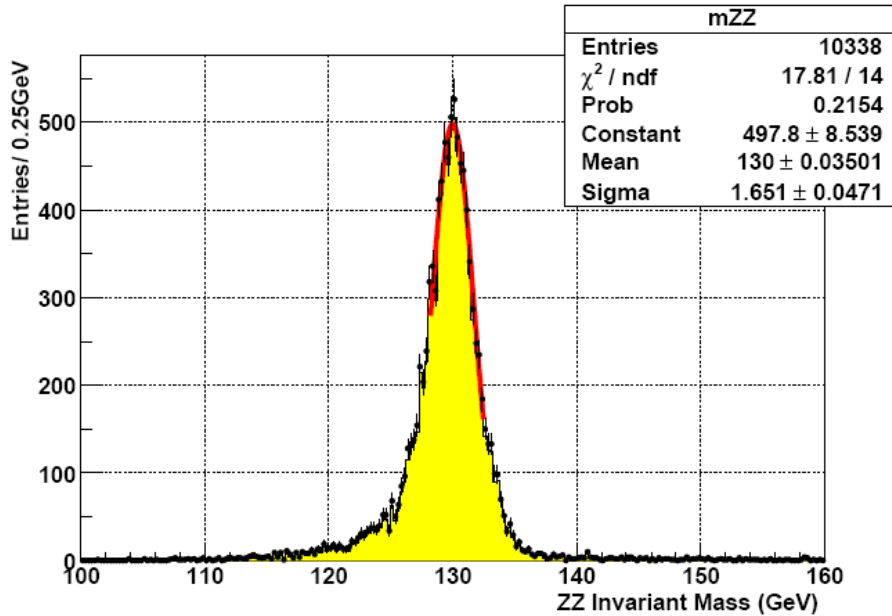
Figure 8.1: $H \to ZZ^* \to 4e$ invariant mass disribution for a Higgs Mass of 130 GeV for low luminosity.

Background processes

The decay channel $H \rightarrow ZZ^* \rightarrow 4l$ provides a rather clean signature in the low mass range for Higgs searches at the LHC. In addition to the irreducible background from ZZ^* and $Z\gamma^*$ continuum production, there are large reducible backgrounds from $t\bar{t}$ and $Zb\bar{b}$ production.

After the kinematic cuts are applied, the reducible backgrounds from $t\bar{t}$ and $Zb\bar{b}$ production are ten times higher than the irreducible one [79]. Since the overall uncertainties on these backgrounds are large, it is desirable to bring them well below the irreducible background from ZZ^* continuum production. This is achieved with an additional rejection of 100, which can be obtained using lepton isolation and vertexing measurements.
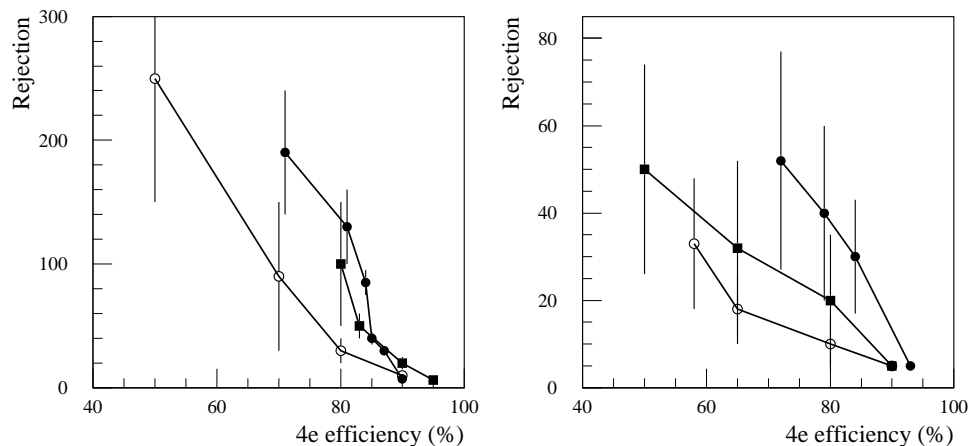
Figure 8.2: (left) Rejection of $t\bar{t}$ background versus overall efficiency for $H \rightarrow ZZ^* \rightarrow eeee$ final states with $m_H = 130$ GeV. The results are shown for track isolation at low luminosity (black circles), calorimeter isolation at low luminosity (black squares) and calorimeter isolation at high luminosity (open circles). (right) Same as left plot but for the $Zb\bar{b}$.

For the four electron final state, the results for the background rejections as a function of the efficiency for signal events with $m_H = 130$ GeV are shown separately for $t\bar{t}$ and $Zb\bar{b}$ events in Figure 8.2 both for low and high luminosity. Combining rejections (using isolation and impact parameter cuts) against the $t\bar{t}$ and $Zb\bar{b}$ reducible backgrounds at low luminosity, for a overall signal efficiency of 57%, a rejection of ~ 1200 (~ 130) against $t\bar{t}$ ($Zb\bar{b}$) can be obtained. At high luminosity, similar rejections are obtained for an efficiency of 47%, a rejection of ~ 800 (~ 50) against the $t\bar{t}$ ($Zb\bar{b}$) backgrounds can be obtained [25].

Invariant Mass Studies

The dependence of the trigger efficiency on the Higgs invariant mass was also studied for SM Higgs process $H \rightarrow eeee$ at low and high luminosity. Figure 8.3 shows the trigger efficiency as a function of the Higgs mass for low and high luminosity.

The trigger efficiency increases slightly with the Higgs mass. For an invariant mass of 300 GeV the overall trigger efficiency is 99.4% (98.4%) at low (high) luminosity. This

is expected since for larger Higgs masses the electrons of the decay are more energetic and well above the trigger threshold.
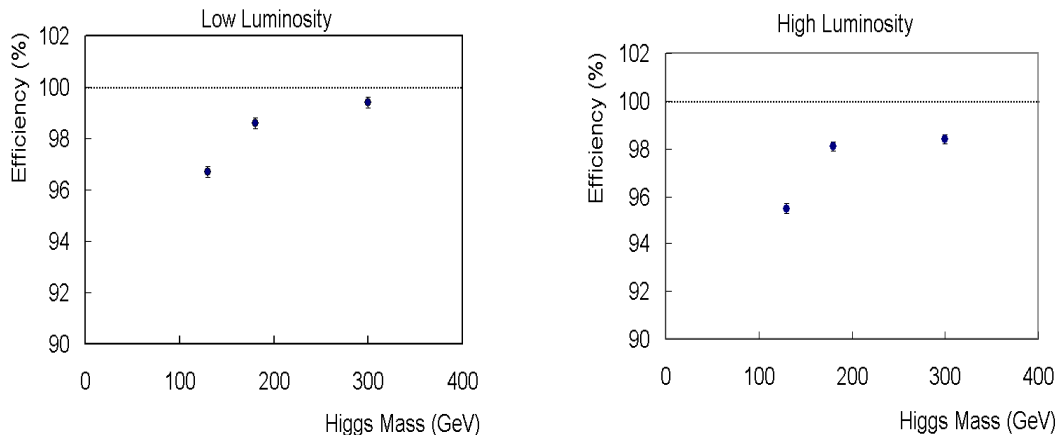

Figure 8.3: Trigger Efficiency as a function of the Higgs mass for the Higgs channel $H \to ZZ^* \to 4e$ for low and high luminosity.

8.3.2 $H \to ZZ^* \to ee\mu\mu$

Overall Efficiency

The electron identification criteria described in Chapter 6 for this process is preceeded by the following kinematical cuts at MC level after event reconstruction: two leptons with $p_T > 20$ GeV and $|\eta| < 2.5$ and two additional leptons with transverse momentum $p_T > 7$ GeV and $|\eta| < 2.5$ are required. Figure 8.3 shows an event display of this Higgs decay process in a ρZ projection in barrel and endcap calorimeters of the ATLAS detector.

The trigger efficiency for a Higgs mass of 130 GeV for the single and double object electron trigger menu is shown in Table 8.2 for low and high luminosity scenarios. For the low luminosity scenario the trigger is found to be 76.9% efficient selecting these events. The overall trigger efficiency for this scenario is 29.9%. The trigger efficiency for the high luminosity scenario is 71.0%. If instead two electrons with $p_T > 20$ GeV and $|\eta| < 2.5$ are required as kinematical cuts at the MC level the trigger is found to be 93.7% (90.5%) efficient selecting electrons at low (high) luminosity.

Furthermore, if the muon and electron plus muon trigger menus are included ($\mu 10+ e15i$ for low luminosity and $\mu 10 + e20i$ for high luminosity) in the analyses the trigger efficiencies for this process will increase by at least 20%. This study has not been performed as the complete μ trigger selection has not been available yet.
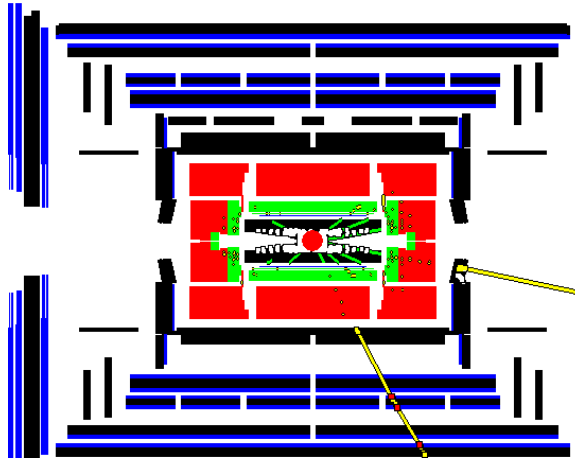
Figure 8.4: Event display of the Higgs process $H \to ZZ^* \to 2e2\mu$. ρZ projection in barrel and endcap calorimeters of the ATLAS detector.

8.3.3 $H \to WW^* \to e\nu e\nu$ via VBF

Overall Efficiency

The final state associated with events from these leptonic decay processes include the two quark jets from the hard scattering in conjunction with two leptons and missing p_T from the decay of the W bosons. In this analysis two different kinematical cuts at MC level were applied to the leptonic selection of the reconstructed events. The selection required that these leptons were electrons with $p_T > 15$ GeV and $|\eta| < 2.5$.

The trigger efficiencies for a Higgs Boson with a mass of 170 GeV are given in Table 8.2 for low luminosity. In this study only the Level1 and Event Filter triggers are considered compared to the Higgs analyses discussed in the previous sections. The results should not differ considerably when the Level2 trigger is applied since the Level2 selection is set–up in such a way to not reject events prematurely. A trigger efficiency of 89.5% is obtained.

Furthermore, if the jet and E_T^{miss} trigger menus are included in the analyses the trigger efficiencies for this process will increase. This study has not been performed as the complete *jet* and E_T^{miss} trigger selection has not been available so far.

Background processes

For $m_H < 2m_Z$, vector boson fusion amounts in leading order to about 20% of the total Higgs production cross–section and becomes more important with increasing mass. Studies by the ATLAS collaboration have demonstrated that the ATLAS experiment has a large discovery potential in the $H \to WW^* \to l^+l^- P_T^{miss}$ channel [31].

The dominant backgrounds for this process are $t\bar{t}$ production where the W bosons from the top decays leptonically, and electroweak W pair production.

Table 8.3: Trigger Efficiencies with respect to kinematical cuts as described in the text for the Higgs channel: $H \rightarrow \gamma\gamma$ (120 GeV) at low luminosity.

Trigger	Luminosity	$H \rightarrow \gamma\gamma$
$\gamma 60i$	low	57.0 ± 0.7
$2\gamma 20i$	low	74.0 ± 0.6
$\gamma 60i \ or \ 2\gamma 20i$	low	83.0 ± 0.5

8.3.4 $H \rightarrow \gamma\gamma$

Overall Efficiency

In the analyses of this channel the following kinematical cuts at the MC level were applied to the selection of events: one photon with $p_T > 40$ GeV and $|\eta| < 2.4$, an additional photon with transverse momentum $p_T > 25$ GeV and $|\eta| < 2.4$ and photons in the barrel–endcap transition region $1.37 < |\eta| < 1.52$ are excluded.

The trigger efficiency for a Higgs mass of 120 GeV for the single and double object photon trigger menu is shown in Table 8.3 for low luminosity scenario. The trigger is found to be 83.0% efficient for this Higgs decay mode. The overall trigger efficiency for this scenario is 46%. The trigger efficiency in the η acceptance region is found to be consistent with previous studies [54].

The Higgs invariant mass distribution for this channel for a Higgs mass of 120 GeV at low luminosity is shown in Figure 8.5. The invariant mass was calculated with an offline analysis. The offline analysis used the same photon selection cuts used at the trigger photon selection. In the former case, the selection starts from e.m. clusters, a better calibration is performed and conversion information is also included. As can be noticed in the mentioned figure the reconstructed invariant mass is well calibrated and nicely gaussian although a low energy tail is still present mainly due to converted photons (yellow histogram in figure): 79% of the events are contained in the $\pm 1.4\sigma$ interval around the nominal Higgs mass while for a Gaussian distribution this fraction is expected to be 83.8%. For further details on the Higgs mass window cuts see [80].

Background processes

The $H \rightarrow \gamma\gamma$ is a promising rare decay channel for Higgs searches in the mass range 100 GeV $< m_H <$ 150 GeV, where the production cross-section and the decay branching ratio are both relatively large.

This decay places severe requirements on the performance of the electromagnetic calorimeter. Excellent energy and angular resolution are needed to observe the narrow mass peak above the irreducible prompt $\gamma\gamma$ continuum. Powerful photon identification capability is required to reject the large QCD reducible background in which one or two jets are misidentified as photons. The fine granularity of the first sampling of the electromagnetic calorimeter offers the possibility to separate photons from hadrons. A track veto and the
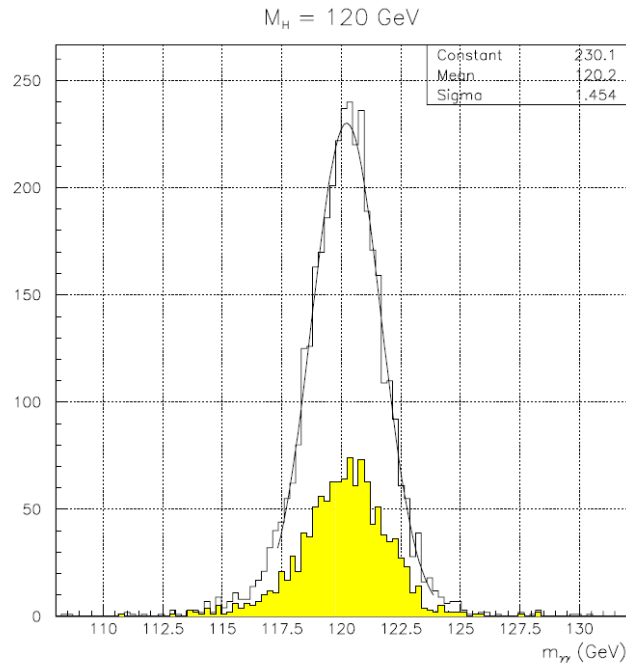
Figure 8.5: $H \rightarrow \gamma\gamma$ invariant mass disribution for a Higgs Mass of 120 GeV at low luminosity.

reconstruction with photon conversions will help further reduce the backgrounds.

The irreducible background consists of genuine photon pairs produced via the following three processes: Born ($qq \rightarrow gg$), box ($gg \rightarrow gg$), and quark bremsstrahlung ($qg \rightarrow qg \rightarrow qgg$).

In addition to the irreducible gg background, other potentially large background sources have to be considered. These include jet–jet and γ–jet events in which one or both jets are misidentified as photons, as well as $Z \rightarrow ee$ decays, where both electrons are mistaken as photons. Since the production cross–sections for these processes are many orders of magnitude larger than the signal cross–sections, excellent photon/jet and photon/electron discrimination are required [25].

For pairs of calorimeter clusters which pass the kinematic cuts and have an invariant mass in the range from 70 GeV to 170 GeV, the ratios of the jet–jet and g–jet cross–sections to the irreducible $\gamma\gamma$ cross–section are 2×10^6 and 8×10^2 respectively. There are large uncertainties on these ratios and on the fraction of jets which are expected to satisfy the photon identification criteria, arising from higher-order corrections and from uncertainties in jet fragmentation. In order to reduce these backgrounds to a level well below that of the irreducible $\gamma\gamma$ continuum, rejection factors of 2×10^7 and 8×10^3 are required.

The results are shown in Figure 8.6 as a function of the two photon invariant mass $m_{\gamma\gamma}$. After applying the full offline photon identification cuts from the calorimeter and the Inner Detector, the residual jet–jet and γ–jet backgrounds are found to be at the level of approximately 15% and 20%, respectively, of the irreducible $\gamma\gamma$ background over the mass
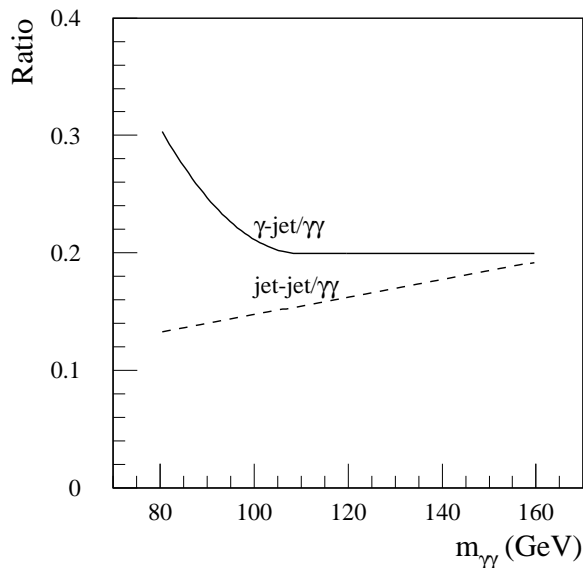
Figure 8.6: Expected ratios of the residual reducible jet–jet and γ–jet backgrounds to the irreducible $\gamma\gamma$–continuum background as a function of the invariant mass of the pair of photon candidates at high luminosity.

range relevant to the $H \to \gamma\gamma$ search.

8.4   Trigger vs. Offline Studies

A first study has been performed to detect if the Level1 RoI trigger selection is rejecting events prematurely. The analyses was performed on a SM Higgs process $H \to eeee$ data sample with invariant mass of 130 GeV at low luminosity [81].

As shown in section 8.2.1 the overall trigger efficiency for the $H \to ZZ^* \to eeee$ (130 GeV) was 96.7% when the Level1 e.m. RoI trigger step was applied as starting point for the selection before the EF selection step. If an EF trigger analysis is performed using e.m. clusters the overall trigger efficiency is 97.7%. Therefore, the Level1 RoI selection step of the former analysis rejects 1% of the events that would have passed the latter analysis. As described in chapter 6 the Level1 calorimeter selection is composed of a e.m. and hadronic transverse energy, and isolation cuts. The Level1 e.m. and hadronic isolation cuts slightly contribute to the loss in efficiency, only 0.1% of the events are lost applying these selection cuts. The main effect comes from the Level1 energy cuts. The Level1 has coarser granularity and digitized output compared to the offline selection which results in poorer energy resolution and therefore in less efficiency.

A second study performed has shown that less than 1% of the Higgs events that would fulfill a offline analyses criteria are rejected by the online selection presented here. The values and order in which the selection were applied for calorimeter, Inner Detector and Cluster–Track matching were identical for the trigger and offline analysis. These loss of events is mainly due to the fact that the L1 trigger selection is hardware based having only

coarse granularity calorimeter information available. This results in a poorer energy resolution compared to the offline selection. Another factor is that the offline and trigger electron identification strategies are slightly different and that the offline has a better calorimeter calibration available compared to the Level1 and the Level2 trigger.

Chapter 9

Combined Test Beam Data Measurements and Analysis

In this chapter electron/pion separation studies in the Level2 system performed with real data obtained in the 2004 ATLAS Combined Test Beam (CTB) are presented. A method to obtain pure samples of electrons and pions has been developed using beam line and TRT detector information and is used in this study. Trigger electron efficiencies and pion fake rates have been studied for different particle energies using calorimeter and tracking information from the Level2 trigger.

9.1 Motivation

The ATLAS experiment at the LHC is expected to start taking data from proton–proton collisions in 2007. In preparation for this phase, it will be essential to understand the detector performance and response and to gain experience on their combined operation. Thus, in the year 2004 a full slice of the ATLAS experiment has been tested with beams of different particles (pions, electrons, protons, photons and muons) at different energies, and polarities, ranging from 1 GeV up to 350 GeV providing a unique opportunity to evaluate the individual sub-detector performances, but also to exploit the full power of the ATLAS detector for detailed particle identification and measurement and to acquire a better understanding of the detector before the commissioning phase [82].

Excellent particle identification is one of the most important design criteria for the ATLAS experiment. The ATLAS electromagnetic calorimeter and Inner Detector systems are designed to identify electrons and photons in a wide energy range as explained in Chapters 3.2.1, 3.2.3 and Chapter 6. Good electron identification and e/π separation capability are especially important in the momentum range below 200 GeV. In that momentum range, a large number of pions are expected to be produced in the proton–proton collisions at 14 TeV. A fraction of hadronic showers may be fully contained within the e.m. calorimeter, creating a potential source of misidentification.

After the Level1 trigger, the Level2 trigger system has a critical role in the e.m. identification performance as was studied in Chapter 6. Indeed, the online trigger must be able to select electrons in a very efficient manner, while keeping the background rate to a

minimum.

In this chapter, electron/pion separation in the Level2 system has been studied using combined test beam electrons and pions at momenta of 20 GeV and 50 GeV. The results of this analysis are important, since this is the first and only occasion that a full slice of ATLAS has been assembled and tested before the full ATLAS detector becomes operational.

9.2   Combined Test Beam Setup

Test beam periods are crucial during the research and development period of a detector, since they represent a great opportunity to face and solve unexpected problems that might arise in a later stage of the detector operation. The Combined Test Beam (CTB) activity carried out between spring and fall of 2004 was particulary important, because small sections of all the ATLAS subdetectors using final or quasi–final readout electronics were integrated altogether for the first time with the Trigger and Data Acquisition system (TDAQ).

9.2.1   ATLAS Detectors

The testbeam table setup, which can be seen seen in Figure 9.1, resembled the geometry and setup of the full ATLAS detector as much as technically possible. The 2004 CTB tested a full barrel slice of the ATLAS experiment and made use of the CERN H8 beamline. The different components included were [83]:

- Inner Detector: was represented by three layers of six pixel modules, and four layers of two SCT modules each, wich were situated inside a magnetic field, and by two wedges of the barrel TRT placed just after the magnet.

- Calorimeters: the e.m. LAr calorimeter prototype module was housed inside a cryostat filled with liquid Argon. For the hadron Tile Calorimeter three barrel, and three Extended Barrel (EB) modules were used. All of the Tile modules except the barrel module at the bottom were production modules. When running with extended barrel modules, a small extra e.m. calorimeter was placed in front of the EB modules, to extend the coverage.

- Muon System: a couple of meters behind the table a part of the barrel Muon Spectrometer, a Monitored Drift Tube (MDT) chamber, was placed, while four more barrel MDT stations (seven chambers) were placed further downstream. One end–cap Cathode Strip Chamber (CSC), six end–cap MDT chambers at three stations, one end–cap Thin Gap Chamber (TGC) triplet, and two TGC doublets were also placed further downstream. There was also a muon trigger consisting of two 10×10 cm scintillators, two trigger stations of barrel Resistive Plate Counters (RPC), and two magnets installed.

The ID and calorimeter detectors are the first elements of the combined ATLAS assembly along the beam line. The pixel and SCT layers are placed within a bending
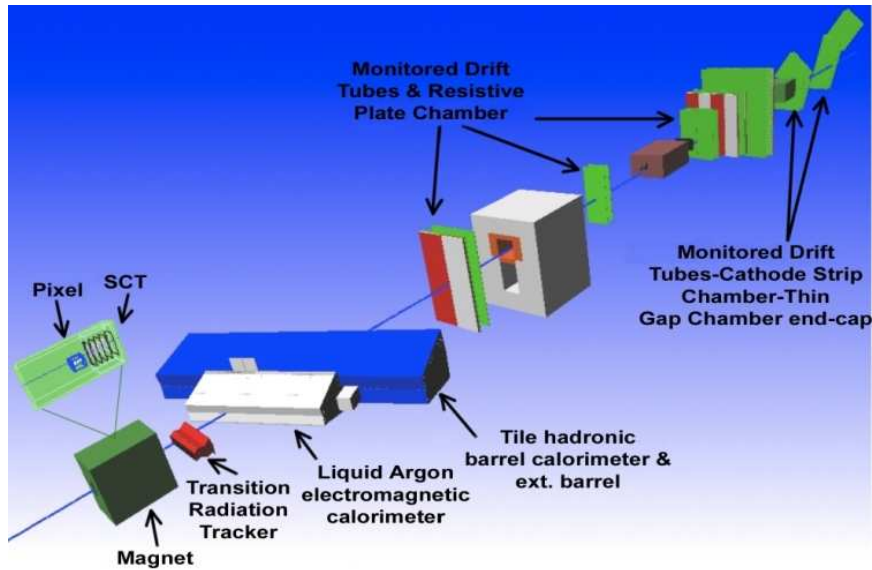
Figure 9.1: Schematic view of the experimental CTB setup in the CERN H8 are showing the architecture of the ATLAS test line: the detectors are positioned to receive the beam from the SPS. A muon particle which enters the magnet and crosses all detectors is shown (blue line).

magnet, providing a magnetic field of about 1.4 T; the distance between the last pixel layer and the first SCT layer is the same as in ATLAS ($\simeq$ 175 mm).The next element along the beam is the TRT system, at a distance of about 55 mm from the last layer of the SCT. This distance is larger than the one designed for ATLAS (40 mm) due to the extensions of the coils outside the magnet [84]. The TRT subdetector is followed by the LAr e.m. calorimeter and the TileCal. The distance between the last TRT layer and the LAr calorimeter is $\sim$ 782 mm. Following the beam line a magnet for bending the tracks in the horizontal plane and then the detectors of the muon spectrometer [85] (RPC, MDT, and TGC chambers) are found. The distance between the TileCal and the first component of the muon spectrometer is about 28 m.

To ensure the compatibility of the test beam data with the ATLAS general software framework, the slice assembled in H8 has been corresponded by convention to sector one in η and sector one in ϕ, as shown by the yellow area in Figure 9.2.

The reference frame for the whole experimental setup is shown in Figure 9.3 (the grey plane represents a generic subdetector layer). The beam goes through the different subdetectors (from left to right) along the X axis; the Y axis goes up vertically and the Z axis direction completes the right–handed reference. All the distances are referred to the interaction point.
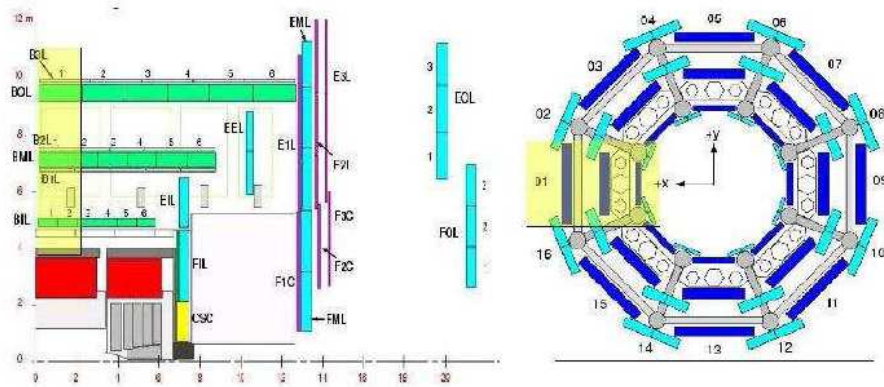
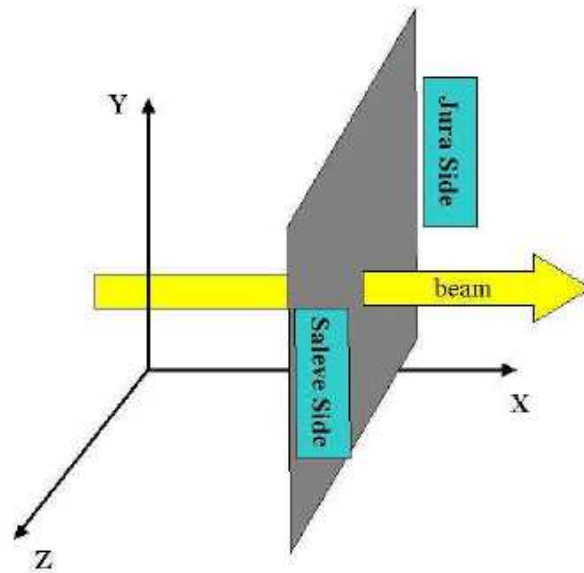Figure 9.2: The H8 slice refered to the H8 reference frame.

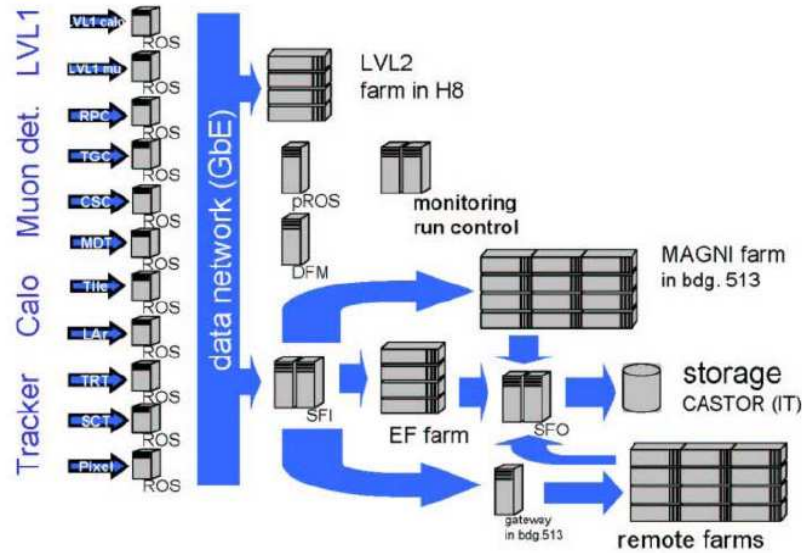Figure 9.3: The H8 reference frame.

Figure 9.4: Schematic diagram of the TDAQ setup in the CTB. Around 90 PCs and Single Board Computers were used to manage the flow of data, test event selection algorithms and provide control and monitoring.

9.2.2 Trigger and DAQ System

During the CTB, the latest prototype of the ATLAS TDAQ system was used for the data taking of all subdetectors. All ATLAS subdetectors need their own detector–specific DAQ development. As explained in detailed in Chapter 4.2, the readout electronics is controlled by a ReadOut Driver (ROD), custom–built electronics board for each subdetector. The ROD receives data events that are accepted by the Level1. The detector specific part of the DAQ system needs to control the ROD and respond to commands of the central DAQ (e.g. 'Start of run'). The ROD module sends event data to a Readout System (ROS). The Level2 runs specific algorithms in a computer farm. It can request subsets of data from different detectors in order to make the decision. During the CTB it was always running in 'spy' mode and was not filtering events. The data fragments received from the ROS are collected by the SubFarm Input (SFI) application and sent to the EF system. After this step, without modification or filtering, the SubFarm Output (SFO) stores them in a local disk. Finally, output files are transferred to mass storage system (CASTOR) [86]. Their data format is very similar to the one expected in ATLAS in 2007. Figure 9.4 shows a schematic view of the TDAQ setup during the CTB, indicating also the connections to the monitoring computers and other services. Around 90 PCs and Single Board Computers were used.

The Level2 farm for the testbeam was composed of a RoIB prototype and 4 single processor Intel Xeons running at 2.4 GHz and equipped with 1 Gb of memory each. This farm housed one L2SV, up to three L2PUs and a dataflow application used to transmit the Level2 to the EF, the so called pseudo-ROS (pROS). This unit had the responsibility of buffering the Level2 result and act like a normal detector read-out system as seen from

the event building side of the system. The in situ EF farm was composed of 4 nodes in the same configuration as for Level2. Other external EF farms were deployed throughout the testbeam. Every local EF node was running one Event Filter Dataflow Manager (EFD) and up to two processing tasks [87]. A possibility of operating a remote Event Filter farm, located outside CERN, was studied in its data flow aspect using the CTB setup. An Event Filter process running in Cracow was recieving a fraction of events, containing detector data in real time and was sending the data back (without processing it). Similar exercises with other remote Event Filter farms located in Edmonton, Manchester and Copenhagen were also done during the CTB, although no real detector data was involved in those cases.

Further development of the TDAQ subsystems which took place after the CTB period benefited from the direct experience of the system integration during the said period. Most ATLAS subdetectors, representing seven technologies from inner tracking to calorimeter and muon chambers, were integrated with the TDAQ in the CTB runs.

Besides the architecture of the first level, almost the entire architecture of the DAQ, including the High Level Trigger (Level2 and Event Filter) have been implemented. This quite complete test of the DAQ and the trigger will certainly shorten the detector commissioning in $2005 - 2007$.

9.2.3   HLT Algorithms

The Level2 system in the test beam was configured to run track fitting algorithms for the Pixel, SCT, TRT and muon detectors. The algorithms were scheduled by the HLT steering framework using many software components from the ATLAS offline detector description, Event Data Model and infrastructure software. The complete detailed description of the HLT Event Selection Software was given in Chapter 4.4.

Because of the nature of the tests executed in the CTB, many different parts of the Level1 hardware were being tested, switched on, off or simply re–configured. The Level1 Result contents therefore, could not be used as a seeder in Level2. In absence of RoI information for all detectors, a software simulation of the RoI data was used to initiate the event selection process. In an initial phase the raw data decoding software of a Level2 tracking selection algorithm was commissioned with beam data. Three Level2 tracking algorithms, IdScan, SiTrack and TRTxkalman [48]were run using alignment and calibration data. The obtained event/track features were encoded in the Level2 result record, which was send together with the Level2 decision to the EF farm. The Level2 Calorimeter algorithm T2Calo was n not included in the Level2 configuration. Histograms monitoring the selection process can be found in Appendix 3.

The algorithms running at the L2PUs, seeded by the L2SV, were able to take data from the ROBs, transform it into higher–level objects and apply algorithmic work. The Level2 decision and processing log were reused at the EF level to monitor and confirm Level2 analysis [87]. Another important exercise was the use of the collected data to develop and control the functioning of the entire offline software chain, from the condition database to the reconstruction program (in the Athena framework), to the graphics and to the Geant 4 simulation. For example, it has been possible to verify the data in the 'raw' format and in their definition 'in objects', their decoding and the conversion from one format to the other, their use and the access scheme, both in the trigger algorithms and in the reconstruction
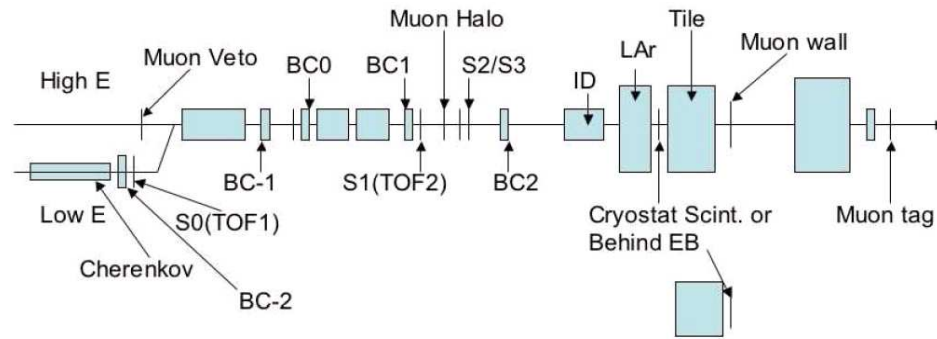
Figure 9.5: Schematic outline of the beamline instrumentation, and also of the ATLAS sub–detector elements.

programs, and finally their use 'online' for monitoring and calibration.

9.2.4 Beamline Instrumentation

The H8 beamline provided hadrons, electrons or muons with energies from 1 up to 350 GeV for the ATLAS CTB. The H8 beam is created by extracting a up to 400 GeV proton beam from the Super Proton Synchroton (SPS) towards the North Area, where the is directed onto the primary target (Beryllium up to 300 mm). Different target and absorbers are placed to produce a 'pure' electron or pion sample.

The beamline instrumentation used by the CTB consists of scintillators, beam–chambers, and Cherenkov detectors [83]. These detectors are used for the trigger, to get the beam position and quality, and for particle ID. The beam instrumentation is shown in Figure 9.5, including the last beam magnets.

Cherenkov Counters

There are three 1 m long Cherenkov counters along the H8 beamline. The first one is furthest upstream and named CHRV1. The two others are placed just upstream of the last bend of the Very Low energy (VLE) beamline, one on the straight beamline in case of higher momenta ($p_T > 10$ GeV), and the other one is placed on the deviated path for VLE mode, in both cases called CHRV2 (HE or VLE).

Beam Chambers

There are five beam chambers used to define the beam profile, these are designated BC-2 to BC2.

Scintillators

The scintillator, named Muon Veto (SMV), will tag unwanted muons coming from the straight high energy line. SO is used for checking the beam intensity and quality, and also for the Time–of–Flight, when running in VLE mode. The S1, S2 and S3 scintillators

Table 9.1: Summary of test beam data events used for the electron/pion separation study in the Level2 system. The beam energies and the dominant beam content is shown for each case. All the runs have the first magnet on except the one of π at 50 GeV.

E (GeV)	Nominal Beam	Run Number	Number of Events
20	e	2102413	10^4
20	π	2102389	10^4
50	e	2102400	10^4
50	π	2102350	10^4

are also used for checking the beam intensity and quality, and for the main trigger. The Muon Halo (SMH) is used for tagging halo muons and other particles. The Muon Tag (SMT) is used as a muon trigger or as a muon tag.

Time Of Flight

To supplement the Cherenkov counters at very low energy a Time Of Flight (TOF) measurement is used to improve particle identification.

9.3 Data Sets

The beam available in the H8 area was either a secondary or tertiary particle beam tuned for the energy and particle content. A 450 GeV primary proton beam is extracted from the SPS toward the North Aread and directed onto the primary target. The magnets located after the primary target provided the momentum selection for the secondary beam that contained mostly pions. Electrons were obtained in the tertiary beams. None of the beams available during the test beam runs were pure. The fractions of electrons and pions (or kaons) in the beam varied with beam setting. In addition, pion decays in flight originated muon contamination.

The CTB data used for these study was obtained during the 25 ns run period dedicated to the TDAQ system and all detector systems present. The beam impinged on the calorimeter at fixed incident angle and position corresponding to $\eta = 0.45$ and $\phi = 0$. The magnetic field surrounding the SCT and pixel systems was of 1.4 Tesla. Table 9.1 gives a summary of the runs used in this study. These runs contain around 10^4 particles and have been selected according to their particle type (electrons or pions) and energy (20 or 50 GeV). Unfortunately, during the complete CTB data–taking period, there was no pion run taken at 50 GeV with the first magnet on.

9.4 Beam Purity

Before the Level2 e/π separation performance can be assessed, it is necessary to have a good identification of electrons and pions which can be provided by detectors that

are not used by the Level2 algorithms in order to avoid biases in the selection.

Among the different devices present in the experimental area (see Figure 9.5), the following ones have been used to select a pure sample of electrons and a pure sample of pions: a pressure gas (filled with Helium) Cherenkov counter, situated at the beginning of the beam line element layout are suitable for e/π separation up to 50 GeV energy, a muon tag scintillator located at the far end of the beamline, and the TRT detector. Event though the TRT is not a beam filtering device, it can be used in this study because the HLT selection performance is only studied considering the Pixel, SCT and calorimeter systems.

The signal from the muon tag scintillator situated in the muon area, downstream of the beam line, is used first to remove the muon contamination. Figure 9.6 shows the signals in the for electron and pion beams at 50 GeV energy. Events with a signal in the muon scintillator greater than 480 ADC counts are considered as muons, and therefore excluded from the analysis. As it can be observed, and according to this selection criteria, the muon contribution to these data sets is in general very small, being more important in the 50 GeV pion beam.
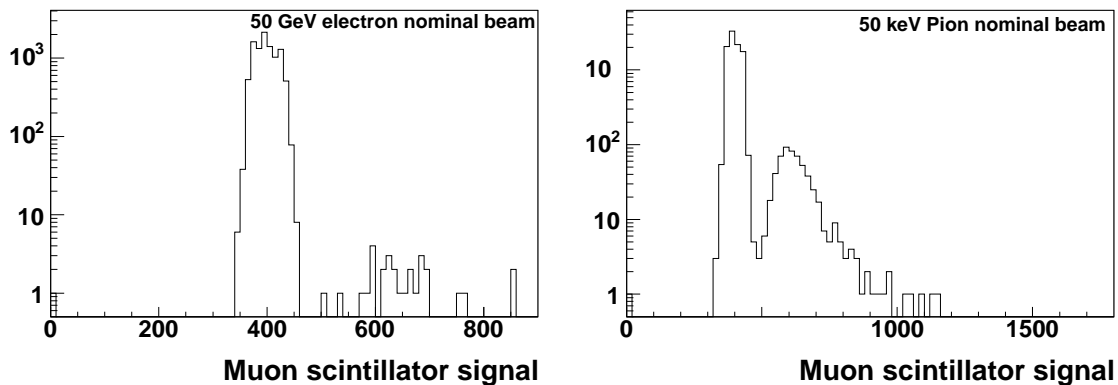
Figure 9.6: Signal distributions (in ADC counts) in the muon tag scintillators for nominal beams of 50 GeV electons and pions.

The TRT subdetector is used to identify electrons and pions. The criteria applied is the following:

- Selection of good tracks: only the events with one reconstructed track in the TRT are considered. In addition, the number of hits in the track has to be greater than 25. This applies equally to both the electron and pion samples.

- Cut on the number of high level (HL) hits (transition radiation hits) in the track; for electrons, the energy deposition in the TRT straws is dominated by transition radiation hits, while for pions, it is mostly due to δ–rays [66]. Electrons are required to have a track with more than seven HL hits while pions are required to have less than three. Figure 9.7 shows the number of HL hits for pions and electrons for an energy beam of 50 GeV.
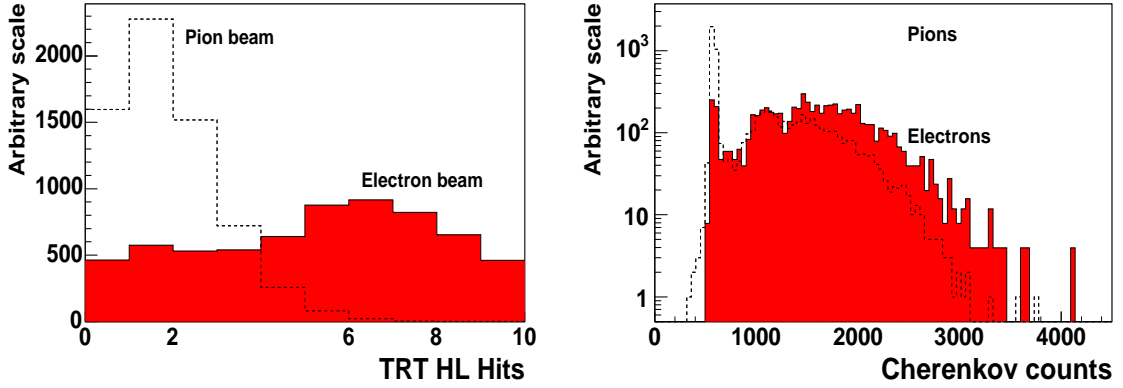
Figure 9.7: The left plot shows the number of High Level (HL) hits of the reconstructed tracks in the TRT subdetector. Distributions are shown for all events satisfying the good track condition criteria for a nominal beam of 50 GeV electrons (shaded) and pions. The right plot shows the signal distribution in the Cherenkov detector for electrons (shaded) and pions. Only events satisfying the TRT and muon tag filtering criteria are shown.

After the TRT filtering, little pion contamination remains in the electron sample and vice versa. The Cherenkov detector is then used to further clean up the electron and pion samples. Electrons are required to have more than 800 ADC counts in the Cherenkov detector. The opposite criteria is used to select pions. Figure 9.7 shows the signal of the Cherenkov detector for electrons and pions already pre–selected by applying the criteria of TRT and muontag. The Cherenkov selection performance is worse at 50 GeV than at 20 GeV (see Appendix 3).

The effect of all the previously defined selection criteria is shown in Figure 9.8, where the scatter plots of the signal in the LAr e.m. calorimeter and the Tile hadronic calorimeter are shown for nominal beams of 50 GeV electrons and pions, before and after beam particle filtering. As it can be observed, very little pion contamination remains in both samples after the selection. The final number of events in each sample after the preselection is 2500.

In order to calculate the purity of the electron and pion samples it is important to calculate the efficiency of finding electrons using the particle identification cuts for pions ϵ_e^π and the efficiency for finding pions using the particle identification cuts for electrons ϵ_π^e.

The efficiency ϵ_e^π is best measured in a beam of dominantly electrons. An upper limit can be calculated assuming the signals in the Cherenkov counter and the TRT detector give independent measurements. The efficiency for finding electrons when making cuts for pions is

$$\epsilon_e^\pi = (\epsilon_e^\pi)_{Ch}(\epsilon_e^\pi)_{TRT} \tag{9.1}$$

with $(\epsilon_e^\pi)_{Ch}$ and $(\epsilon_e^\pi)_{TRT}$ being the efficiencies for the Cherenkov counter and the TRT respectevily. Measuring the efficiencies is easy in a beam containing only electrons. Four different selection criteria can be defined:

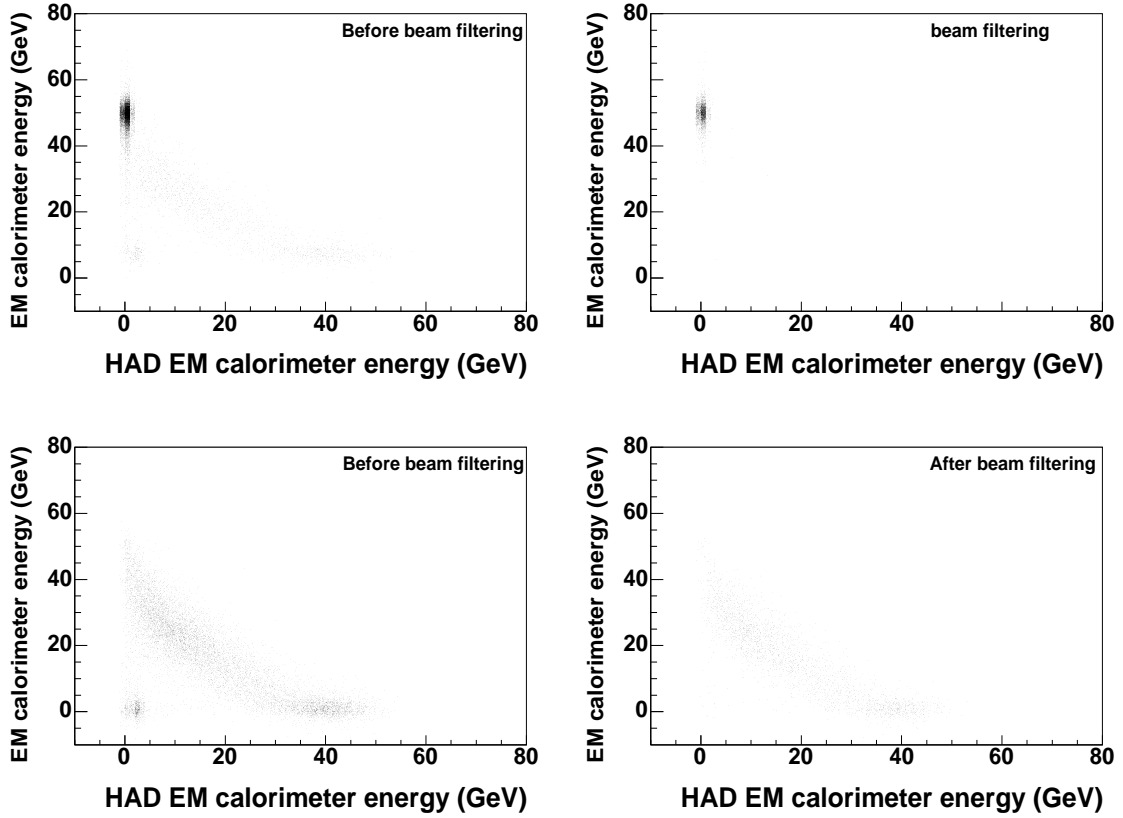- **A** Pion identification cuts in both the Cherenkov counter and the TRT.

Figure 9.8: Correlation plots of the signal in the LAr e.m. calorimeter and the Tile hadronic calorimeter for a 50 GeV electron (top) and pion (bottom) nominal beam. The plots are shown before (left column) and after (right column) beam filtering.

- **B** Pion identification cuts in the Cherenkov counter and electron identification cut in the TRT.

- **C** Electron identification cut in the Cherenkov counter and pion identification cut in the TRT.

- **D** Electron identification cuts in both the Cherenkov counter and the TRT.

With X_e and X_π defined as the number of electrons and pions after the criteria X the total number of particles X_{total} is given as

$$X_{total} = X_e + X_\pi = xX_e \qquad \text{where} \qquad x > 1. \tag{9.2}$$

Since the cuts on the Cherenkov counter and the TRT are independent:

$$(\epsilon_e^\pi)_{TRT} = \frac{C_e}{C_e + D_e} = \frac{1}{1 + \frac{D_e}{C_e}} \tag{9.3}$$

Table 9.2: Summary of test beam data events used for the electron/pion separation study in the Level2 system. The beam energies and the dominant beam content is shown for each case. All the runs have the first magnet on except the one of π at 50 GeV.

20 GeV	$\epsilon_e^\pi < (\epsilon_e^\pi)_{TRT}(\epsilon_e^\pi)_{Ch} < 0.072 \cdot 0.063 = 4.5 \cdot 10^{-3}$
	$\epsilon_\pi^e < (\epsilon_\pi^e)_{TRT}(\epsilon_\pi^e)_{Ch} < 0.0042 \cdot 0.016 = 6.6 \cdot 10^{-4}$
50 GeV	$\epsilon_e^\pi < (\epsilon_e^\pi)_{TRT}(\epsilon_e^\pi)_{Ch} < 0.053 \cdot 0.17 = 8.7 \cdot 10^{-3}$
	$\epsilon_\pi^e < (\epsilon_\pi^e)_{TRT}(\epsilon_\pi^e)_{Ch} < 0.00099 \cdot 0.62 = 6.2 \cdot 10^{-4}$

The fraction of pions in region D will be lower than in region C, so $c/d > 1$ using the notation from (9.2). Inserting this in (9.3) results in an upper limit on the efficiency

$$(\epsilon_e^\pi)_{TRT} = \frac{1}{1 + \frac{cD}{dC}} < \frac{1}{1 + \frac{D}{C}} \tag{9.4}$$

However, the large number of particles in region A indicate a large contamination of pions in the electron beam and (9.4) will be a pessimistic estimate.

The analyses of $(\epsilon_e^\pi)_{Ch}$ and $\epsilon_\pi^e < (\epsilon_\pi^e)_{TRT}(\epsilon_\pi^e)_{Ch}$ are similar to the calculation of $(\epsilon_e^\pi)_{TRT}$, yielding:

$$(\epsilon_e^\pi)_{Ch} = \frac{1}{1 + \frac{aC}{cA}} < \frac{1}{1 + \frac{C}{A}} \tag{9.5}$$

$$(\epsilon_\pi^e)_{TRT} = \frac{1}{1 + \frac{bA}{aB} + \frac{bE}{eB}} < \frac{1}{1 + \frac{A}{B} + \frac{E}{B}} \tag{9.6}$$

$$(\epsilon_\pi^e)_{Ch} = \frac{1}{1 + \frac{dB}{bD}} < \frac{1}{1 + \frac{B}{D}} \tag{9.7}$$

The results are summarised in Table 9.2.

An upper limit on the amount of electrons in the pion beam before the particle identification, is given by the fraction of events passing selection criteria D in the pion beam. This is scaled with the fraction of electrons actually passing this selection criteria (estimated from the electron beam).

After the beam purity cuts both beams will be pure to below the level of 10^{-4} which is sufficient for the electron identification studies were rejections below 5×10^{-3} are never reached. The electron contamination in the pion samples of 20 GeV (50 GeV) without any pre–selection was 4.5% ($\sim 0.1\%$), while the pion contamination in the electron samples at both energies was $\sim 19\%$. The contamination of electrons and pions in the pion and electron samples results negligible after the pre–selection cuts. The results are summarized in Table 9.3.

9.5   Level2 e/π Separation Performance

The Level2 electron/pion separation performance of the high–p_T single electron trigger was studied, 20 GeV and 50 GeV electron and pion filtered beam samples described

Table 9.3: The purity of the beams used for the HLT electron identification studies. Values are calculated before, and after applying the identification criteria in the Cherenkov counter and the TRT.

	Maximum fraction before selection		Maximum fraction after selection	
	20 GeV	50 GeV	20 GeV	50 GeV
electrons in pion beam	0.045	0.087	$2.9 \ 10^{-5}$	$5.4 \cdot 10^{-5}$
pions in electron beam	0.187	0.185	$8.3 \cdot 10^{-4}$	$1.6 \cdot 10^{-3}$

in the previous section were used. This samples, according to Table 9.3, were considered pure, and consisted of a single RoI per event, containing electrons and charged pions [88].

9.5.1 Level2 Electron Trigger Selection

As explained in Chapter 5, all algorithms at Level2 are seeded by the information coming from a RoI identified by the Level1 trigger. The Level1 trigger simulation used in the electron physics performance study in Chapter 7 is not used for the present step. Instead, in order to seed the Level2 trigger, a fixed RoI with the η and ϕ position of the beam is used. The Level1 RoI is then transfered to Level2 calorimeter algorithm T2Calo and the tracking algorithm IdScan. A detailed description of both algorithms was given in Chapter 6.

At the CTB most runs were not taken with LAr and Tile ROD in Physics Mode which means output was only in terms of raw ADC samplings. The Level2 calorimeter reconstruction algorithm T2Calo works with ROD Physics mode data (E, t, χ^2). Therefore T2Calo has been modified to make use of the offline calorimeter cells. For IdScan, a difference between the online tracking selection described in Chapeter 6 and the tracking performed in this study is that in this case only one track is reconstructed.

The cluster and track reconstructed by T2Calo and IdScan respectively, are used to select electrons based on the following criteria:

- E_T^{EM}: The transverse energy in the e.m. calorimeter calculated using the energies of all the electromagnetic layers in a 3×7 window around the RoI position.

- E_T^{HAD}: The transverse energy in the hadronic calorimeter.

- R_η^{shape}: The ratio of energy contained in a 3x7 cell window to that in a 7x7 cell window in the second sampling of the calorimeter.

- R_η^{strips}: The fractional difference in energy between the first sampling cell with the maximum energy, E1, and the second maximum energy, E2, in the first sampling of the electromagnetic calorimeter.

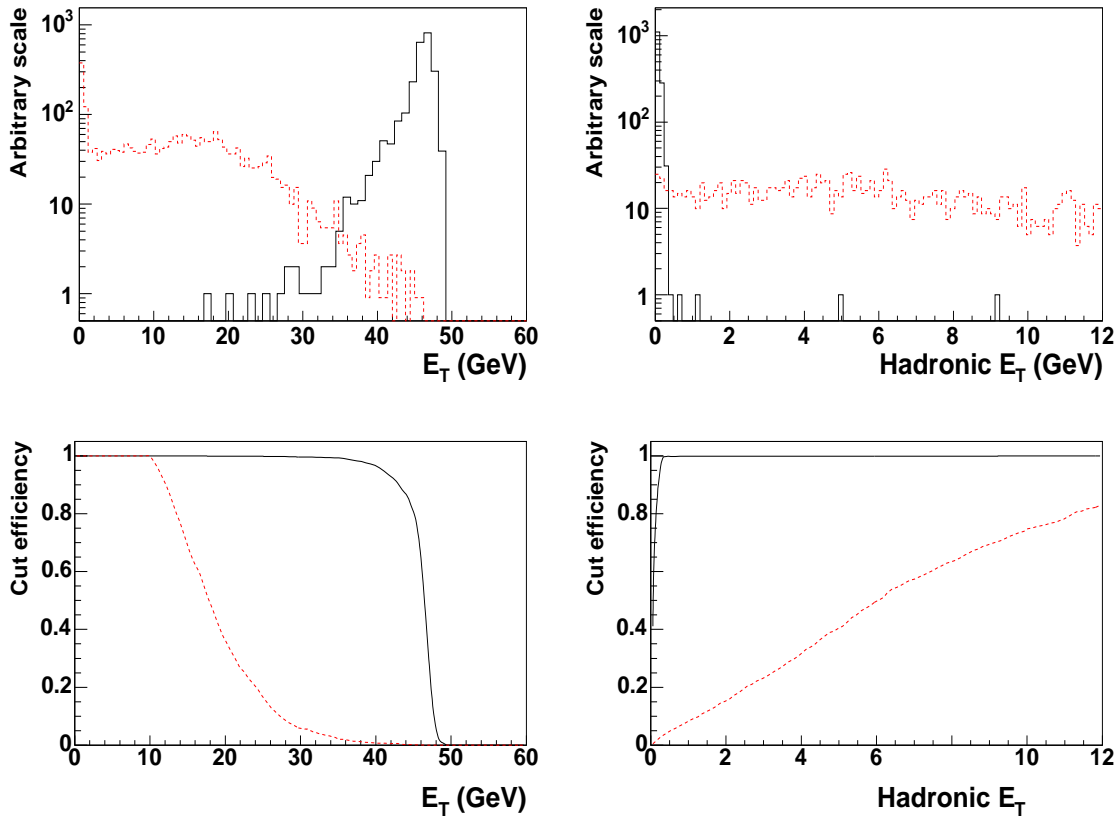- E_T/p_T: ratio between the cluster energy and the momentum of the reconstructed track.

Figure 9.9: Distributions of the transverese energy deposited in the second sampling of the e.m. calorimeter (E_T), and the transverese energy deposited in the first sampling of the hadronic calorimeter ($Hadronic E_T$) are shown for 50 GeV electrons (continous line) and pions (dotted line). The efficiency for selecting the corresponding particles as a function of the cut is also shown.

- $\Delta\eta$, $\Delta\phi$: position difference between the cluster and the track.

The distribution of the different Level2 calorimeter selection cuts are shown in Figure C.2 for an electron and a pion run of 50 GeV. The effect of these selection cuts on the trigger efficiency are shown independently for each selection variable. The distribution of the different Level2 tracking selection cuts are shown in Figure 9.11 and Figure 9.10 for an electron and a pion run of 50 GeV. The effect of these selection cuts on the trigger efficiency are shown independently for each selection variable.

9.5.2 Selection Optimization and Results

The variables described in Chapter 9.2.1 are optimized in order to obtain the the best pion rejection by independently varying the limit for each variable, while retaining $\sim 90\%$ Level2 overall electron selection efficiency. The optimization is performed first on
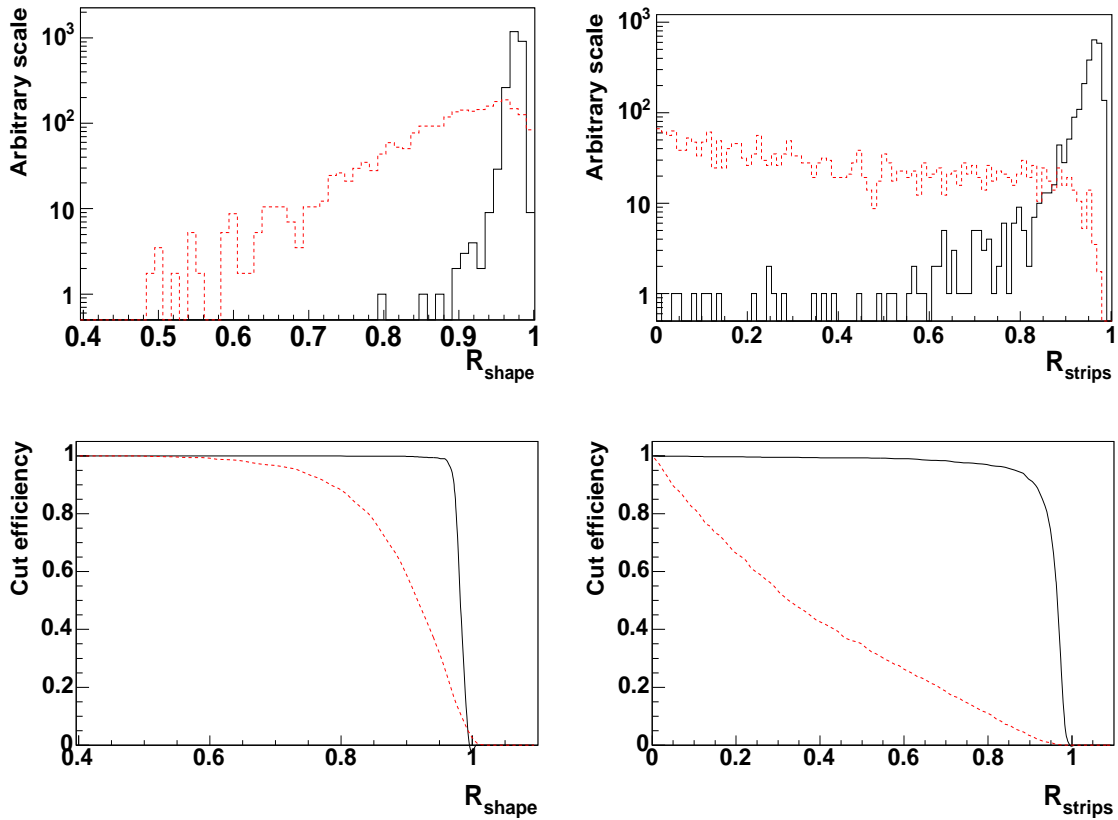
Figure 9.10: Distributions of the lateral shape in the second sampling of the e.m. calorimeter (R_{shape}), and the lateral shape in the first sampling of the calorimeter (R_{strips}) are shown for 50 GeV electrons (continous line) and pions (dotted line). The efficiency for selecting the corresponding particles as a function of the cut is also shown.

the calorimeter based variables trying to get the best pion rejection, while not loosing more than 4% of the electrons. Figures C.2, 9.10 and Figures 9.11 were used as guidance to get a first set of optimal cuts and then some fine tuning, was performed around these values. The cluster to track matching variables were then optimized applying the same criteria, and trying to obtain a final $\sim 90\%$ electron efficiency.

A set of optimized cuts was obtained separately for the 20 GeV and 50 GeV samples of electrons. The selection values can be found in Appendix 3 yield the best results. The performance achieved by the Level2 single electron trigger using the optimization criteria described above is given in Table 9.4. As it can be seen, for both energies under consideration, a pion fake rate of the order of seven per mil can be obtained for a Level2 selection efficiency of around 90%.

As explained in Section 9.3 the first magnet was turned off for the run of pions at 50 GeV. Therefore, it is difficult to optimize the selection cut for the variable E_T/p_T. As a conservative performance estimate, the value of the cut has been chosen to be the same
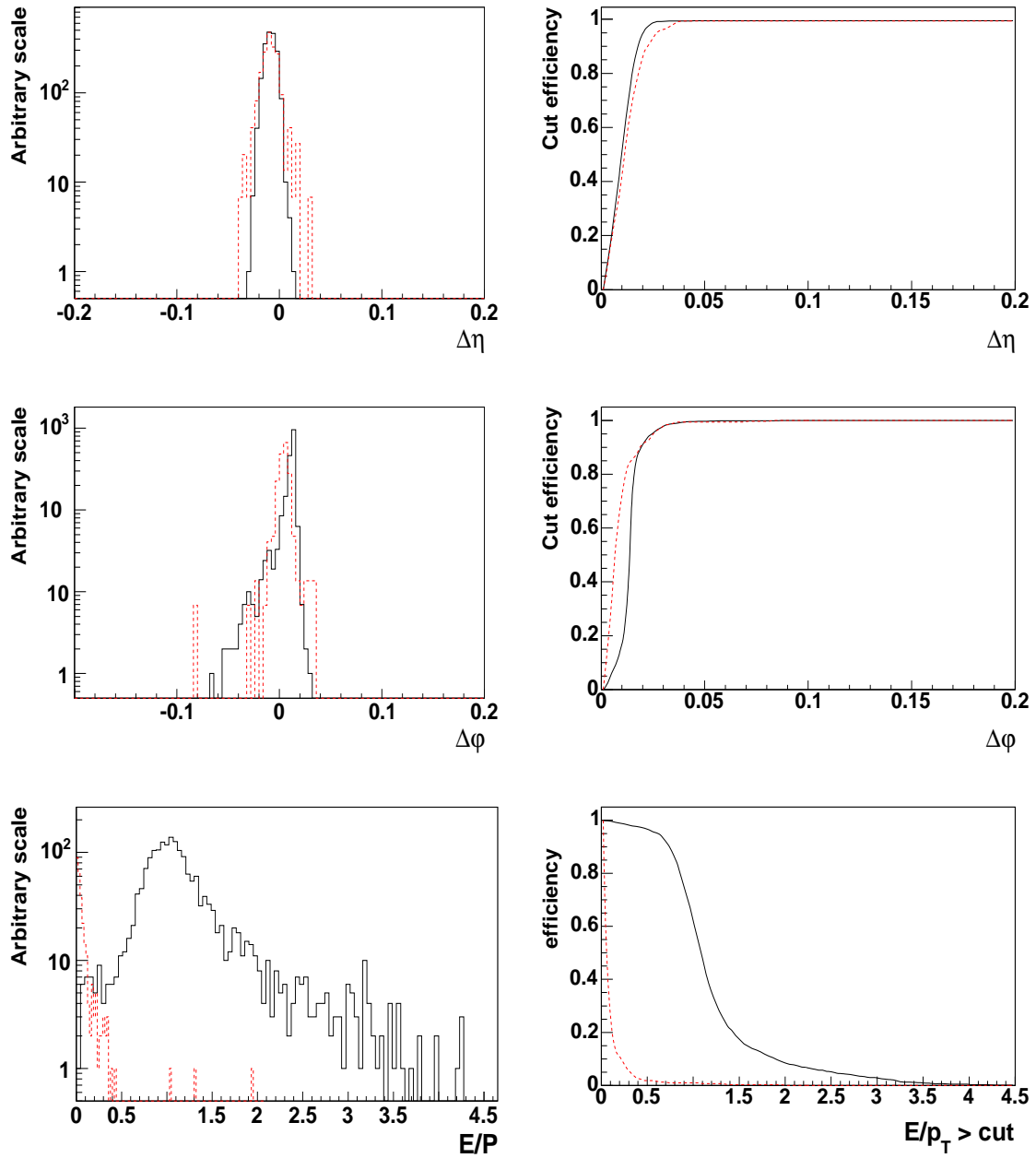
Figure 9.11: Distributions of the position difference between the cluster and the track in η ($\Delta\eta$) and in ϕ ($\Delta\phi$) as well as the distribution of the ratio between the cluster energy and the momentum of the reconstructed track (E_T/p_T) are shown for 50 GeV electrons (continous line) and pions (dotted line). The efficiency for selecting the corresponding particles as a function of the cut is also shown.

as for the 20 GeV particles. To further validate, the performance optimization has been done assuming that the distributions of E_T/p_T for pions in Figure 9.11 are correct. In this

Table 9.4: Efficiency results for 20 and 50 GeV samples. The cuts are tuned independently for both samples in order to have the best pion rejection, while retaining $\sim 90\%$ Level2 overall electron efficiency. The performance is also calculated for 50 GeV electron and pions using the cuts optimized for the 20 GeV samples.

Sample Energy	Selection cut	Efficiency (%)	Fake Rate (
20 GeV	Level2 Calo	95.56 ± 0.04	0.92 ± 0.04
	Level2 Matching	89.94 ± 0.04	0.67 ± 0.04
50 GeV	Level2 Calo	96.05 ± 0.04	0.33 ± 0.04
	Level2 Matching	90.02 ± 0.04	0.07 ± 0.04
50 GeV using 20 GeV tuned cuts	Level2 Calo	97.56 ± 0.04	0.51 ± 0.04
	Level2 Matching	91.27 ± 0.04	0.04 ± 0.04

case, the 50 GeV electron Level2 selection efficiency would be 87.12% and the pion fake rate would be four per mil.

During real data–taking in ATLAS, the selection optimization will be performed for the lowest possible particle energies, i.e. close to 20 GeV. In Chapter 5.3 the inclusive single and double electron trigger menus were presented: *e25i* and *2e15i* (*e30i* and *e20i*) at initial (design) luminosity). The physics performance of these trigger menus was assessed for simulated electron samples in Chapter 7. Therefore, as a final cross–check, the physics performance has been calculated for 50 GeV electron and pions using the cuts optimized for the 20 GeV samples. The results summarized in Table 9.4, show no performance degradation as particle energy increases. These results are comparable to the ones obtained in [89], where 2002 test beam data and offline calorimeter selection algorithms were used and an electron selection efficiency of $\sim 90\%$ was obtained for a pion fake rate of 5 per mil.

Chapter 10

Conclusions

In this thesis a study of the electron/photon physics selection strategy at the Level1 and High Level Trigger has been presented. The trigger strategy for inclusive electron selection has been evaluated on MC simulated data using the 'almost' final ATLAS HLT reconstruction software and realistic data access mechanism and steering of the algorithms. The electron trigger selection at each step (Level2 and Event Filter) has been evaluated in terms of physics performance (signal efficiency versus background rejection rate) and system performance (data preparation and execution time of the algorithms). A total trigger efficiency after the Event Filter of $\sim 76\%$ ($\sim 73\%$) for the single electron trigger with $p_T = 25(30)$ GeV at a trigger event rate of $40(\sim 200)$ Hz at a luminosity of 2×10^{33}cm^{-2}s^{-1} (10^{34}cm^{-2}s^{-1}) can be retained in $|\eta| < 2.5$. From present understanding, a reasonable target at the EF is to accept electrons with an overall efficiency of about $\sim 80\%$ with respect to the Level1 trigger in order not to cut too hard on physics. Further work is needed to optimize and cross–check the electron trigger selection at the high luminosity scenario. A total trigger efficiency after the Event Filter of $\sim 81\%$ for the single photon trigger with $p_T = 20$ GeV at a trigger event rate of 8 Hz at a luminosity of 2×10^{33}cm^{-2}s^{-1} in $|\eta| < 2.4$.

In order to understand where the computing resources are being used in the trigger, Level2 and EF system performance studies have been performed in terms of the data preparation and the algorithm feature execution time. A Level2 calorimeter and tracking algorithm processing times per RoI of $\sim 2 - 3$ ms was found which is within the average latency allowed (~ 10 ms). The data preparation part of the algorithms, conversion of the raw data bytestream to an object for algorithm reconstruction, was found to be the most time consuming part for both the Level2 and Event Filter trigger selection. Thus, timing performance is one of the most crucial issues of the HLT selection, specially at Level2, and has to be continuosly optimized to meet the design target. The Event Filter system performance studies performed has optimized the timing of calorimeter and ID offline algorithms used as an Event Filter prototype.

The trigger efficiencies for the Standard Model Higgs boson in the mass range below 190 GeV have been studied for several electron and photon decay modes. It has been demonstrated that the ATLAS online electron/photon trigger is efficient for selecting Higgs events with electron and photon decays: $H \to ZZ^* \to 4e$, $H \to ZZ^* \to 2e2\mu$, $H \to \gamma\gamma$ and

$H \to WW^* \to e\nu e\nu$ via VBF. The trigger efficiency for the Higgs decay $H \to ZZ^* \to 4e$ with $m_H = 130$ GeV was found to be 96.7% (95.5%) after the Event Filter in $|\eta| < 2.5$ for low (design) luminosity scenarios. The trigger efficiency for the Higgs decay $H \to \gamma\gamma$ with $m_H = 120$ GeV was found to be 83% after the Event Filter calorimeter selection in $|\eta| < 2.4$ for the low luminosity scenario. In addition, the results obtained demonstrate that the trigger menus for electrons and photons are well adapted for the Higgs physics programme envisaged at LHC. The overlap in the thresholds for transverse energy of the single and double electron/photon trigger makes the trigger selection very robust and stable. Furthermore the study of the $H \to ZZ^* \to 4e$ channel has proven that the inclusive electron trigger selection does not reject events prematurely. The present study confirms that the existing inclusive electron/photon trigger selection is as well efficient to select electrons from more challenging channels that involve other signatures apart from leptons and photons such as missing transverse energy for the $H \to WW^* \to e\nu e\nu$ via VBF channel. Future work should complete the analysis adding other trigger menus including objects like the muon, jet and E_T^{miss} triggers in online selections when the full trigger software for this menus will be available.

The electron/pion separation capabilities of the Level2 high–p_T single electron trigger has been studied with real data obtained in the 2004 ATLAS Combined Test Beam. Trigger electron efficiencies and pion fake rates have been studied for beam of electrons and pions at momenta of 20 GeV and 50 GeV using calorimeter information and tracking information from the Level2 trigger. A method to obtain pure samples of electrons and pions has been developed using beam line and TRT detector information. This study has shown that using the Level2 single electron selection, electron selection efficiencies of $\sim 90\%$ can be obtained while maintaining the pion fake rate at a level of 7 per mil. These results are comparable to previous offline electron selection studies performed with 2002 test beam data. The results of this analysis are important, since this is the first and only occasion that a full slice of ATLAS has been assembled and tested before the full ATLAS detector becomes operational.

Appendix A

Trigger Physics Performance Selection Cuts

A complete list of cuts used in the Level1 and HLT trigger selection (Level2 and Event Filter) for the sinlge and dounle electron trigger are presented. The cuts factorized by detector system are given in Table A.1, Table A.2 Table A.3 and Table A.4 for all levels separately. The order in which the cuts are presented is also the order in which they are applied. An exception is the E_T cut of Level2 calorimeter. It is applied at the very end of Level2, but presented (for convenience) in the Level2 calorimeter section.

LVL1	$e25i$	$e30i$	$e15i$
E_T (GeV) $>$	19	20	9
e.m. ring isol. (GeV) $<$	3	5	4
had. ring isol. (GeV) $<$	2	3	2
had. core isol. (GeV) $<$	2	2	2

Table A.1: Cuts applied on Level1 Calo.

LVL2		$e25i$	$e30i$	$e15i$
Calo	E_T (GeV) $>$	22.5	25.5	11
	$R_\eta^{shape} >$	0.90	0.90	0.9
	$R_\eta^{strip} >$	0.72	0.75	0.72
	E_T^{had} (GeV) $<$	1.0	2.2	1.0
ID	$p_T^{track}(GeV) >$	8	8	8

Table A.2: Cuts applied on Level2 Calo and Level2 ID.

LVL2 ID-Calo	e25i				e30i			
η-ranges	0.-1.	1.-1.5	1.5-2.	2.-	0.-1.	1.-1.5	1.5-2.	2.-
$\|\Delta\Phi\| <$	0.035	0.035	0.030	0.025			0.05	
$\|\Delta\eta\| <$	0.07	0.06	0.05	0.05			0.05	
$E_T/p_T \in$		[0.2,3.]		[0.2,3.5]		[0.2,4.]	[0.2,5.]	[0.2,7.]

Table A.3: Cuts applied on Level 2 ID-Calo.

EF		e25i	e30i	e15i
Calo	E_T (GeV) $>$	20	27	10
ID	# prec. hits $\geq$	7	7	7
	# pixel hits $\geq$	1	2	1
	# B-layer hits $\geq$	1	1	0
	$a_0^{vert} <$	0.2	0.2	0.2
ID-Calo	if $\eta < 1.37 \rightarrow E_T/p_T \in$	[.8,1.3]	[.7,1.7]	[.7,2.1]
	if $\eta \geq 1.37 \rightarrow E_T/p_T \in$	[.7,2.5]	[.7,2.7]	[.7,3.2]
	$\|\Delta\Phi\| <$	0.02	0.02	0.03
	$\|\Delta\eta\| <$	0.01	0.01	0.03

Table A.4: Cuts applied on EF Calo, ID and ID-Calo.

Appendix B

Energy Reconstrucion of the e.m. LAr Calorimeter

B.1   Energy Reconstruction

The reconstruction of the cell energy in ATLAS is done at the level of the ROD (Read Out Driver). The RODs receive the raw data and reconstruct the energy (E_{Rec}) and the time of flight (τ) of the particle using the optimal filtering technique. The reconstructed energy has the following expression:

$$E_{rec} = f \sum_{0 \leq i < Sample}^{i} a_i.S_i \tag{B.1}$$

$$\tau.E_{rec} = f \sum_{0 \leq i < Sample}^{i} b_i.S_i \tag{B.2}$$

The energy is computed as a linear sum of the $S_i = (ADC - Pedestal)$ values. The coefficients a_i and b_i are chosen so that eq. B.1 will be the energy (amplitude of the signal) and eq. B.2 will evaluate the energy times the time of flight. The index i represents the number of samples taken to calculate the pulse. For ATLAS this number is 5. ADC_i is the value of the ADC cut in a particular sample. As a function of the detector modes, the DSPs (ROD's processors) are initialized with different algorithms that allow for data taking in physics or calibration modes.

The decay time is determined by the pulser circuit. In order to obtain a 0.1% precision it is essential to form the pulse right on the electrodes so that the path for calibration signals be as close as possible to the path for physics signals.

B.1.1   Pedestal

The pedestal of a readout channel is the output signal when there is neither a beam nor a calibration pulse. The pedestal levels are calculated by computing the average output of each channel over all the pedestal events. Together with their standard deviation (which corresponds to the electronic noise) the pedestal levels are stored in a database for

later use with calibration and physics data, where they are subtracted channel by channel as explained above.

B.2 The Current to Energy Conversion Factor

A charge particle which passes through the detector induces ionization in the liquid argon all along its track. The corresponding charges are collected by the anodes of the detector. After the amplification and the shaping, five samples of the signal are digitized by an ADC (Analog to Digital Converted). At this stage, the signal is measured in ADC–counts.

In order to get the measured current in units of visible energy a factor $f_{I/E}$, which is assumed to be independent of the beam energy is applied to each cell. Since the EM calorimeter contains a two different geometries, the factors need to be calculated independently.

B.2.1 Accordion

Given that the accordion is a sampling calorimeter, the conversion factor $\mu A2MeV_{acc}$ can be estimated in the following way:

$$\mu A2MeV_{acc} = \frac{1}{I/E \times f_{sample}} \tag{B.3}$$

Where I/E is the energy to current conversion factor given by:

$$I/E = \frac{q_0}{W_0} f_{recomb}(E) V_d(E) \frac{E}{HV} \tag{B.4}$$

where:

- $q_0 = 1.6 \times 10^{-19} C$ is the electron charge.

- $W_0 = 23.6 eV$ is the ionization potential of the Liquid Argon.

- E is the electric field.

- $f_{recomb}(E)$ takes into account recombination effects (typically a few % for $E = 10 kV.cm^{-1}$.

- $V_d(E)$ is the drift velocity.

- $HV = 2000V$ is the hight voltage.

In the straight sections of the accordion calorimeter $E = HV/g$ where g is the gap width (2.12 mm). If we define $t_{drift} = g/V_d$ we can express I/E in the straight section as:

$$I/E_{straight} = \frac{q_0}{W_0} f_{recomb}(E) \frac{V_d(E)}{g} = \frac{q_0}{W_0} f_{recomb}(E) t_{drift} \tag{B.5}$$

In the accordion foldings, the electric field behaves differently (the charge collection is different) and the formula $E = HV/g$ no longer holds. To account for this difference,

equation B.4 needs to be integrated for charges deposited in the full LAr gap. The size of this effect is around 7%.

The values of I/E in the straight parts of the accordion from the simulation and the data are $14.2 nA/MeV$ and $16 nA/MeV$ respectively. Since the differences are not understood as of yet, the value obtained from the data will be used.

f_{sample} is the sampling fraction which translate the visible energy deposited in the Liquid argon (E^{act}) into the total deposited energy (E^{tot}):

$$f_{sample} = \frac{E^{act}}{E^{tot}} \tag{B.6}$$

It can be estimated knowing the energy deposited by ionization dE/dx (deposited by a MIP) and the additional energy e/μ deposited by radiation by an electron:

$$f_{sample} = \frac{e}{\mu} \times \frac{dE/dx|_{act}}{dE/dx|_{act} + de/dx|_{pas}} \tag{B.7}$$

The additional effect of the electric field is taken into account by computing the visible energy from the simulated current I_{sim} using $I/E_{straight}$:

$$E^{act} = \frac{I_{sim}}{I/E_{straight}} \tag{B.8}$$

which lead to a value of f_{sample} 7% lower than with equation :

$$f_{sample} = 0.1667 \qquad \text{for} \qquad \eta < 0.8 \qquad = 0.1959 \qquad \text{for} \qquad \eta > 0.8 \tag{B.9}$$

The dependence of the sampling fraction on the shower depth in taken into consideration at the cluster level.

B.2.2   Presampler

Given that the presampler is not a sampling calorimeter, the conversion from current to energy is done in the following manner and replacing f_{sample} with a factor that is specific to the presampler denoted by F_{PS}:

$$\mu A2MeV_{PS} = \frac{1}{I/E \times F_{PS}} \tag{B.10}$$

Since there is no bending in the presampler, the electric field suffers no deformations; however, the gap width varies according to η between 1.9 and 2.0 mm introducing an η dependence in I/E and a higher value for I/F_{PS} than I/E_{acc}. For simplicity, only one value of I/E is used for the whole presampler averaging thus over the gap widths. Only 11 mm out of the 13 mm of the active layer of the presampler are exposed to the electric field, therefore the current Geant4 simulation needs to be adjusted in order to take this fact into consideration. Future releases will cure this problem. The presampler conversion value can be deduced from the accordion by multiplying I/E_{acc} by the ratio of the gap width:

$$I/E_{PS} = I/E_{acc} \times \frac{g_{acc}}{g_{PS}} = 16 \times \frac{2.12}{1.95} = 17.4 nA/MeV \tag{B.11}$$

B.3 Optimal filtering technique

A digital filtering technique is used to extract the peak amplitude A and the signal time. This employs 5 signal samples (S_i) where A is expanded in a linear weighted sum of coefficients (OF) and the pedestal is subtracted from the signal in each sample (see eq. B.1).

This method ensures a non-biased way of cell energy reconstruction which minimizes noise contributions in particular during low luminosity periods. The coefficients are calculated using the expected shape of the pulse, its derivative and the noise autocorrelation function. The noise contribution is minimized respecting the constraints on the signal amplitude and its time jitter [1]. The noise autocorrelation function is determined from randomly triggered events.

The shape of the physics signal g_i ($g_i \equiv g(t_i)$) can be predicted using a formula with four free parameters which can be extracted from a fit to the measured physics pulse shape [91]. Then the OF coefficients are calculated in such a way that the variance of eq. B.1 and eq. B.2 and is minimized satisfying a series of constraints. The shapes of the measured and predicted physics pulse agree within 2%.

The height of the pulse after shaping is proportional to the energy deposited by a passing charged particle in the liquid argon. By sampling the pulse at its peak, one can get a measurement of the energy. However, in doing this noise is introduced in the pulse and the sample assumed to be taken at the peak of the pulse can be shifted due to jitter, etc.

These effects are partially compensated by sampling the pulse and applying the optimal filtering technique. Once the pulse shape and the noise autocorrelation matrix are known, linear coefficients can be optimized in order to maximize the signal to noise ratio.

With two sets of linear weights a_i and b_i the following linear combinations are formed:

$$A = \sum_i a_i S_i \tag{B.12}$$

$$A\tau = \sum_i b_i S_i \tag{B.13}$$

where S_i are the signal samples. The computation of a_i and b_i is described in detail in [92], then the following conditions are imposed:

$$A = < \sum_i a_i S_i > \qquad \text{and} \qquad A\tau = < \sum_i b_i S_i > \tag{B.14}$$

If the signal shape can be described with a function g, then the samples S_i can be expressed in the following way:

$$S_i = Ag(t - \tau) = Ag_i - A\tau g_i' n_i \tag{B.15}$$

Here n_i is the noise, while g_i and g_i' are respectively the value of the shaping function g and the value of its first derivative for the sample i.

---

[1] A shift on t_0, τ or on the sampling frequency due to a jitter on the clock can cause an extra contribution to the constant term of the energy resolution thus degrading the latter [90]

When replacing S_i by its Taylor expansion in equation B.14, we get:

$$A = \sum_i (Aa_ig_i - A\tau a_ig_i' + <n_i>) \tag{B.16}$$

$$A\tau = \sum_i (Ab_ig_i - A\tau b_ig_i' + <n_i>) \tag{B.17}$$

By requiring that the average of the noise remains equal to zero, the following constraints are obtained:

$$\sum_i a_ig_i = 1 \quad \text{and} \quad \sum_i a_ig_i' = 0 \tag{B.18}$$

$$\sum_i b_ig_i = 0 \quad \text{and} \quad \sum_i b_ig_i' = -1 \tag{B.19}$$

Appendix C

Combined Test Beam Studies

C.1 Online Running of HLT Algorithms

For both, Level2 and EF, histograms allowed to monitor the selection process. The histograms were sent from the processing units to a histogram collection facility from where display programs could retrieve them for graphical presentation. Figure C.1 shows the number of tracks and different track computed values from IdScan Level2 tracking algorithm. Before installation at the test beam the software was extensively tested in Level2 and EF emulators as well as combined Level2 and EF multi-node testbeds, as devised in in the development strategy adopted by HLT.

C.2 Level2 Electron Selection

Table C.1: Summary of the Level2 electron identification cuts used in the study in Chapter9. They are optimized in order to obtain the best pion rejection rate, while retaining a $\sim 90\%$ Level2 overall electron selection efficiency.

Sample Energy	$E_T(GeV)$	$E_T^{Had}(GeV)$	R_η^{shape}	R_η^{strips}	E_T/p_T	$\Delta\eta$	$\Delta\phi$
	>	<	>	>	>	<	<
20 GeV	12.0	0.5	0.92	0.70	0.6	0.04	0.04
50 GeV	30.0	0.5	0.88	0.80	0.6	0.05	0.05
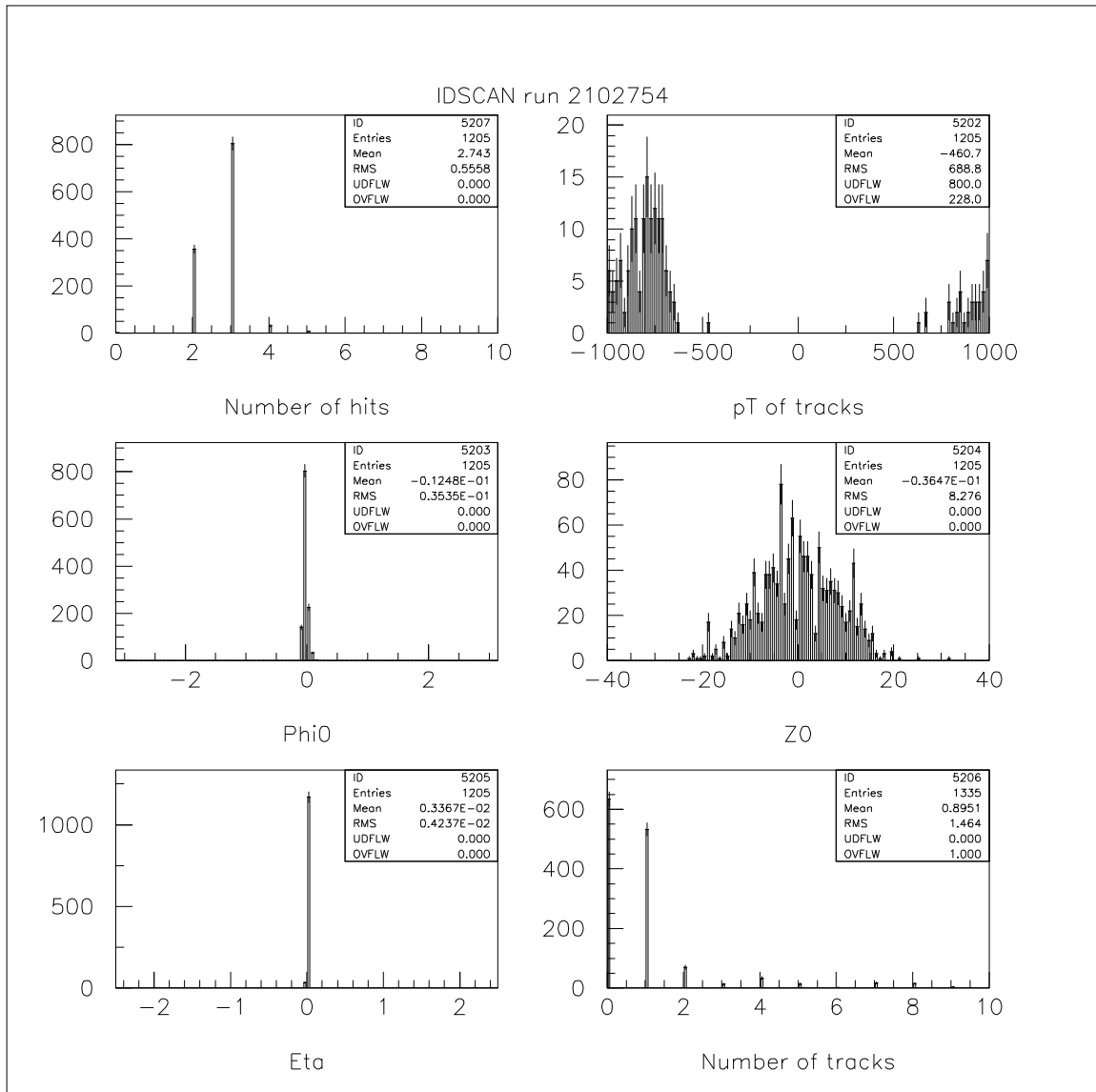
Figure C.1: Online Histograms obtained at the CTB running IdScan tracking algorithm.
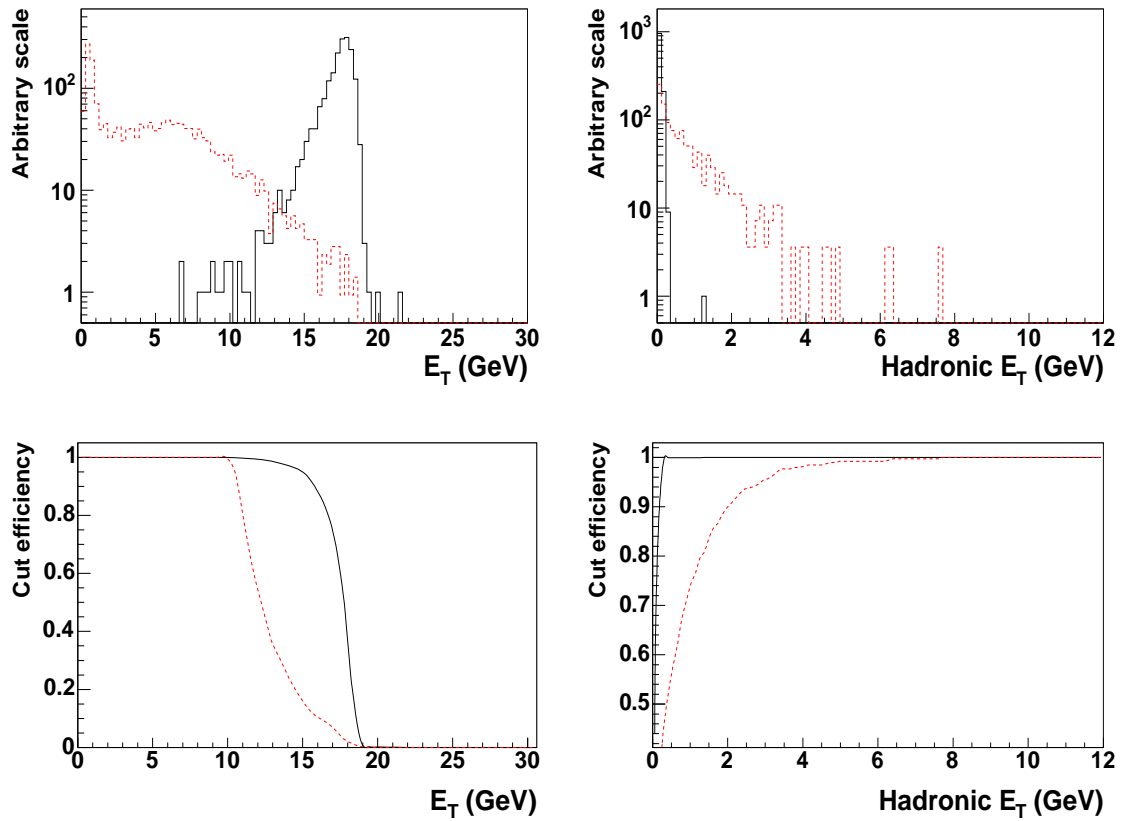
Figure C.2: Distributions of the transverese energy deposited in the second sampling of the e.m. calorimeter (E_T), and the transverese energy deposited in the first sampling of the hadronic calorimeter ($HadronicE_T$) are shown for 20 GeV electrons (continous line) and pions (dotted line). The efficiency for selecting the corresponding particles as a function of the cut is also shown.
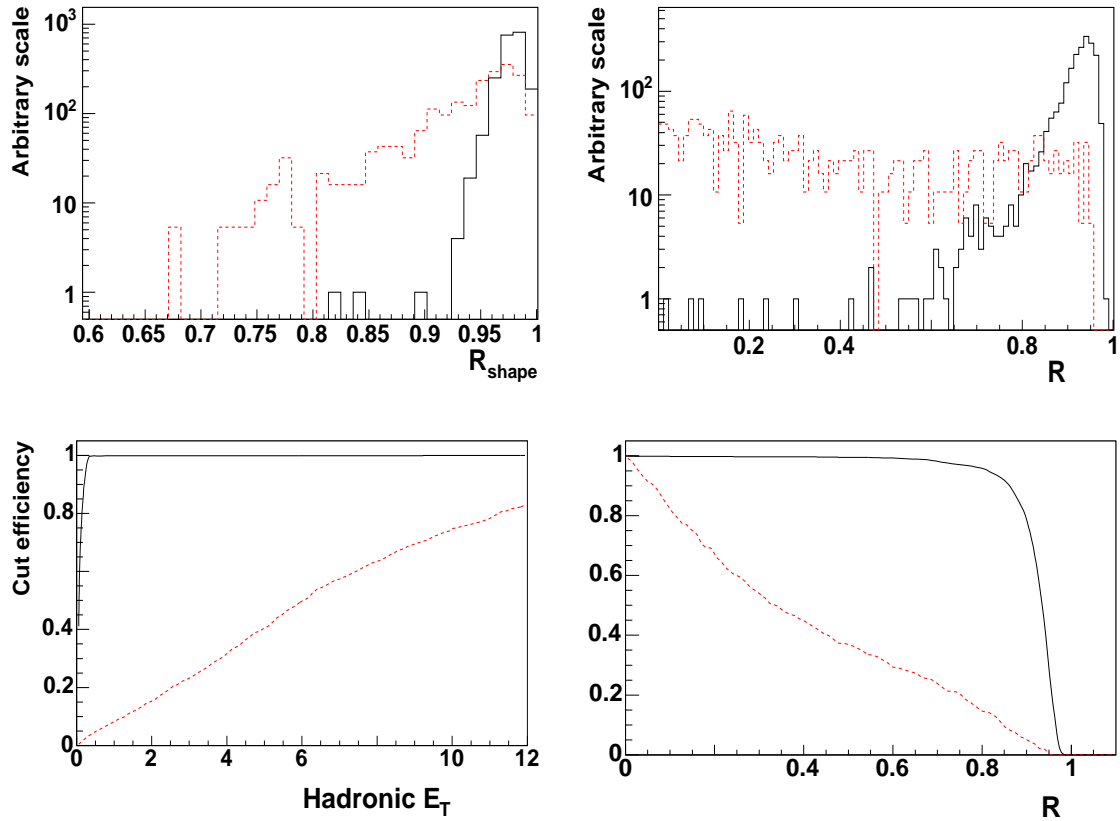
Figure C.3: Distributions of the lateral shape in the second sampling of the e.m. calorimeter (R_{shape}), and the lateral shape in the first sampling of the calorimeter (R_{strips}) are shown for 20 GeV electrons (continous line) and pions (dotted line). The efficiency for selecting the corresponding particles as a function of the cut is also shown.
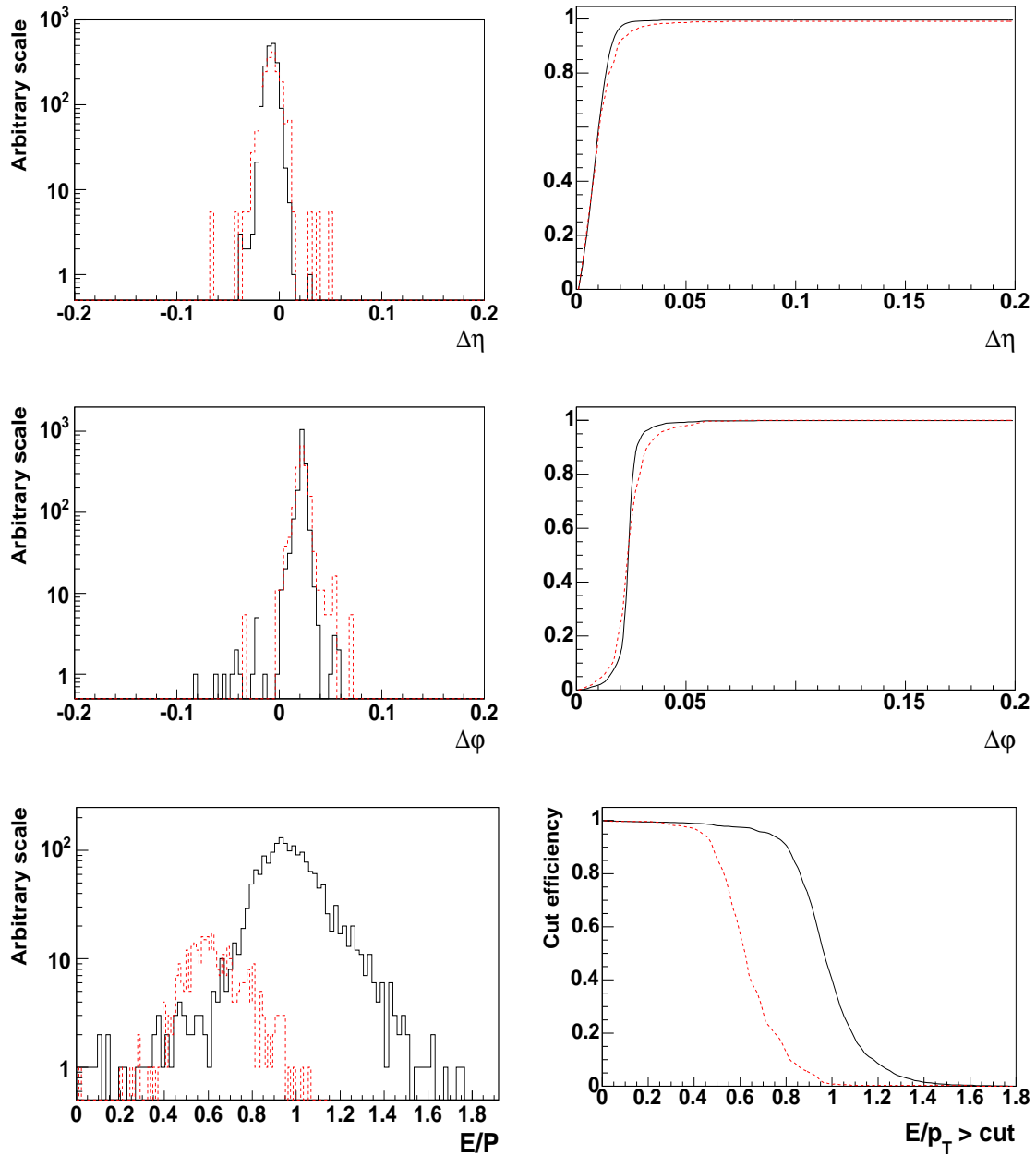
Figure C.4: Distributions of the position difference between the cluster and the track in η ($\Delta\eta$) and in ϕ ($\Delta\phi$) as well as the distribution of the ratio between the cluster energy and the momentum of the reconstructed track (E_T/p_T) are shown for 20 GeV electrons (continous line) and pions (dotted line). The efficiency for selecting the corresponding particles as a function of the cut is also shown.

Bibliography

[1] Spiesberger H., Spira M., and Zerwas P.M. The standard model: Physical basis and scattering experiments. *DESY*, hep-ph/0011255; DESY-THESIS-2000-01; MZ-TH-2000-53; PSI-PR-2000-17, 2000.

[2] Glashow S.L. *Nucl. Physics*, 20:579, 1961.

[3] Salam A. *Elementary Particle Theory*. Svartholm ed. Stockholm, 1968.

[4] Weinberg S. *Phys. Rev. Lett.*, 19:1264, 1967.

[5] Friedman J.I. and Kendall H.W. *Ann. Rev. Nucl. Sci.*, 22:203, 1972.

[6] Gell-Man M. *Phys. Lett.*, 8:214, 1964.

[7] Zerwas P.M. *T*. Kluwer Academic Publishers. Amsterdam, 1999.

[8] Weyl H. *Z. Phys.*, 56:330, 1929.

[9] Yang C.N. and Mills R. *Phys. Rev.*, 96:191, 1954.

[10] Higgs P. W. *Phys. Lett.*, 12:132, 1964.

[11] Englert F. and Brout T. *Phys. Rev. Lett.*, 13:321, 1964.

[12] Guralnik G.S., Hagen C.R., and Kibble T.W. *Phys. Rev. Lett.*, 13:585, 1964.

[13] Hooft G. *Nucl. Phys.*, B33:173, 1971.

[14] Hooft G. and Veltman M. *Nucl. Phys.*, B44:189, 1972.

[15] LEP Collaboration. *LEP-EWWG/LS2000-01*, 2000.

[16] Altarelli G. Concluding talk: Status of the standard model and beyond. *CERN-PH-TH/2005-051*, SIS-2005-004, 2005.

[17] Altarelli G. The crucial problem: the electroweak symmetry breaking. *CERN*, CERN-TH/99-365, 1999.

[18] Higgs Working Group. Report of the tevatron higgs working group. hep-ph/0010338, 2000.

[19] Dedes A., Heinemeyer S., Su S., and Weiglein G. *Nucl. Phys.*, B674:271, 2003.

[20] Giudice G.F., Rattazi R., and Wells J.D. *Nucl. Phys.*, 595:250, 2001.

[21] ATLAS Collaboration. *The Large Hadron Collider Technical Design Report.* CERN/AC/95-05, 1995.

[22] LHCb Collaboration. *LHCb Technical Proposal.* CERN/LHCC/98-4, 1998.

[23] ALICE Collaboration. *ALICE Technical Proposal.* CERN/LHCC/95-71, 1995.

[24] ATLAS Collaboration. *ATLAS Trigger Performance Status Report.* CERN/LHCC/98-15, 1998.

[25] ATLAS Collaboration. *ATLAS Detector and Physics Performance Technical Design Report.* CERN/LHCC/99-14, 99-15, 1999.

[26] Pretzl K. Calorimeters in astro and particle physics. *J. Phys. G: Nucl. Part. Phys. Res.*, 31:R133, 2005.

[27] ATLAS Collaboration. *Liquid Argon Calorimeter Technical Design Report.* CERN/LHCC/96-41, 1996.

[28] Spira M. *Fortsch. Phys.*, 46, 1998.

[29] Gianotti F. Collider physics: Lhc. *ATLAS internal note*, ATLAS-CONF-2001-001, 2000.

[30] Costanzo D. Higgs physics at the lhc. *ATLAS internal note*, Talk presented at the XXXXVI Recontres de Moriond Electroweak Interactions and Unified Theories, 2001.

[31] Asai S. et al. Prospects for the search of a standard model higgs boson in atlas using vector boson fusion. *ATLAS internal note*, SN-ATLAS-2003-024, 2004.

[32] Jakobs K. *Physics at the Large Hadron Collider.* Nuclear Physics B 116-149, 2003.

[33] Jakobs K. and Tresfger T. Sm higgs seaarches for $h \to ww^* \to l\nu l\nu$ with a mass between $150 - 190$ gev at lhc. *ATLAS internal note*, ATLAS-PHYS-COM-99-031, 1999.

[34] Jakobs K. A study of the associated production wh, $h \to ww^* \to l\nu l\nu$. *ATLAS internal note*, ATLAS-PHYS-COM-99-062, 1999.

[35] Cavalli D. et al. The higgs working group: summary report. hep-ph/0203056, 2002.

[36] Savard P. and Azuelos G. The discovery potential of a heavy higgs ($m_H = 800$gev) using full simulation of atlas. *ATLAS internal note*, ATLAS-PHYS-98-128, 1998.

[37] Ruiz H. and Bosman M. The discovery potential of a heavy sm higgs boson through the $h \to zz \to ll\nu\nu$ channel at the lhc with the atlas detector. *ATLAS internal note*, ATLAS-PHYS-2002-027, 2002.

[38] Unal G. Search for higgs. *Talk presented at the IV ATLAS Physics Workshop*, 2003.

[39] Bern Z., Dixon L., and Schmidt C. Isolating a light higgs boson from the di–photon background at the lhc. hep-ph/0206194, 2002.

[40] ATLAS Collaboration. *ATLAS High Level Trigger Data Acquisition and Controls.* CERN/LHCC/2003-022, 2003.

[41] ATLAS Collaboration. *ATLAS First–Level Trigger Technical Design Report.* CERN/LHCC/98-14, 1998.

[42] AthenaDeveloperGuide-8.0.0-draft.pdf. *The ATHENA architecture.* http://atlas.web.cern.ch/Atlas/GROUPS/SOFTWARE/OO/architecture.

[43] Wiedenmann W. et al. *IEEE Trans. Nucl. Sci.*, 51:915, 2004.

[44] Beck HP. et al. *IEEE Trans. Nucl. Sci.*, 51:470–475, 2004.

[45] Haeberli C. et al. *IEEE Trans. Nucl. Sci.*, 51:585–590, 2004.

[46] Hauser R. The atlas trigger system. *ATLAS internal note*, SN-ATLAS-2003-027, 2003.

[47] Elsing M. et. al. Analysis and conceptual design of the hlt selection software. *ATLAS internal note*, ATL-DAQ-2002-013, 2002.

[48] PESA Core Algorithms Group. Algorithms for the atlas high level trigger. *ATLAS internal note*, ATL-DAQ-2003-002, 2003.

[49] Comune G. et al. The algorithm steering and trigger decision mechanism of the atlas high level trigger. *ATLAS internal note*, ATL-DAQ-2003-031, 2003.

[50] Schorner-Sadenius T. and Tapprogge S. Atlas trigger menus for the lhc start–up phase. *ATLAS internal note*, ATL-DAQ-2003-004, 2003.

[51] Gonzalez S., Hansl-Kozanecka T., and Wielers M. Selection of high-pt electromagnetic clusters by the second level trigger of atlas. *ATLAS internal note*, ATL-DAQ-2000-002, 1999.

[52] Gonzalez S., Gonzalez-Pineiro B., and Shears T.G. First implementation of calorimeter fex algorithms in the lvl2 reference software. *ATLAS internal note*, ATL-DAQ-2000-020, 2000.

[53] Shears T.G. and Gonzalez S. Further studies and optimisation of the level-2 trigger electron/photon fex algorithm. *ATLAS internal note*, ATL-DAQ-2000-042, 2000.

[54] Wielers M. Photon identification with the atlas detector. *ATLAS internal note*, ATL-PHYS-99-016, 1999.

[55] Konstantinidis N.P. and Drevermann H. Determination of the z position of primary interactions in atlas. *ATLAS internal note*, ATL-DAQ-2002-014, 2002.

[56] Konstantinidis N.P. and Drevermann H. Algorithms to select space points of tracks from single primary interactions in atlas. *ATLAS internal note*, ATL-COM-DAQ-2003-040, 2003.

[57] Gaines I., Gonzalez S., and Qian S. Implementation of an oo track reconstruction model into multiple lhc experiments. *CHEP Conference in Padova*, 2000.

[58] Pralavorio P. Electron/jet separation with the atlas detector. *ATLAS internal note*, ATL-PHYS-99-015, 1999.

[59] Baines J. T. M., Gonzalez S., Mommsen R. K., Radu A., Shears T. G., Sivoklokov S. Yu, and Wielers M. First study of the lvl2-ef boundary in the high-pt electron/photon high-level trigger. *ATLAS internal note*, ATL-DAQ-2000-045, 2000.

[60] Santamarina C. et al. Implementation and performance of the seeded reconstruction for the atlas event filter selection software. *ATLAS internal note*, ATL-COM-DAQ-2005-026, 2005.

[61] Wielers M. Isolation of photons. *ATLAS internal note*, ATL-PHYS-2002-004, 2001.

[62] Gavrilenko I. Description of global pattern recognition program (xkalman). *ATLAS internal note*, ATL-INDET-97-165, 1997.

[63] Clifft R. and Poppleton A. Ipatrec: inner detector pattern-recognition and track-fitting. *ATLAS internal note*, ATL-SOFT-94-009, 1994.

[64] Benekos N.C., Clifft R., Elsing M., and Poppleton A. Atlas inner detector performance. *ATLAS internal note*, ATL-INDET-2004-002, 2003.

[65] Vaniachine A. et al. Data challenges in atlas computing. *Nuclear Instruments and Methods in Physics Research*, **502**:446–449, 2003.

[66] ATLAS Collaboration. *Inner Detector Technical Design Report*. CERN/LHCC/97-17, 1997.

[67] Sjostrand T., Lonnblad L., Mrenna S., and Skands P. *PYTHIA 6.206 manual*, second edition, 2002. LU TP 0121.

[68] Brun R. et al. *GEANT3 Detector Description and Simulation Tool*. CERN DD/EE/84-1, 1986.

[69] Grothe M. et al. Architecture of the atlas high level trigger event selection software. *Nucl. Instrum. Methods Phys. Res.*, A (518):537, 2004.

[70] ATLAS Collaboration. *Computing Technical Design Report*. CERN/LHCC/2005-022, 2005.

[71] Moyse E.J.W. and Watson A. Performance and validation of trigt1calo, the offline level-1 calorimeter trigger simulation. *ATLAS internal note*, ATL-DAQ-2003-027, 2003.

[72] ATLAS Collaboration. *ATLAS High–Level Triggers, DAQ and DCS Technical Proposal.* CERN/LHCC/2000-17, 2000.

[73] Tapprogge S. Physics requirements for the atlas high-level trigger. *ATLAS internal note*, ATL-DAQ-2000-033, 2000.

[74] Tapprogge S. *ATLAS trigger rates and associated physics performance*, 2002. http://agenda.cern.ch/.

[75] Thomas E. Private communication. *ATLAS internal note*, 2005.

[76] Baines J. et al. Performance studies of the high level electron trigger. *ATLAS internal note*, ATL-COM-DAQ-2003-020, 2003.

[77] Cranmer K., Fang Y., Mellado B., Paganis S., Quayle W., and Wu S. L. Analysis of vbf $h \to ww \to \nu\nu$. *ATLAS internal note*, ATL-PHYS-2004-019, 2004.

[78] Paganis S. Higgs$\to zz^* \to 4l$ analysis with dc1 full atlas simulation and reconstruction. *ATLAS internal note*, ATL-COM-PHYS-2005-043, 2005.

[79] Linossier 0. and Poggioli L. H to zz* to 4 leptons channel, in atlas signal reconstruction and reducible backgrounds rejection. *ATLAS internal note*, ATL-PHYS-97-101, 1997.

[80] Bettinelli M., Carminati L., Consonni M., and Tartarelli G.F. Analysis of the inclusive $h \to \gamma\gamma$ channel with dc1 samples. *ATLAS internal note*, ATL-COM-PHYS-2005-056, 2005.

[81] Perez-Reale V. Triggering standard model higgs processes in the atlas experiment. *ATLAS internal note*, ATL-COM-PHYS-2004-051, 2004.

[82] Gadomski S. et al. Deployment and use of the atlas daq in the combined test beam. *ATLAS internal note*, ATL-DAQ-CONF-2005-019, 2005.

[83] Di Girolamo B., Dotti A., Giangiobbe V., Johansson P., Pribyl L., and Volpi M. Beamline instrumentation in the 2004 combined atlas testbeam. *ATLAS internal note*, ATL-TECH-PUB-2005-001, 2005.

[84] Di Girolamo B. Mpbs magnet characteristics. *CERN*, ATC-TT-EN-006, 2003.

[85] Cerutti F. et al. Proposed measurement program for h8 2004 muon system test. *ATLAS internal note*, ATL-COM-MUON-2004-006, 2004.

[86] *CASTOR*. http://castor.web.cern.ch/castor/.

[87] Anjos A. et. al. Deployment of the atlas high-level triggers. *ATLAS internal note*, ATL-COM-DAQ-2005-023, 2005.

[88] Diaz-Gomez M., Padilla C., Riu I., and Perez-Reale V. Performance of the second level trigger electron selection algorithms with the 2004 atlas combined test beam data. *ATLAS internal note*, ATL-COM-PHYS-2005-069, 2005.

[89] Lu L., Stroynowski R., and Gao Y. Electron identification and e/π separation with barral module p15. *ATLAS internal note*, ATL-COM-LARG-2003-004, 2003.

[90] Wingerter-Seez I. Study of energy reconstruction using optimal filtering with the lar electromagnetic calorimeter. *ATLAS internal note*, LARG-NO-19, 1995.

[91] Prieur D. Etalonnage du calorimetre electro-magnetique du detecteur atlas. reconstruction des evenements avec des photons non pointants dans le cadre d'un modele super-symmetrique gmsb. *These Universite Annecy (France)*, LAPP-T-2005-03, 2005.

[92] Cleland W.E. and Stern E.G. Signal processing considerations for liquid argon ionization calorimeters in a high rate environment. *Inst. and Meth.*, A 338:467–497, 1994.

Acknowledgments

Curriculum Vitae

Name:	Valeria Perez Reale
Place of Birth:	Santa Rosa, Argentina
Date of Birth:	February 10th 1977
Nationality:	Spanish, Argentinian

1991-1994 High School Education	Escuela Normal Superior Santa Rosa, Argentina
1995-2001 University Education	Facultad de Ciencias Exactas y Naturales Universidad Nacional de La Pampa Santa Rosa, Argentina
2001	Licenciada en Fisica (Master in Physics) Universidad de La Pampa, Argentina Supervisor: Prof. Dr. Roberto Deza
2002-2006	PhD in Physics Laboratory for High Energy Physics University of Bern, Switzerland Supervisor: Prof. Dr. Klaus Pretzl